Finite Element Study on Bridge Details Susceptible to Distortion-Induced Fatigue

By

Christopher A. Adams

Submitted to the graduate degree program in Civil Engineering
and the Graduate Faculty of the University of Kansas School of Engineering
in partial fulfillment of the requirements for the degree of
Master of Science

_____
Chairperson

Committee Members: _____

_____

Date Defended: _____

The Thesis Committee for Christopher Adams certifies that
This is the approved version of the following thesis:

Finite Element Study on Bridge Details Susceptible To Distortion-Induced Fatigue

_____
Chairperson

Committee Members: _____

_____

Date Defended: _____

ACKNOWLEDGEMENTS

I would like to thank Drs. Adolfo Matamoros, Caroline Bennett, Stan Rolfe, and Ron Barrett for the opportunity to work on this research project. I would also like to thank them for their guidance, support, and expertise in everything involved with the project. Also, thanks to Transportation Pooled Fund Study, TP5-5 (189), for providing the funding required to work on the project.

I would also like to thank my family and friends for their everlasting support through the research process.

ABSTRACT

Some bridges designed prior to the mid 1980s have experienced problems in the web-gap region, above plates connecting intermediate stiffeners to the girder web and below girder top flanges, due to differential deflections of adjacent girders. The effects from cross frames attached to girders subjected to these differential deflections are the cause of out-of-plane deformations or distortions, which are the driving force for fatigue cracks in the web-gap region. A few retrofits exist that focus on reducing or eliminating the magnitude of web-gap stress; these include lengthening the web-gap with a slot repair or fixing the connection plate to the top flange creating a positive attachment. Both of these retrofits have been used with mixed results. Because of this, new retrofitting schemes were studied which utilized carbon fiber reinforced polymers (CFRP) to reduce the stress demand and achieve a more even distribution of stresses in web-gap regions by providing an alternative load path for secondary stresses. Finite element (FE) models were used to study the effectiveness of the new retrofit methods in comparison with the slot and positive attachment repair methods. The results of the FE models showed that the CFRP materials repair technique was more effective in reducing the magnitude of web-gap stress and web distortion than the other two aforementioned specimens.

TABLE OF CONTENTS

LIST OF FIGURES

LIST OF TABLES

LIST OF SYMBOLS

Symbol	Description
E_c	Concrete Modulus of Elasticity
f'_c	Specified Concrete Compressive Strength
in	Inch
K_I	Stress Intensity Factor
ΔK_I	Stress Intensity Factor Range
kip	Kilo-pound (1,000 pounds)
kl	Effective Length
ksi	Kips per Square Inch
mm	Millimeter
n	Modular Ratio
PL	Plate
psi	Pounds per Square Inch
r	Radius of Gyration
σ_{nom}	Nominal Stress
$\Delta\sigma_{nom}$	Nominal Stress Range

LIST OF ACRONYMS

Acronym	Description
3D	Three Dimensional
AASHTO	American Association of State Highway and Transportation Officials
ACI	American Concrete Institute
AISI	American Iron and Steel Institute
AISC	American Institute of Steel Construction
ASTM	American Society of Testing and Materials
CFRP	Carbon Fiber Reinforced Polymer
FE or FEA	Finite Element Analysis
HSS	Hot Spot Stress
IIW	International Institute of Welding
KU	University of Kansas
Mn/DOT	Minnesota Department of Transportation
NSBA	National Steel Bridge Alliance
SS	Structural Stress
TRB	Transportation Research Board
UIT	Ultrasonic Impact Treatment

CHAPTER 1 – INTRODUCTION

Fatigue cracking in steel connections and welds has been a problem observed in many bridges around the world. Fatigue cracks often initiate from welds or other structural discontinuities and propagate through structural components until they are arrested or until failure. Due to the high frequency of fatigue cracks found during bridge inspections, the Minnesota Department of Transportation (Mn/DOT) sponsored a study seeking to identify connection details in which fatigue cracks were most commonly found (Lindberg and Schultz 2007). The research included a survey that was sent to state DOTs and the US Army Corps of Engineers to report the number of and type of details that were most prone to fatigue cracking. The survey asked to identify problems with details not found in published sources. Sixteen surveys were completed, and the results were compiled in a Mn/DOT report outlining the findings.

Based on the surveys, a list of eleven details that experience fatigue problems was compiled. In particular, four fatigue details were found to occur more frequently than the remaining seven. Although the vulnerability of these details is not always related to distortion of the web, the four most commonly found details and the particular fatigue problems associated with these details are described in the following as part of a literature review within this thesis.

1.1 TRANSVERSE STIFFENER WEB GAP

This type of connection detail develops fatigue cracks in the web-gap region between the girder flange and transverse connection plate. Transverse connection plates are intended to attach lateral braces (X, K, or plate type) between adjacent bridge girders; these braces exist to transfer traffic loads transversely between girders and to provide support against lateral-torsional buckling of the bridge girders during construction (Tedesco et al. 1995). From the completed surveys, this particular detail was found to be the most common and is a product of bridge distortion which "accounts for the largest category of fatigue cracking nationwide" (Roddis and Zhao 2001). This distortion is caused by differential deflections between adjacent girders (see Figure 1-1), wherein high secondary stresses are formed in the web-gap regions near the top of the girder where the concrete deck restrains rotation of the top flange.

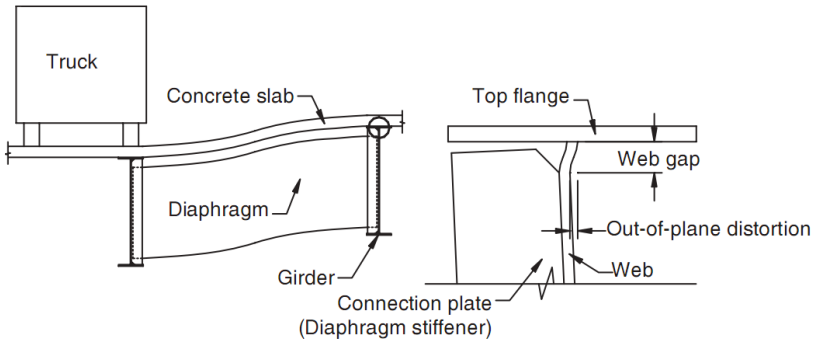

Figure 1-1 Differential deflection (Hu et al. 2005)

Web-gaps exist because it was common practice to cut the transverse stiffener short of the tension flange prior to the mid 1980s to avoid fatigue-

sensitive weldments in regions of high tension stress; this was done because early experience with transverse welds on tension flanges of European bridges in the 1930s resulted in a number of fractures (Fisher and Keating 1989). Also, web-gaps can sometimes occur between the compression flange and connection plate for ease of fabrication (Castiglioni et al. 1988). Because of this, fatigue cracking can occur in both the positive and negative moment regions where the top flange is in compression and tension, respectively. Various factors that influence the location of distortion-induced fatigue cracks are discussed in the following sections.

1.1.1 DISTORTION CRACKS IN POSITIVE AND NEGATIVE MOMENT REGIONS

There has been much discussion about the location along a girder where distortion-induced fatigue cracks in the web-gap region are most likely to form. Although many papers have been published concerning this topic, the results are inconclusive and there is no consensus opinion about which moment region these cracks typically form in.

- Positive Moment region – Positive bending occurs away from bridge supports where longitudinal compressive stresses occur at and near the top girder flanges. Also, differential deflections between adjacent girders are the highest. Because of this, Roddis and Zhao (2001) state “cracks most frequently occur in the positive moment regions of the bridge girders,

where the differential girder deflections are the largest and the out-of-plane bending moments are the highest."

- Negative Moment region – Negative bending occurs at bridge supports where longitudinal tensile stresses occur at and near the top girder flanges. Khalil et al. (1998) investigated a skewed bridge with X-type diaphragms, and eight (8) out of nine (9) cracks due to differential deflections between adjacent girders occurred in the negative moment region.

Based on this, it is unclear which moment region is more susceptible to cracking due to differential deflections of adjacent girders.

1.1.2 SKEW VS. NON-SKEW BRIDGES

Bridges are often skewed to accommodate ever-increasing complex highway alignments, and the skew angle influences susceptibility to distortion-induced fatigue in steel bridge girders. Because of the skew, lateral brace placement is complicated. These braces can be staggered or can be rotated parallel to the bridge skew in certain situations. The AASHTO Bridge Design Code (2002, 2004) allows bracing to be rotated parallel to the skew angle if the skew angle is less than 20°, as shown in Figure 1-2. When the skew angle is greater than 20°, connection and braces become too flexible due to longer brace lengths when the braces are oriented parallel to the skew angle (Wang and Helwig 2008). Because of this, the AASHTO Bridge Code (2002, 2004) specifies that the

bracing must be perpendicular to the longitudinal direction of the girder; bracing may either be non-staggered (Figure 1-3) or staggered (Figure 1-4).

Presence of stagger also has an effect on web-gap cracking. Barth and Bowman (2001) reported that non-staggered diaphragms were more susceptible to fatigue cracking than comparable staggered diaphragm configurations. Because the connection plates exist on both sides of the web in non-staggered situations, this configuration makes the connection more rigid and more prone to cracking over webs with connection plates only on one side of the web.

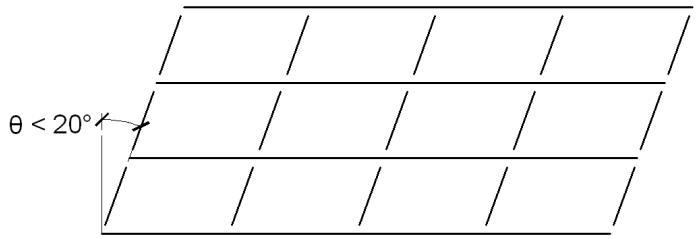

Figure 1-2 Bridge skew < 20°

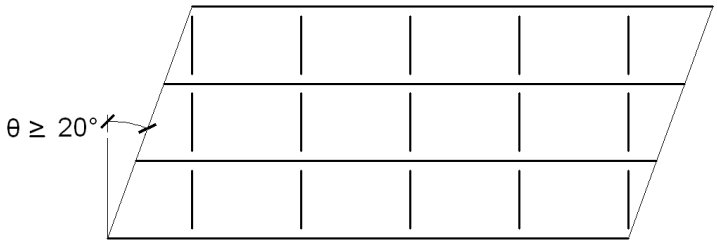

Figure 1-3 Bridge skew ≥ 20° (no stagger)

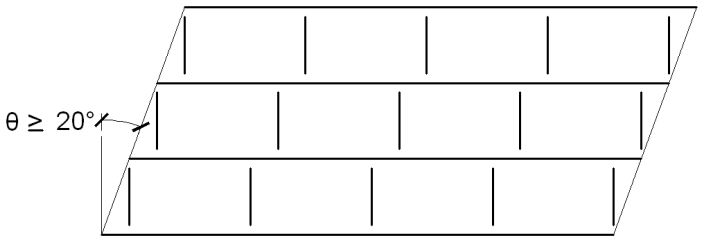

Figure 1-4 Bridge skew ≥ 20° (stagger)

All of these factors affect the behavior of fatigue cracking in the most common bridge detail experiencing fatigue problems.

1.2 INSUFFICIENT COPE RADIUS

The second most common fatigue-prone detail found in the Mn/DOT survey involves cracking at coped sections of floor beams which act as lateral bracing or load distribution members. Floor beams are often coped to provide enough clearance for the supports when the framing beams are at the same elevation as the main girders, as shown in Figure 1-5 (Yam and Cheng 1990). In addition, both the top and bottom flanges of floor-beams or plate diaphragms may be coped to allow these members to be reversed or inverted in the event of cracking (Zwerneman et al. 1993). Because of coping, the flexural resistance of the beam is reduced by up to 90%, which introduces a high stress concentration at the cope corner caused by geometric discontinuities (Cheng and Yura 1986). This structural discontinuity is the initiation site for fatigue cracks.

Coping is normally achieved by flame cutting, and this fabrication method produces metallurgical changes such as the formation of a martensitic layer at the cut edge (Goldberg 1973). This layer is known to have micro flaws which can be the source of fatigue cracking (Yam and Cheng 1990). Flame cutting introduces high tensile residual stresses at the cut edge due to differential temperature during cooling (Yam and Cheng 1990).

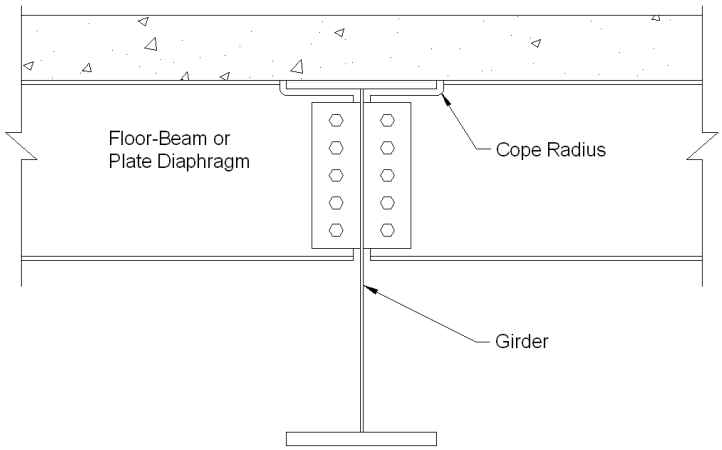

Figure 1-5 Floor-beam or plate diaphragm cope

Cracks form due to tensile stresses resulting from differential deflections of adjacent girders (Zwerneman et al. 1993). The combined effect of stress range and cope radius are the two most important factors that influence crack initiation life. It has been shown that the stress concentration factor increases with decreasing cope radius (Yam and Cheng 1990). In other words, a smaller cope radius at a corresponding stress range was shown to produce a shorter initiation life than a larger cope radius. Small cope radii exist because in the 1980s there

were no specific guidelines and recommendations in the American Institute of Steel Construction (AISC) LRFD Specification (1986) and AASHTO (1984) design codes for the design of coped beams under fatigue loading.

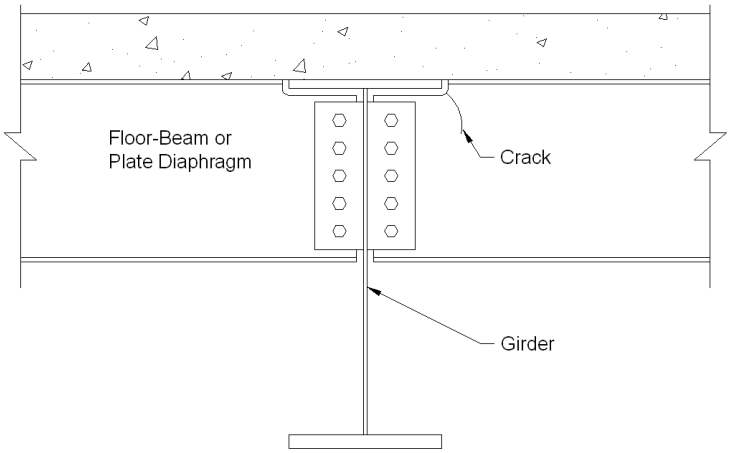

Figure 1-6 Crack at cope radius in floor beam-to-girder connection

1.3 SHELF PLATE WELDED TO GIRDER WEB

Diagonal lateral bracing is commonly used to transfer wind loads between adjacent girders. When this happens, the connection plates used to attach diagonal braces to the girder web intersect transverse stiffeners (shown in Figure 1-7). Because of this, welds connecting the transverse stiffener to the girder web and the lateral bracing to the girder web intersect. This intersection of welds is particularly vulnerable to fatigue cracks. At the time when the bridges that tend to experience this type of cracking were designed, it was common to allow these welds to intersect.

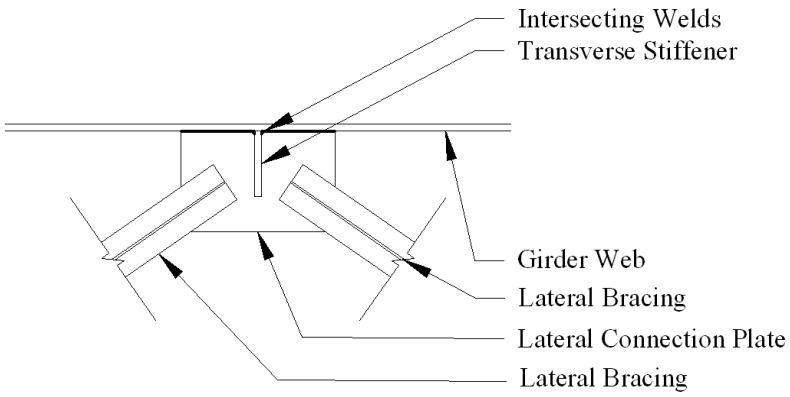

Figure 1-7 Lateral connection plate intersecting transverse stiffener (plan view)

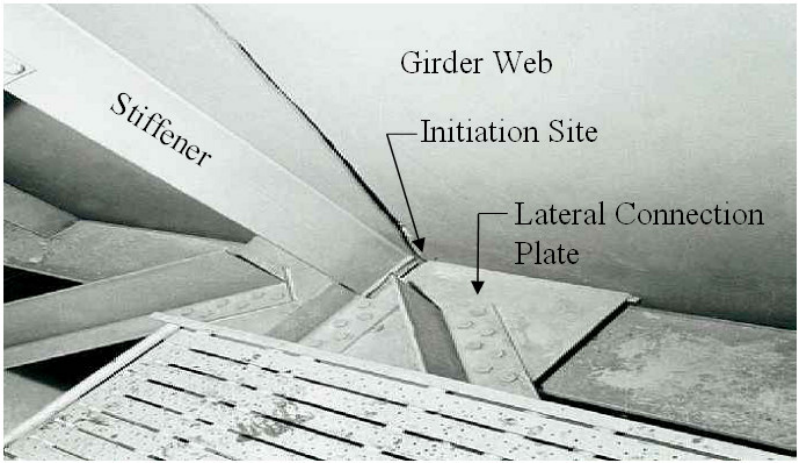

Figure 1-8 Crack initiation site (Fisher 1984)

1.4 PARTIAL LENGTH COVER PLATE

Older bridges commonly employ welded plates to the bottom flanges of girders intended to increase the flexural capacities of members. Plates are welded to the girder flange to increase the bending moment of inertia of the section, which allows the girder to carry increased flexural loads (Hassan and Bowman 1996).

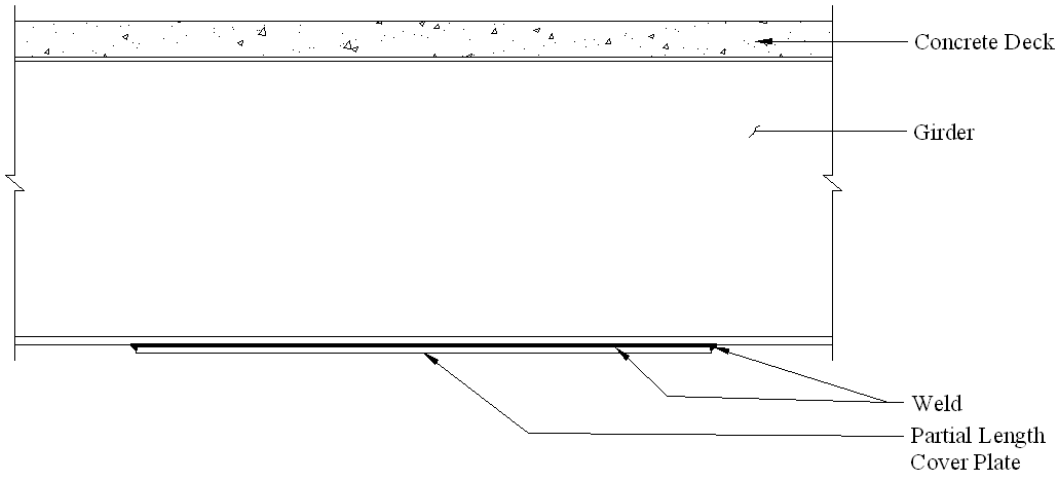

Figure 1-9 Partial length cover plate

Cracks tend to initiate at the weld toe at the ends of the cover plate, as shown in Figure 1-10. This detail corresponds to a Category E detail according to the AASHTO Bridge Specification (2002). Cracks have been shown to propagate through the girder flange and into the girder web (Fisher 1984).

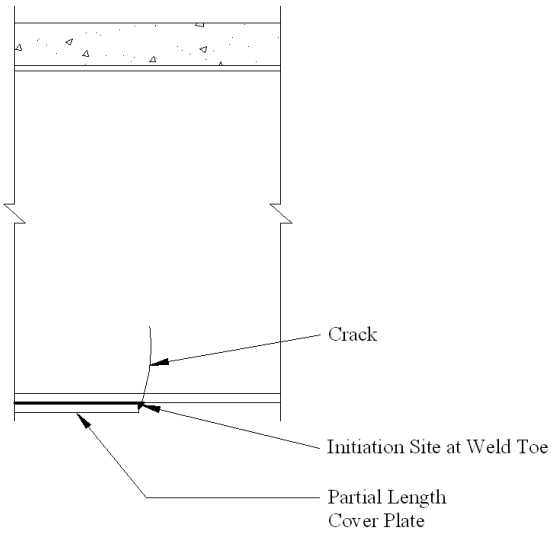

Figure 1-10 Crack initiation site at the end of a welded coverplate attached to a girder's bottom flange.

1.5 RETROFITTING SCHEMES

Some retrofitting schemes have been established either as general repair methods for many types of fatigue cracks or as specific repair techniques for the details described in Sections 1.1 through 1.4. In some instances fatigue repair methods developed for a particular type of detail are used in combination with general repair methods to extend fatigue life. Specific repair techniques are discussed in Sections 1.5.1 through 1.5.6.

1.5.1 DRILLED HOLES

Drilled holes are commonly used to arrest or slow growth of fatigue cracks in structures. The concept behind drilled holes comes from the idea that a smooth, circular shape produces a much lower stress intensity factor than the sharp edges of cracks. The stress intensity factor of drilled holes depends on the radius of the circle (larger diameters produce lower stress intensity factors) (Barsom and Rolfe 2006). This idea sparked research aimed at deriving an empirical equation to help engineers determine the minimum diameter of a crack-stop hole necessary to prevent re-initiation of fatigue cracks. The minimum hole diameter equation developed by Barsom and Rolfe is a function of several parameters.

The first parameter is the range of the stress intensity factor (ΔK_I). Stress intensity factors (K_I) are used to help characterize the stress field ahead of a sharp

crack based on crack location and size (Barsom and Rolfe 2006). There are empirical equations for many stress intensity factors given listed by Barsom and Rolfe (2006), and some are shown below for a few common crack situations.

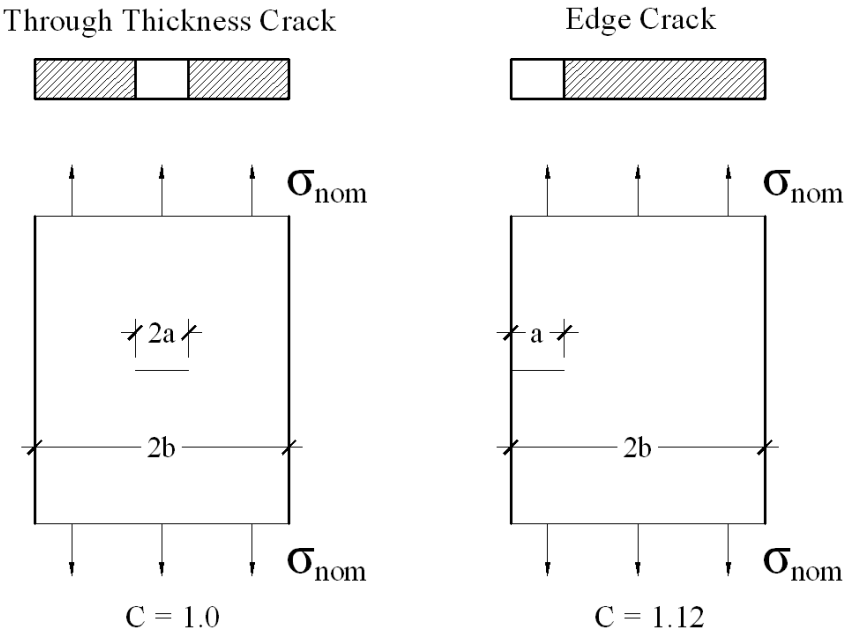

Figure 1-11 Through thickness and edge cracks in finite plates

Figure 1-11 shows crack locations and sizes, and Eqn 1.1 can be used to calculate the stress intensity factor (K_I) based on a nominal stress σ_{nom} away from the crack.

$$K_I = C \cdot \sigma_{nom} \cdot \sqrt{\pi a} \cdot f\left(\frac{a}{b}\right) \qquad \textbf{Eqn 1.1}$$

The factor *f(a/b)* is a function of the ratio of crack width to plate width, and these values are listed by Barsom and Rolfe (2006). This equation is based on principles of fracture mechanics assuming a constant stress. Fatigue cracking

occurs due to a stress range ($\Delta\sigma_{nom}$) in a structure, which can be used to calculate a stress intensity factor range (ΔK_I).

The stress intensity factor range (ΔK_I) calculated using Eqn 1.2 is the first factor used to help engineers proportion crack-stop holes. The second factor involves the tensile yield strength of the material (σ_y); this value can be determined from a simple tensile test.

$$\Delta K_I = C \cdot \Delta\sigma_{nom} \cdot \sqrt{\pi a} \cdot f\left(\frac{a}{b}\right) \qquad \textbf{Eqn 1.2}$$

Barsom and Rolfe (2006) recommended the following equation for a crack-stop hole diameter (2ρ) which was derived from empirical data for any system of units:

$$\frac{\Delta K}{\sqrt{\rho}} < 10\sqrt{\sigma_y} \qquad \textbf{Eqn 1.3}$$

Other research has been done on this topic based on the same variables discussed above. Fisher et al. (1990) recommend the following two equations for crack-stop hole diameters (2ρ) using the stress intensity factor range (ΔK_I) and the material tensile yield strength (σ_y).

$$\frac{\Delta K}{\sqrt{\rho}} < 10.5\sqrt{\sigma_y} \quad (for\ \sigma_y\ in\ MPa) \qquad \textbf{Eqn 1.4}$$

$$\frac{\Delta K}{\sqrt{\rho}} < 4\sqrt{\sigma_y} \quad (for\ \sigma_y\ in\ ksi) \qquad \textbf{Eqn 1.5}$$

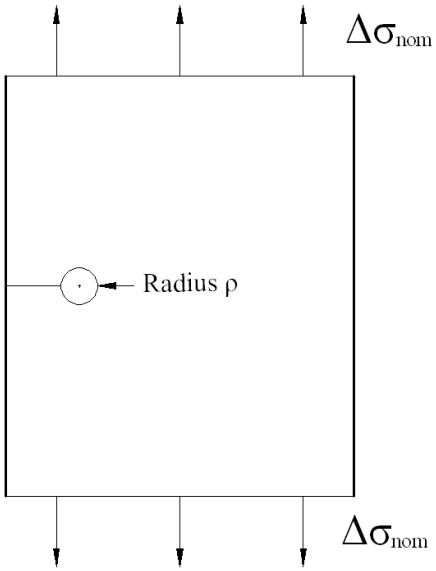

Figure 1-12 Crack-stop hole diameter sized using Eqn 1.3 to Eqn 1.5

Either of the equations suggested by Barsom and Rolfe (2006) or Fisher et al. (1990) can be used to calculate the diameter (2ρ) of a crack-stop hole to prevent crack re-initiation. Different diameters of crack-stop holes can be calculated using Eqns 1.3 to 1.5, but the equations have been known to produce properly sized crack-stop holes to prevent crack re-initiation.

1.5.2 COLD EXPANSION

Crack-stop hole diameters calculated in section 1.5.1 are often too large to be drilled in the actual structure due to space limitations. To account for this, drilled holes are commonly undersized; meaning the diameter of the hole is less than the minimum required to prevent crack re-initiation. Theoretically, a crack

will re-initiate from the undersized drilled hole, so cold expansion of undersized holes can be used as a complement to the former technique.

Cold expansion techniques have been used extensively in the aerospace industry to enhance the fatigue life of in-service planes for the last 40 years (Stefanescu et al. 2004), but this process is also used in other fields. The process begins with a radial expansion of a hole (on the order of a 3-5%) creating a radial plastic flow of material around the hole (Leon 1998). After expansion, spring-back of surrounding elastic material introduces a residual compressive stress field adjacent to the undersized hole (Stefanescu et al. 2004). This residual compressive field helps to counteract the applied tensile stress which is responsible for crack initiation and growth (Ozelton and Coyle 1986).

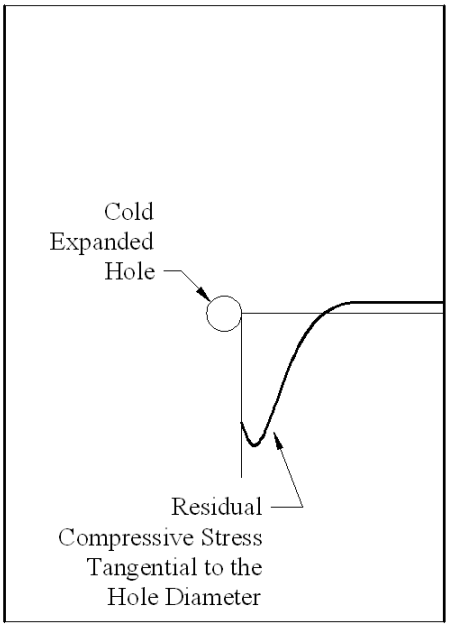

Figure 1-13 Residual compressive tangential stress on cold-expanded hole

1.5.3 HAMMER PEENING

Another scheme that induces compressive stresses at weld toes involves using an impact hammer at high frequency on the metal surface. This procedure is known as peening which is defined as a process that cold works the surface of the metal to improve its material properties. Maddox (1998) reports that the fatigue life of welded joints could be twice as long with hammer peening. However, hammer peening is known to be incredibly noisy, and a number of passes using the hammer must be performed because of the inconsistencies with impacting the same area on the weld toe (Hacini et al. 2008).

1.5.4 ULTRASONIC IMPACT TREATMENT

Ultrasonic Impact Treatment (UIT) is a method similar in application to hammer peening in which residual compressive stresses are induced at weld toes of structures in addition to smoothing geometric discontinuities in the weld that create stress concentrations (Vilhauer et al. 2008). This method was developed in the late 1960s and early 1970s by Russian researchers as an alternative to hammer peening. The benefits of UIT over hammer peening include low equipment weight, low operating noise, high efficiency, and low cost. The UIT procedure results in complete loss of some tensile residual stresses and introduction of compressive residual stresses (Ye et al. 2006).

1.5.5 SHOT PEENING

In addition to hammer peening and ultrasonic impact treatment, another procedure to introduce residual compressive stresses in structural elements is shot peening. This method, unlike hammer peening and UIT, does not require placing a tool on the surface of the material to introduce residual compressive stresses.

The shot peening process is completed by shooting small particles (steel, ceramic, or glass spheres) at high velocities at the metal surface. The shot stream energy of the particles (product of mass and velocity) introduces a residual compressive stress on the material's surface which improves the fatigue performance (Breuer 2007). Since deeper layers of compression have a greater influence on fatigue enhancement, the shot velocity needs to be high which creates surface deformations (Breuer 2007). These surface deformations may not be ideal to preserve the aesthetic appeal of bridges.

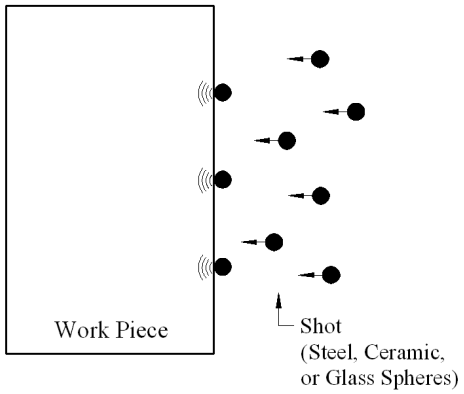

Figure 1-14 Shot peening

1.5.6 CARBON FIBER PATCH

Composite materials have been used in the aerospace industry for a number of years to increase the fatigue performance of aircrafts. This technology is starting to be used for civil applications to improve the fatigue performance of steel bridges as well. Research has shown that Carbon Fiber Reinforced Polymer (CFRP) patches can be used over existing cracks to retard crack growth (Bassetti et al. 2000).

CFRP patches are used extensively in the aerospace industry for a number of reasons. These reasons include high strength to stiffness ratio of the composite materials which results in lightweight assemblies, directional dependence of the material properties (the engineer can orient the fibers in whichever direction is most advantageous), and formability (Okafor et al. 2005).

The concept behind CFRP patches relates to linear-elastic fracture mechanics. In an unreinforced structure with an existing crack, a plastic zone is created due to the presence of a stress range (shown in Figure 1-15); this plastic zone is the cause of crack propagation due to opening and closing of the crack from applied cyclic stresses.

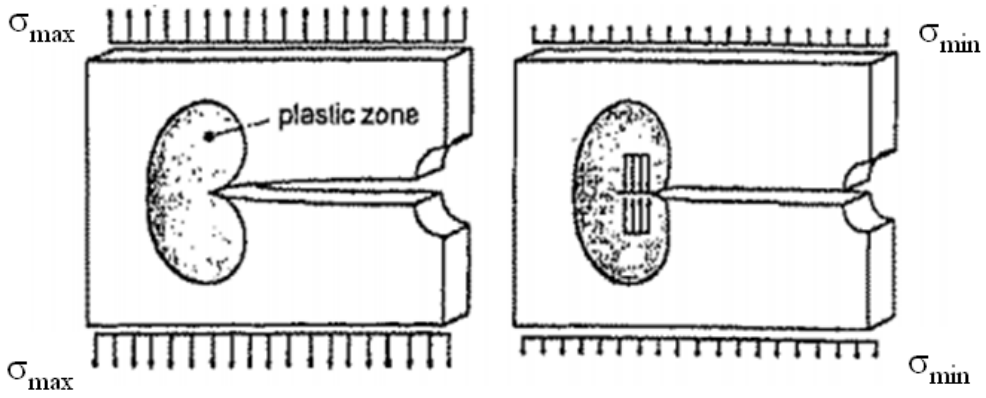

Figure 1-15 Plastic zone (Bassetti et al. 2000)

From fracture mechanics, it is known that crack growth can be slowed or retarded by reducing the opening of the crack. Patches made of composite materials can be used to reduce this effect, which lowers ΔK (Bassetti et al. 2000). CFRP patches are attached to the metal surface over the crack such that the fibers are orientated perpendicular to the crack; the orientation of the fibers is important to reduce the crack opening (Bassetti et al. 2000).

The stiffness of the CFRP patch relative to the stiffness of the base material is the most important parameter for limiting the opening of the fatigue crack. For this reason CFRP patches are much more effective when bonded to aluminum than when bonded to steel. Carbon fibers are often pre-stressed to increase the stiffness of CFRP patches (Bassetti et al. 2000).

As discussed previously, CFRP patches show strong potential for improving fatigue performance of structures by reducing the crack opening displacements. Research has shown that CFRP patches reduce the stress at the

crack tip by up to 50% in aluminum (Domazet 1996). There are a number of barriers to its practical implementation that have yet to be overcome such as galvanic corrosion between the composite and steel material, bond strength, and effectiveness of reducing cyclic, concentrated stresses in steel.

1.5.7 TRANSVERSE STIFFENER WEB GAP RETROFITS

The fatigue problem described in Section 1.1 can be reduced or eliminated using a few established retrofit measures in addition to the schemes described in Sections 1.5.1 through 1.5.6. The most successful retrofit measure involves attaching the connection plate to the top flange.

In the positive moment region of bridge girders, where the top flange is in compression, a common retrofit measure calls for the connection plate to be welded to the top flange to create a positive attachment (Figure 1-16). This retrofit is effective because fixing the connection plate to the top flange significantly reduces secondary stresses due to distortion. It is important to note that welding to the top flange can only be done in the positive moment region because the compressive stresses in the flange do not create a fatigue-sensitive detail (Roddis and Zhao 2003).

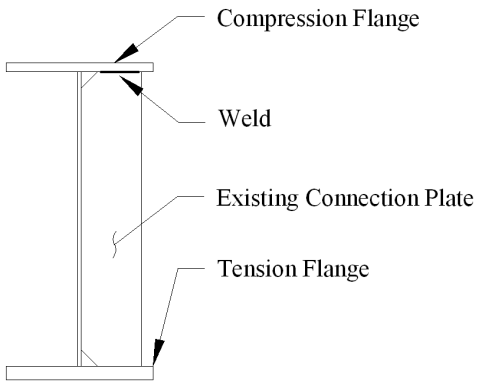

Figure 1-16 Positive moment region – connection stiffener welded to compression flange

In the negative moment region, where the top flange is in tension, the connection plate cannot be welded to the top flange because a fatigue-sensitive detail is created. In order to overcome this limitation, a back-up stiffener may be used to stiffen the connection. Another plate is welded on the opposite side of the web from the connection plate (Figure 1-17). Also, the connection plate is welded to the bottom (compression) flange to stiffen the connection against secondary stresses (Roddis and Zhao 2003).

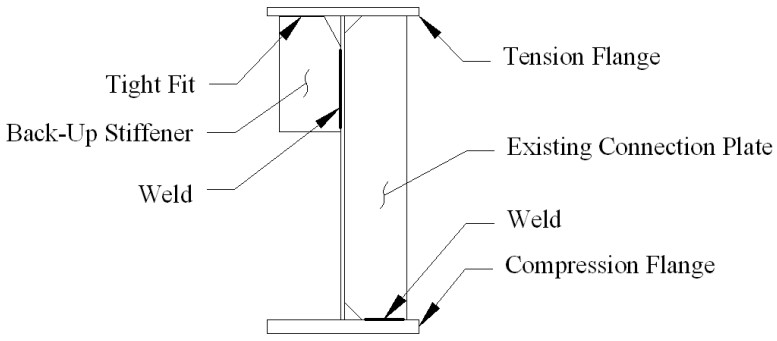

Figure 1-17 Negative moment region - back-up stiffener

Other schemes can be used to create a positive attachment between the connection plate and top flange in both the positive and negative moment regions. Angles or WT shapes can be bolted to the connection plate and either bolted or adhesively bonded to the top flange to reduce secondary stresses due to differential deflections of adjacent girders, as shown in Figure 1-18.

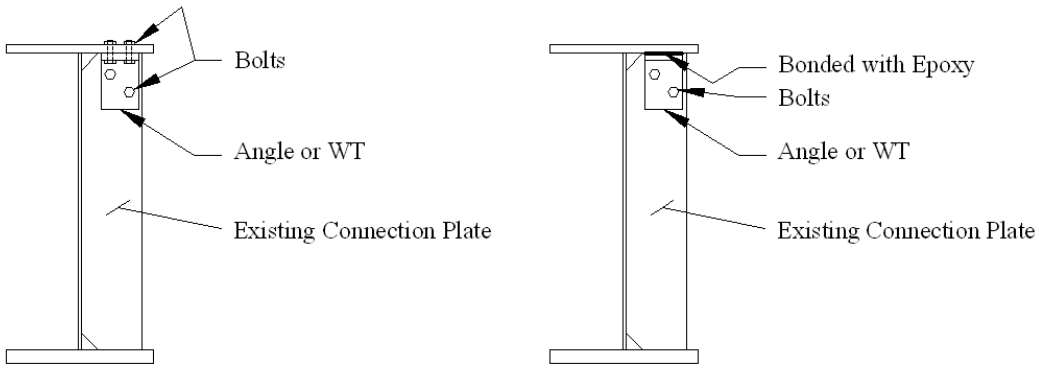

Figure 1-18 Positive attachment – between connection stiffener and top flange provided by bolting or epoxy bond

Using adhesives to bond the angle or WT shape to the top flange has many advantages over using bolts. Bolts require removal of the concrete deck for installation which entails partial closure of the bridge; using adhesives eliminates this problem because the removal of the concrete deck is not required (Hu et al. 2005). A different scheme that is similar to these utilizes studs that are welded to the bottom face of the top flange and can be used without the removal of the concrete deck.

Other retrofit schemes exist that do not require a positive attachment to the top flange of the bridge girders. One alternative calls for softening the connection

by increasing the web gap length to reduce secondary stresses in the web-gap region (Fisher and Keating 1989). A slot is created by drilling a hole in the connection plate and removing the top portion of the connection plate by flame cutting as shown in Figure 1-19. Fisher and Keating (1989) recommended a gap length of 11.8 in. (300 mm) to properly release the connection.

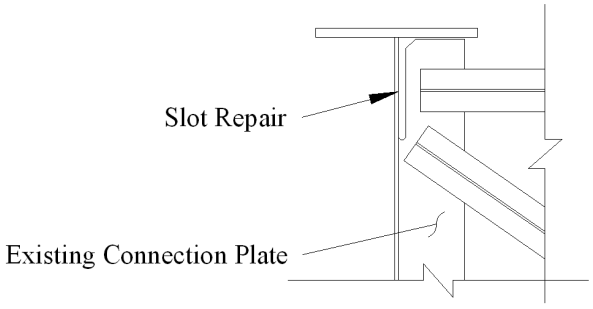

Figure 1-19 Slot repair in connections stiffener

Fisher and Keating (1989) also stated that "increasing the flexibility of the gap region will usually be sufficient to reduce the bending stresses that are driving the crack." However, Zhao and Roddis (2007) reported that the slot repair actually tends to introduce higher magnitude fatigue stresses in the web-gap, which is believed to cause crack re-initiation and propagation found in repaired details. Because of these two conflicting statements, there seems to be some controversy about how effective the slot repair retrofitting scheme is on reducing web-gap stresses.

A third retrofitting scheme that completely eliminates secondary stresses due to differential deflections of adjacent girders calls for removal of the intermediate bracing members. Although not always practical, removing lateral

bracing eliminates web-gap stresses because it eliminates the driving forces that cause the out-of-plane displacements. It should be noted that removing intermediate braces reduces load sharing between girders, which increases the longitudinal stresses of the individually loaded girders. Stallings et al. (1996), however, concluded that the increased girder stresses are not likely to exceed design-level stresses calculated using the AASHTO Code by a meaningful margin.

1.5.8 INSUFFICIENT COPE RADIUS RETROFIT

Since a small cope radius is one of the most important factors for the development of fatigue cracks in the detail described in Section 1.2, an obvious retrofit measure would be to increase or completely eliminate the cope. This can be done by tapering the floor-beam or diaphragm as shown in Figure 1-20. Fisher (1984) called for the use of a crack-stop hole (described in Section 1.5.1) in addition to tapering the floor-beam or diaphragm at the cope to eliminate the stress concentration at an existing crack tip. Also, Fisher (1984) recommended adding plates to the taper to act as a flange with the goals of restoring the bending resistance of the coped section and reducing the stresses below the fatigue limit.

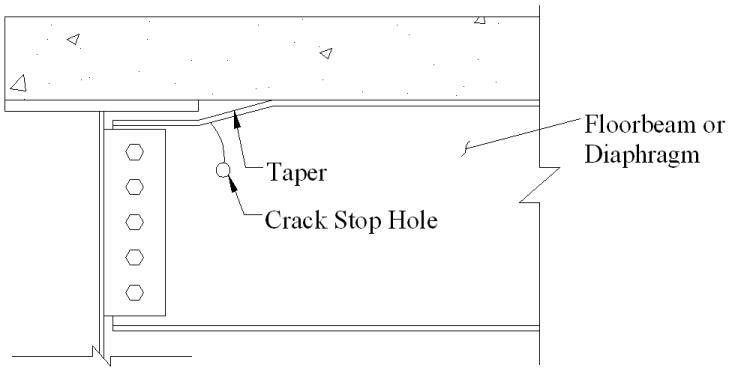

Figure 1-20 Insufficient cope radius retrofit

1.5.9 SHELF PLATE WELDED TO GIRDER WEB RETROFIT

The main problem with the detail described in Section 1.3 originates from the intersecting welds of the lateral connection plate and transverse stiffener. The obvious solution to retrofit this detail is to eliminate the weld intersections. Fisher and Keating (1989) recommended the retrofit solution shown in Figure 1-21, which eliminates the weld intersection that causes cracks to initiate.

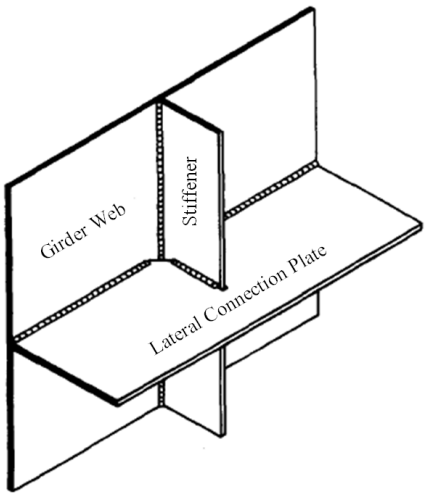

Figure 1-21 Shelf plate welded to girder web retrofit (Fisher and Keating 1989)

1.5.10 PARTIAL LENGTH COVER PLATE RETROFIT

The detail described in Section 1.4 has commonly experienced cracks that tend to initiate at the weld toe of the partial length cover plate. To prevent or slow crack growth, a few schemes were developed to reduce the stress range at the weld toe, lowering the stress intensity factor (ΔK). The first retrofitting scheme, recommended by Hassan and Bowman (1996), called for a bolted splice plate to redistribute the forces around the weld toe as shown in Figure 1-22.

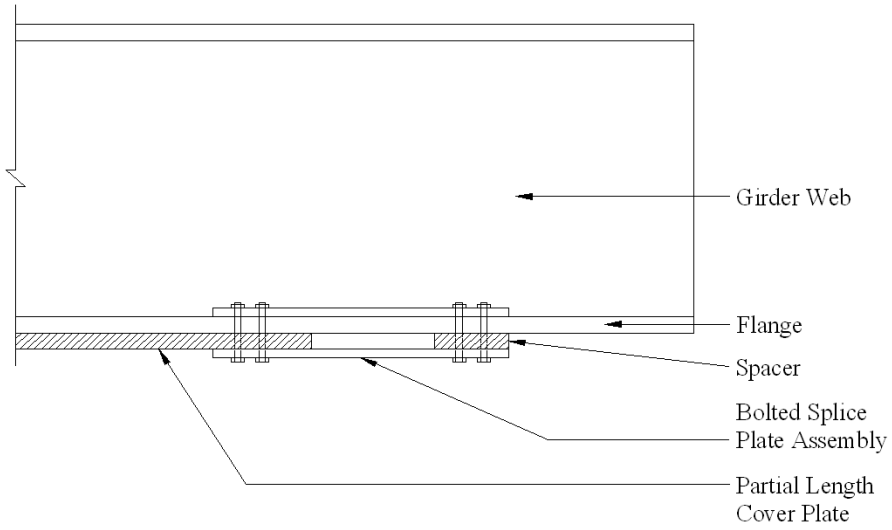

Figure 1-22 Partial length cover plate retrofit

Another retrofitting scheme, developed at the University of Kansas by Kaan et al. (2008), called for the use of carbon fiber reinforced polymers (CFRP). This scheme used the CFRP overlays to stiffen the detail prone to fatigue cracking, producing an alternative load path reduces the magnitude of stress range at the weld toe.

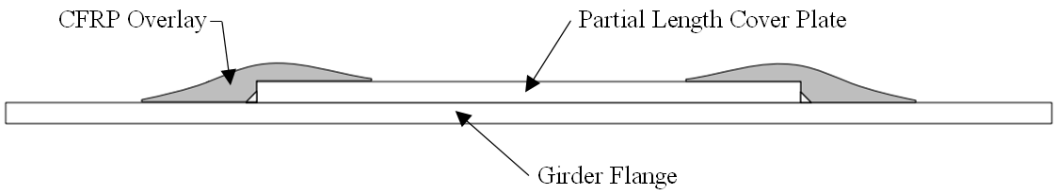

Figure 1-23 Partial length cover plate retrofit - CFRP overlay (Kaan 2008)

Experimental and analytical research performed at the University of Kansas has shown that these CFRP overlays can significantly increase the fatigue life of this particular detail (Kaan 2008).

As previously discussed, the fatigue repair measures described in Sections 1.5.1 through 1.5.6 can be used in combination with any of the detail-specific repairs described in Sections 1.5.7 through 1.5.10.

This study is focused on the transverse stiffener web-gap detail described in Section 1.1. The scope of the investigation involves using finite element models to understand the magnitude of web-gap stress, and to evaluate the effectiveness of various retrofitting schemes. A new retrofitting scheme using carbon fiber reinforced polymers is developed and compared with other retrofit measures documented in the literature.

Full scale testing of the transverse stiffener web gap detail will be performed in the future to evaluate the effectiveness of the retrofit measure developed as part of this study.

CHAPTER 2 FINITE ELEMENT MODELS

Finite Element Analyses (FEA) were performed to develop a better understanding of the distribution of stresses in the web-gap region of the detail described in Section 1.1, particularly in the area above the transverse stiffener connection plates. The Finite Element Analysis software ABAQUS v.6.8-2 was used to perform the analyses. The first step in FE modeling was to select a bridge geometry (girder sections, span, spacing, and brace type) to use as a basis for the models of the study. The bridge configuration selected was similar to a specimen that will be tested at the structural engineering laboratory at the University of Kansas. This bridge configuration is based on an example bridge published by the American Iron and Steel Institute (AISI).

2.1 AISI EXAMPLE BRIDGE

This design example (Eaton et al. 1997) illustrates the design of a skewed, simple span bridge consisting of four (4) I-shaped composite girders each with a span of 161 ft. The girders are spaced at a distance of 13 ft. with a concrete slab thickness of 10 in. including a 1/2 in. integral wearing surface. The structural steel is ASTM A709, Grade 50W uncoated weathering steel with a yield strength of 50 ksi. The specified concrete compressive strength is 4.5 ksi, corresponding to a modular ratio, n, of eight (8). A cross section of the AISI Example Bridge is shown in Figure 2-1 (Eaton et al. 1997).

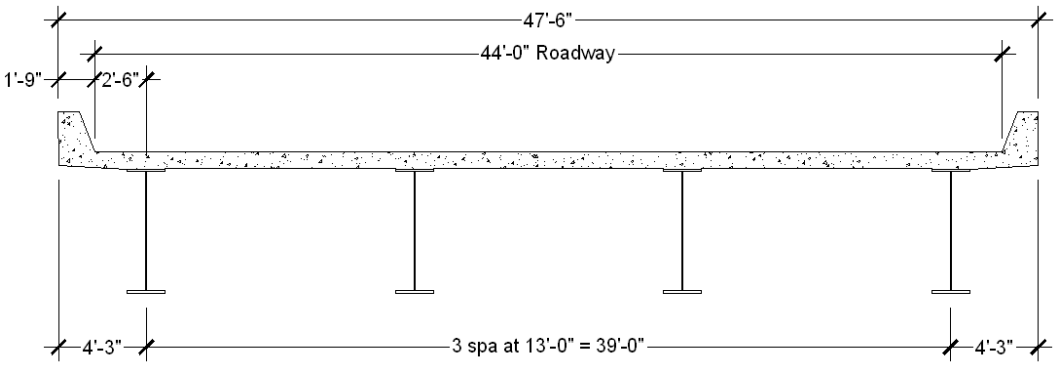

Figure 2-1 AISI example bridge cross section

Along with the above cross section, Figure 2-2 shows the girder dimensions. The top flange has dimensions PL 1 1/4 in. x 22 in.; the web has dimensions PL 1/2 in. x 69 in.; the bottom flange has dimensions PL 2 in. x 22 in.

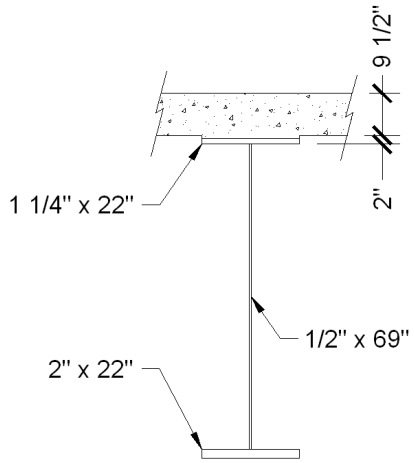

Figure 2-2 AISI example bridge girder dimensions

As discussed earlier, this AISI Example was designed with skewed supports; the skew angle is shown in Figure 2-3.

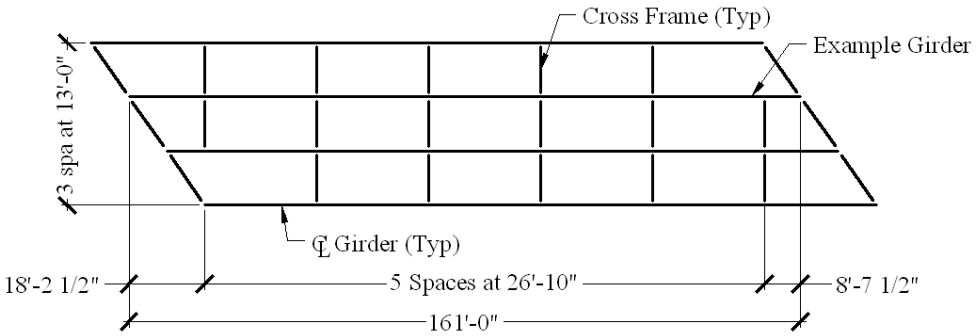

Figure 2-3 AISI example bridge - plan view

The girder section and spacing in this AISI Example was emulated in the bridge configuration that will be tested at the University of Kansas; some changes were made to the bridge design to accommodate available testing area.

2.2 UNIVERSITY OF KANSAS TEST BRIDGE CONFIGURATION

Although full-scale testing might provide a direct comparison to bridges in the national highway inventory susceptible to distortion-induced fatigue, testing of reduced-scale systems is more practical. Few changes were made to the AISI Example Bridge to develop the test specimen that will be used in the experimental phase of this research project.

2.2.1 GIRDER SPACING, SPAN, AND DIMENSIONS

The configuration adopted for the test bridge has three (3) girders spaced at 6 ft. on center. This spacing is approximately half that used in the AISI Example Bridge (13 ft.). Girder and slab thickness dimensions were also scaled

down by a factor of 2 to maintain similitude laws between the two systems. The span, on the other hand, could not be practically scaled by the same factor. A 27 ft. span length was chosen for the experimental study to meet space constraints and to maintain the cost of the specimen within the budget for the project. The 27 ft. span was also used in the finite element models.

For the initial testing phase performed at the University of Kansas, right bridges (without skew) were modeled to understand the behavior of stresses in the web-gap region without the complicating factor of skew. Section views and a plan view of the test setup are shown in Figure 2-4 through Figure 2-6.

2.2.2 CROSS FRAME DIMENSIONS

Section sizes or design calculations for the intermediate cross frames (not at bridge supports) on the full-scale AISI Example Bridge were not given. Because of this, other sources were used as a reference for proportioning that gave a design procedure for sizing intermediate cross frames. Elliot and LeBeau (1997) reported that intermediate cross frame members should be proportioned based solely on slenderness because these braces do not transfer lateral loads to the supports. The slenderness limit (kl/r) is not to exceed 140, as shown in Eqn 2.1, where kl is the effective length of the brace and r is the radius of gyration.

$$\frac{kl}{r} \leq 140 \qquad \textbf{Eqn 2.1}$$

Before proportioning the braces, it was important to decide which brace configuration (K-type or X-type) would be utilized. Criteria by the National Steel Bridge Alliance (NSBA) notes that if the ratio of girder spacing to girder depth is greater than 1.5, then K-braces should be used; otherwise, the use of X-braces is allowed (NSBA, accessed 2009). Because the girder spacing to depth ratio of the full-scale AISI Example Bridge is greater than 1.5, K-Braces were used for the FE models

$$\frac{Girder\ Spacing}{Girder\ Depth} \geq 1.5 \quad \rightarrow \quad K-Braces$$

$$\frac{Girder\ Spacing}{Girder\ Depth} < 1.5 \quad \rightarrow \quad X-Braces$$

Braces were designed for the full-scale prototype AISI Example Bridge, and then scaled by a factor of two for the KU Test Bridge FE models. Based on the length of the braces required in the AISI Example Bridge, full-scale braces consisted of WT5x15 shapes for all sections of the brace.

Connection plates were also scaled from the full-scale AISI Example Bridge. Although connection plate sizes were not given in the design calculations, transverse stiffener sizes were provided (thickness = 7/8 in.). Because of this, the transverse stiffener thickness was scaled by a factor of two and the same dimension was used for the connection plate thickness for the KU Test Bridge.

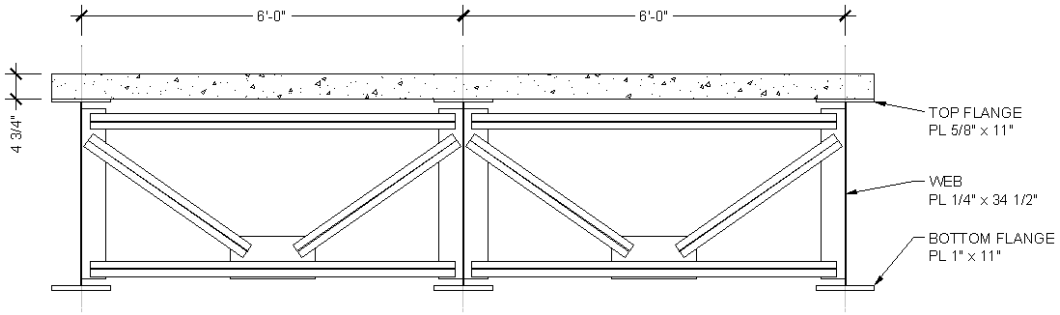

Figure 2-4 KU test bridge section, shown with k-brace option

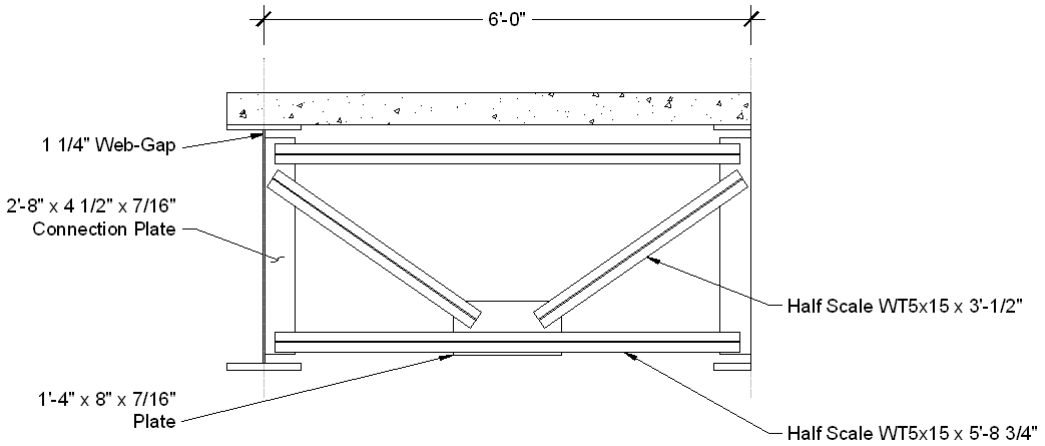

Figure 2-5 KU Cross frame and connection plate sizes (half section) (k-brace option)

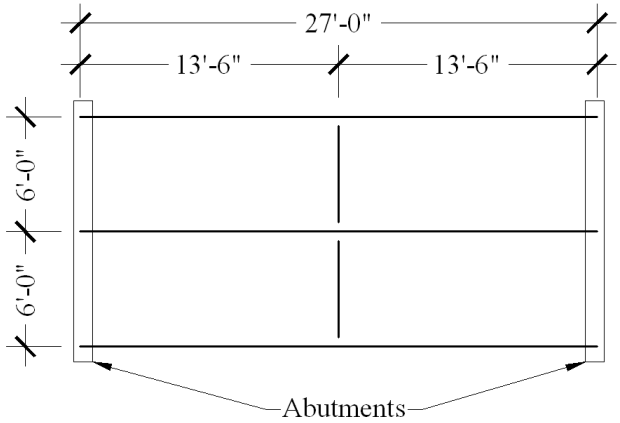

Figure 2-6 KU test bridge plan view

Along with this connection plate thickness, different connection plate geometries were investigated using finite element models to study the effect of

connection plate configuration on web-gap stresses. Two geometries, in particular, were modeled and are shown in Figure 2-7 (a) and (b). Also, a few established retrofitting techniques were investigated to understand the effectiveness of such schemes on the KU Test Bridge configuration as shown in Figure 2-8 (a) and (b).

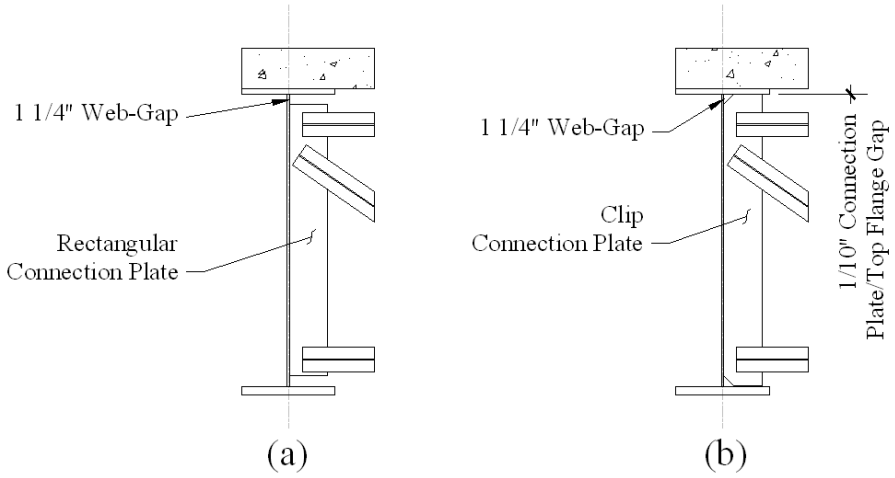

Figure 2-7 Non-retrofitted connection plate geometry: (a) rectangular connection plate; (b) clip connection plate.

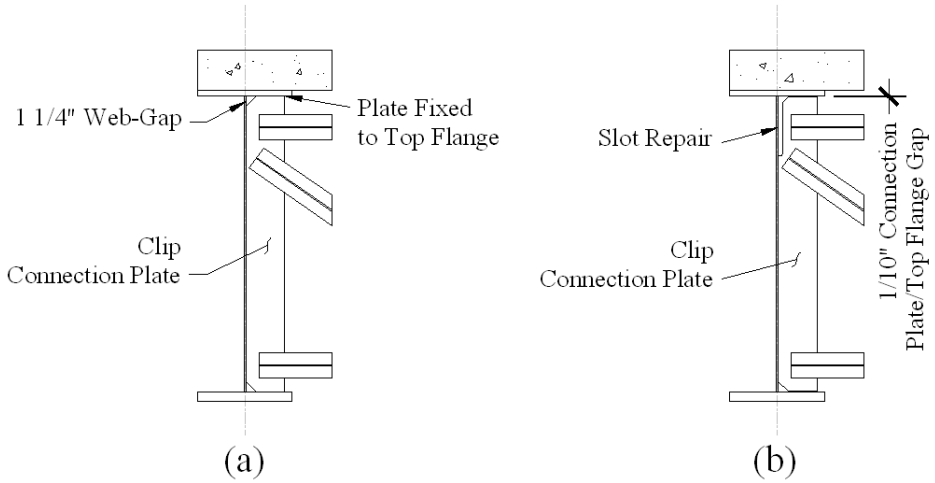

Figure 2-8 Retrofitted schemes connection plate geometry: (a) fixed connection; (b) slot repair.

2.3 FINITE ELEMENT MODEL PROCEDURE

Finite Element (FE) models of the University of Kansas Test Bridge Configuration shown in Figure 2-4 through Figure 2-6 were created using ABAQUS v.6.8-2. The manner in which the FE models were assembled is described in the following sections.

2.3.1 PARTS AND INSTANCES

Parts were used to define section geometries of the structure. The parts in this particular model (girders, braces, connection plates, etc.) were built using 3D solid elements. The procedure that was used to assemble the individual parts of the test bridge assembly was intended to minimize the number of elements used in the model (described in Section 2.3.6). For example, the bridge girders and deck were divided into three sections to make finer meshing easier in the region where the connection plate intersected the girder web (Figure 2-9). There were a total of three part instances in the entire KU Test Bridge assembly, discussed below:

- *Girders and Concrete Deck – Inside*: This part consisted of the three girders and concrete deck merged together. Merging the concrete deck with the bridge girders allowed the two materials to interact together without the use of tie constraints (minimizing the number of tie constraints allowed for the use of more elements in the web-gap region). This part had a total longitudinal length of 4 ft.

- *Girders and Concrete Deck – Outside*: This part composed the remainder of the girder and concrete deck length. The total length of each individual section (on each end of the span) was 11 ft. – 6 in.
- *Braces*: The entire brace system was merged in this part; the half-scale WT5x15 braces were merged to the connection plates. Again, merging the braces to the plates eliminated the need for tie constraints (section 2.3.4).

The KU Test Bridge Assembly was built using these three part instances (shown in Figure 2-9 and Figure 2-10). These three instances were able to interact together with the use of tie constraints discussed in 2.3.4.

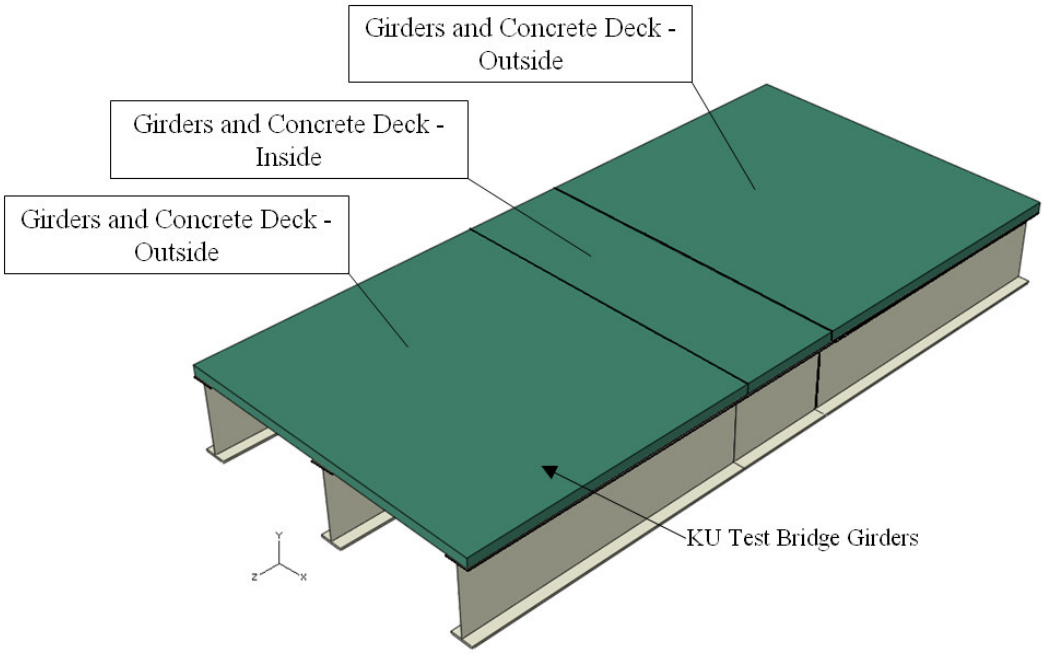

Figure 2-9 "Girders and Concrete Deck" part instances (braces are not visible)

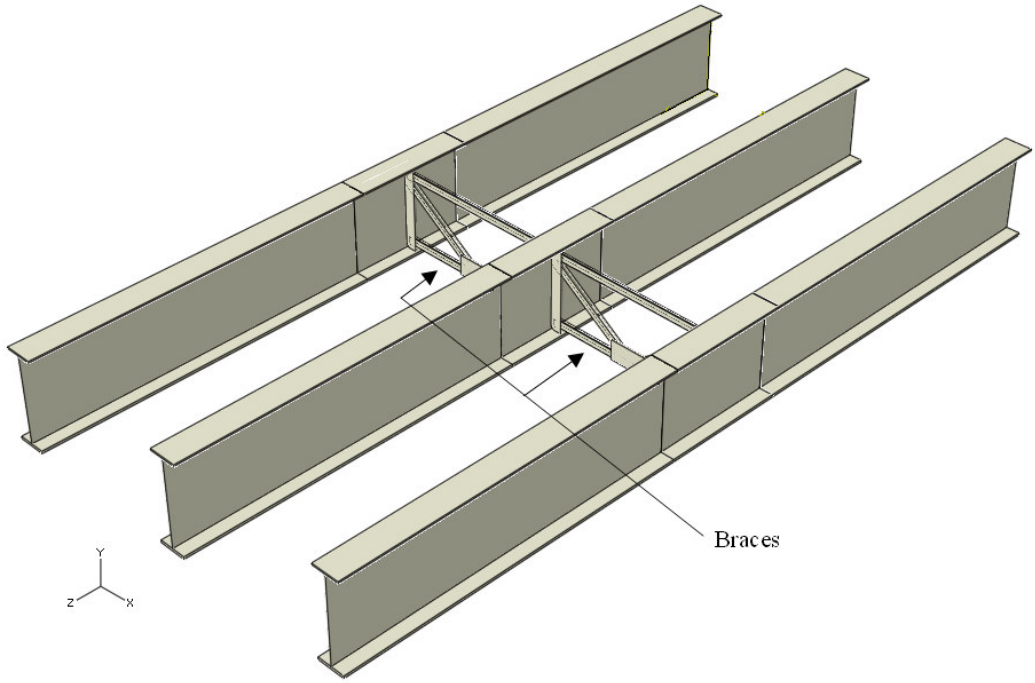

Figure 2-10 "Braces" part instance (concrete deck removed)

2.3.2 MATERIAL PROPERTIES AND SECTIONS

Material properties for concrete and steel were defined in the property module of ABAQUS 6.8-2. Only linear-elastic material properties were defined for these analyses; no plastic or non-linear behavior was defined for any of the FE models. The linear-elastic material properties for both the steel and concrete are defined below.

- Steel: An isotropic material was defined with a modulus of elasticity of 29,000 ksi and a Poisson's ratio of 0.3.

- Concrete: Based on the assumption of normalweight concrete with a compressive strength of 4,000 psi, the modulus of elasticity was calculated using the American Concrete Institute (ACI) Building Code (ACI 2008):

$$E_c = 57,000\sqrt{f_c'}\ psi \qquad \textbf{Eqn 2.2}$$

  E_c was calculated in psi with f'_c also in psi. An isotropic material was defined with this modulus of elasticity and a Poisson's ratio of 0.15. It is worth noting that actual concrete behavior does not act as an elastic material with the dimensions of the slab because the tensile strength of the concrete is much less than its strength in compression and cracking is expected to occur due to bending of the slab. A more precise modeling of the behavior of the concrete would result in a lower flexural stiffness of the slab. Because the flexural stiffness of the slab is small compared with the stiffness of the cross frames, this effect was not considered to be significant enough to warrant the added computational cost of nonlinear analyses.

Solid-homogenous sections with the properties described were assigned to the corresponding regions of the KU Test Bridge.

2.3.3 LOADING STEPS

For each of the FE models, a single loading step was created to simulate the application of a point load by a hydraulic actuator. A general, static load step

was defined in ABAQUS to apply the point load with a time increment of 1.0 seconds. The applied load is described in Section 2.3.5.

2.3.4 PART INSTANCE INTERACTIONS

In order for the part instances described in Section 2.3.1 to behave correctly, part interactions had to be defined. Because there should be no relative movement between the part instances, tie constraints were used to "fuse" the instances to one another. First, the two part instances corresponding to the girders and the concrete had to be tied together. This was accomplished by using two different surface-to-surface tie constraints between the part instances designated "Girders and Concrete Deck – Outside" and "Girders and Concrete Deck – Inside" as shown in Figure 2-11.

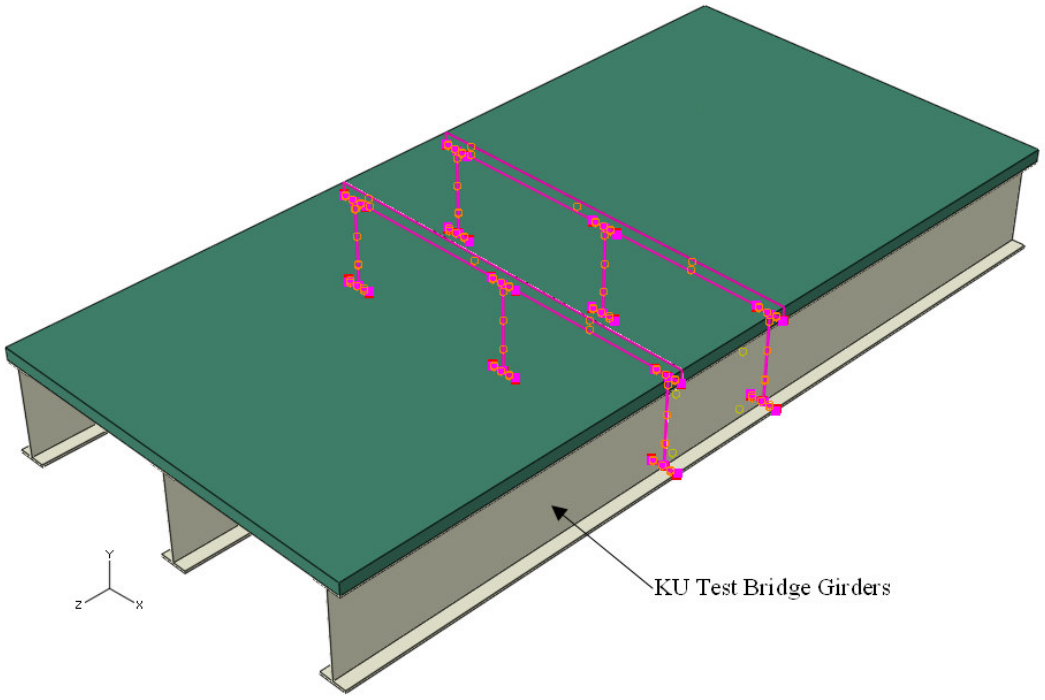

Figure 2-11 Tie constraints on KU test bridge girders (braces not visible)

The part instance designated “Braces” had to be tied to the part instance designated “Girders and Concrete Deck – Inside”. Four different surface-to-surface tie constraints were used to fuse the girder webs to the connection plate as shown in Figure 2-12.

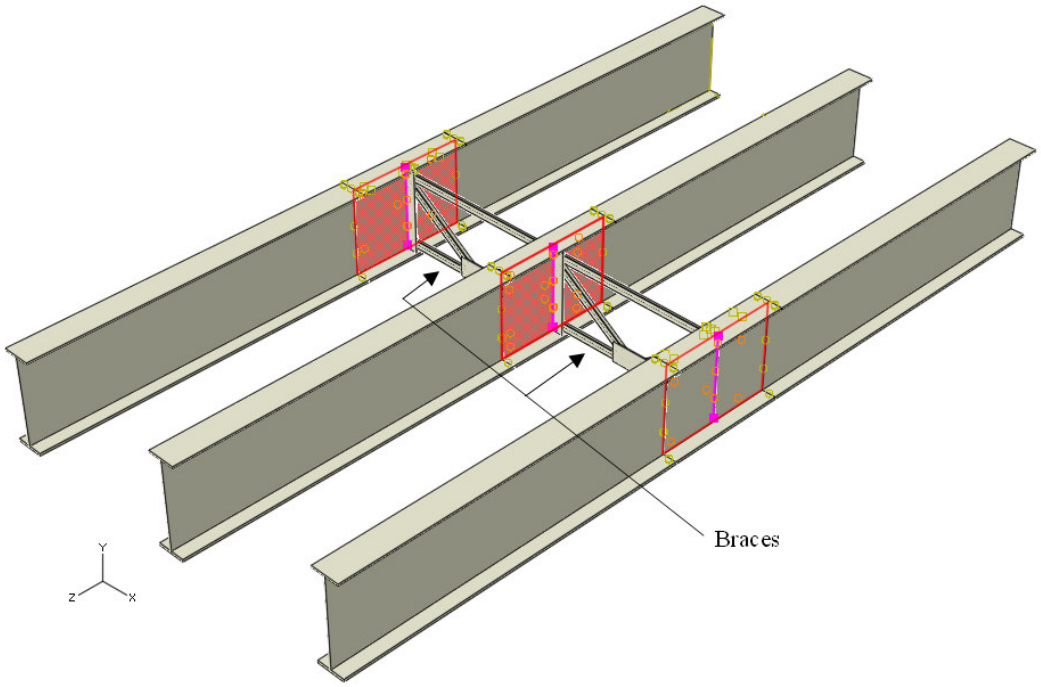

Figure 2-12 Tie constraints on braces with girder webs (concrete deck removed)

In the case where the connection plate was fixed to the top and bottom girder flanges as a retrofit, as shown in Figure 2-8, additional tie constraints were used to tie the connection plate to the top and bottom girder flanges.

2.3.5 LOADING AND BOUNDARY CONDITIONS

A vertical load of 100 kips was applied in the finite element models at midspan of the interior girder. To avoid concrete crushing and high element distortions, the 100 kip load was distributed as a pressure load over a one square foot area which resulted in a pressure load of 694.4 psi applied at midspan of the interior girder (Figure 2-13).

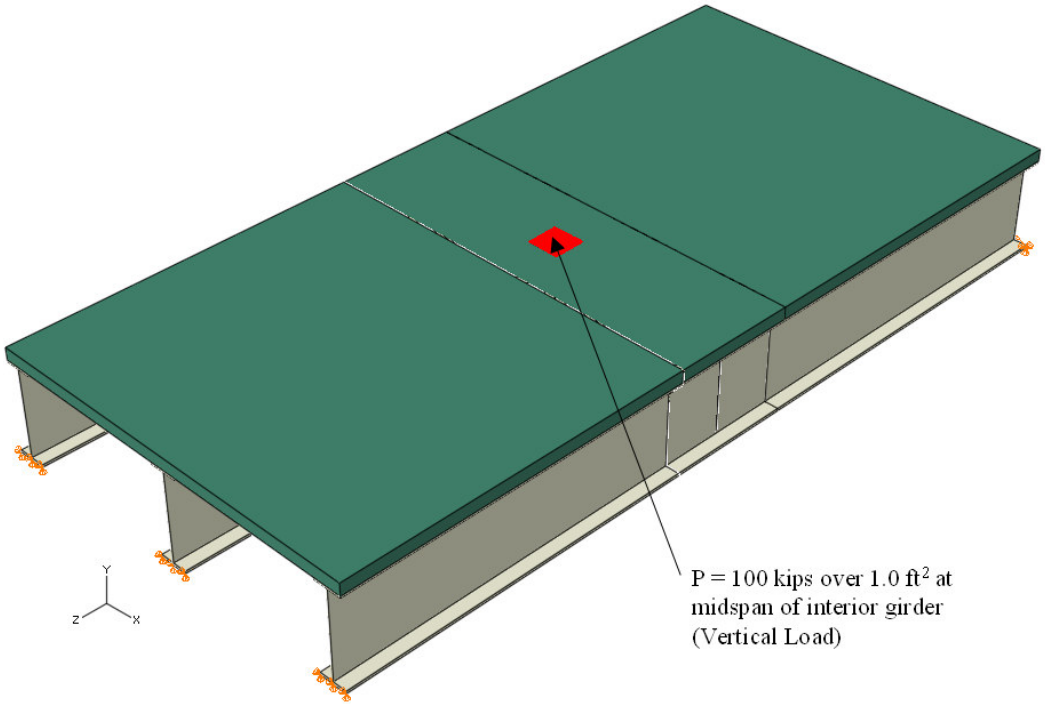

Figure 2-13 100 kip actuator load at midspan of interior girder

Boundary conditions used in the FE model simulated a pin and a roller support at each end of the bridge girders (Figure 2-13). A pin support (constraint in the x-, y-, and z- directions) was used on the bottom of the bottom flange at one end of the bridge girders, and a roller support (constraint in the x- and y- directions, free translation in the z- direction) was used on the bottom of the bottom flange at the other end of the bridge girders. Only the bottom of the bottom flange was selected for boundary conditions to allow for rotations at the supports.

2.3.6 MESHING

Before meshing and seeding were performed in ABAQUS v.6.8-2, the three part instances were partitioned so automatic meshing could be utilized. Partitioning was done because it is important to try to achieve elements with adequate aspect ratios; square elements produce better results than elements in which one of the dimensions is much larger than the other dimension. All of the part instances in the FE models were partitioned to maintain reasonable aspect ratios.

After partitioning was completed, mesh seeds had to be defined for the part instances so the automatic meshing algorithm had an established set of criteria to define the size of the elements. A consistent seeding scheme was used in each of the FE models so that proper comparisons could be made between the different models. The seeding scheme was as follows (the purple circles in the Figures 2.14 through 2.16 represent elemental seeds):

- *Girders and Concrete Deck – Outside Part Instance*: A single seed size was used for this entire part instance. A seed size of 3.5 in./element was used, as shown in Figure 2-14.

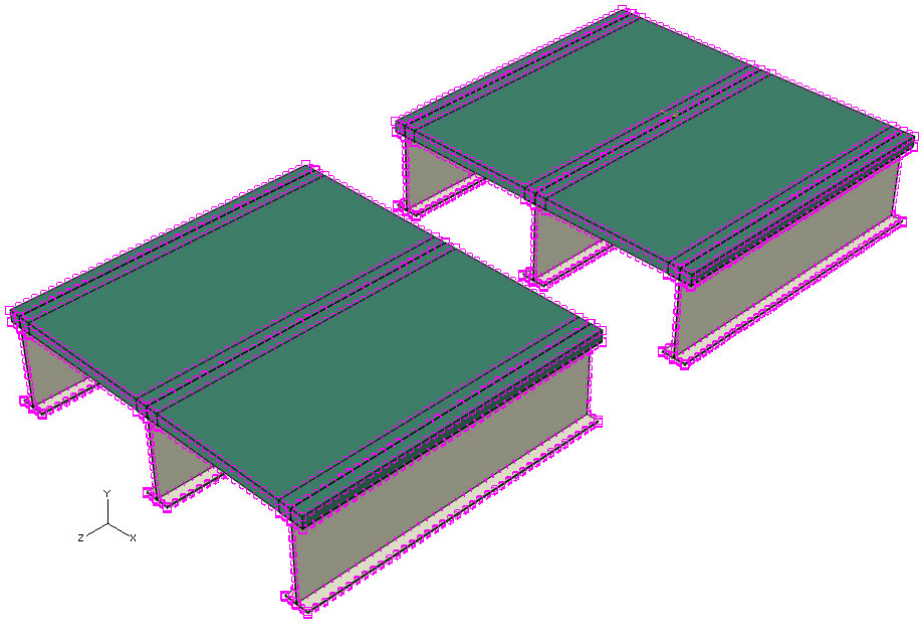

Figure 2-14 Girders and concrete deck - outside seeding

- *Girders and Concrete Deck – Inside Part Instance*: Multiple seed sizes were used in this part instance; a finer mesh was used in the web-gap region because high stresses were anticipated in this area. To achieve a finer mesh in the web-gap region, the following steps were used to seed this part instance. First, as shown in the plan view of this part instance, the outer region (shown in Figure 2-15) used a seed size of 1.0 in./element. Second, as shown in the plan view of this part instance, the inner region (shown in Figure 2-16) used a seed size of 0.1 in./element. After seeding was completed in a plan view, a finer seeding was defined for the web-gap regions. To achieve this, a section view was used to assign a seed size of 0.05 in./element in the web-gap region, as shown in Figure 2-17.

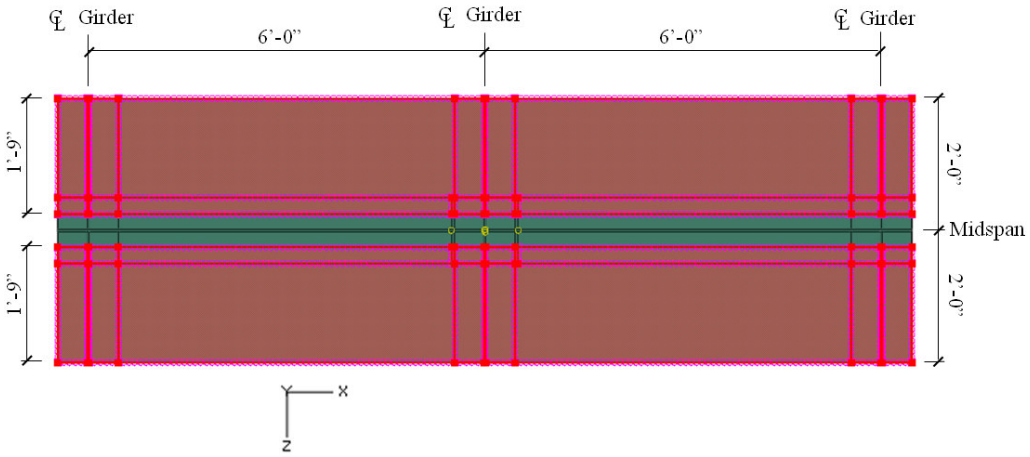

Figure 2-15 Girders and concrete deck - inside: seeding (1.0 in red area)

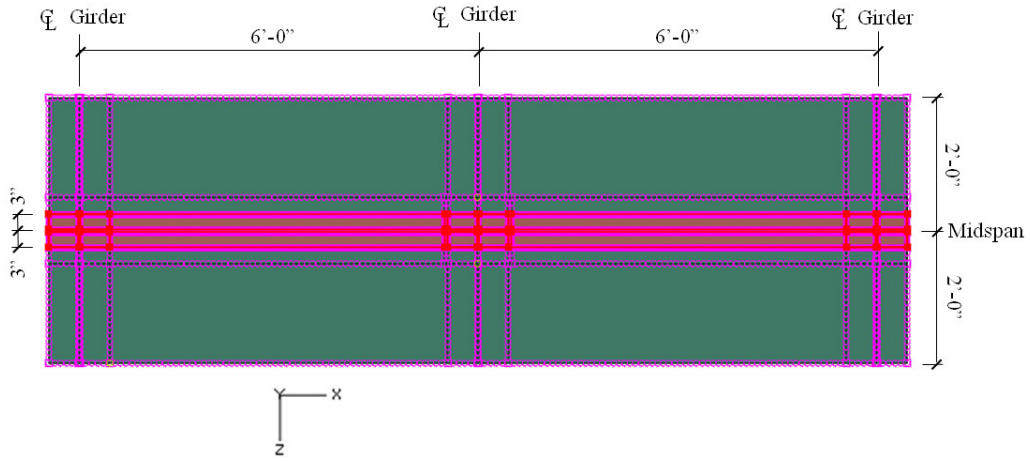

Figure 2-16 Girders and concrete deck - inside: seeding (0.1 in red area)

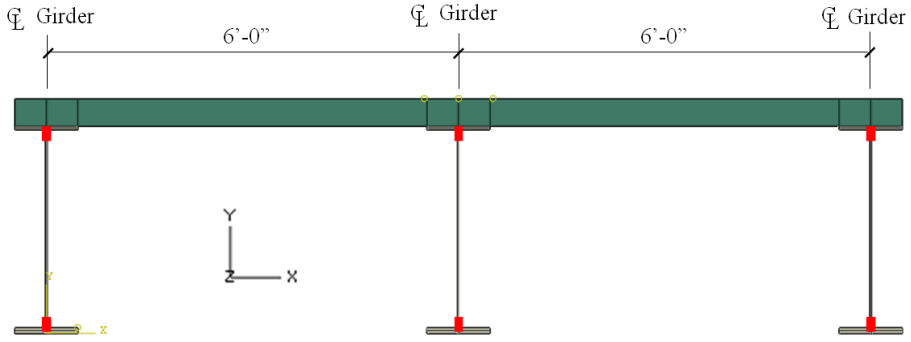

Figure 2-17 Girders and concrete deck - inside: seeding (0.5 in red area)

- *Braces Part Instance*: Similar to the case of the "Girders and Concrete Deck – Inside" part instance, a finer mesh was desired in the region closest to the web-gap. To achieve this, a section view of this part instance was utilized, and the following seeding procedure was used. First, the brace regions not connected to the web connection plate were seeded with 0.5 in./element, as shown in Figure 2-18. After this, the web connection plate and brace regions connected to the plate were seeded with 0.1 in./element, as shown in Figure 2-19.

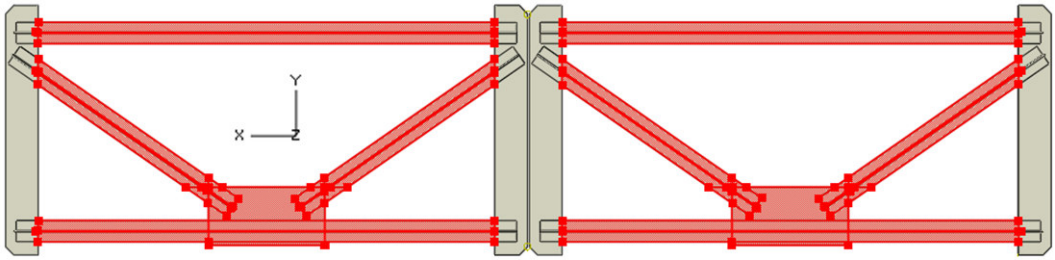

Figure 2-18 Braces part instance: seeding (0.5 in red area)

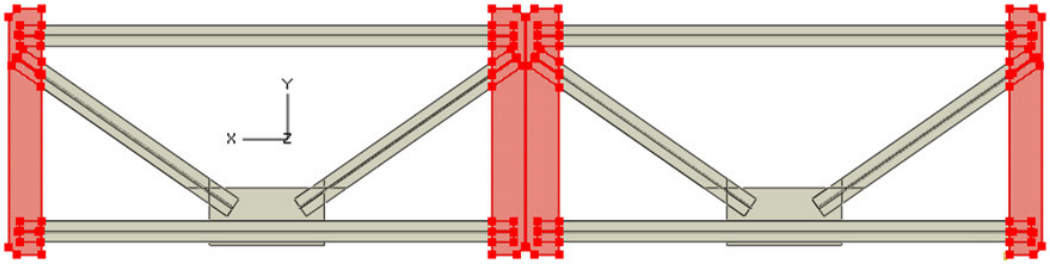

Figure 2-19 Braces part instance: seeding (0.1 in red area)

After seeding was completed on all the part instances, automatic meshing was performed. Structured hex meshes were used in all regions other than the connection plates; swept hex meshes were used in the connection plates due to the

complex geometry. Standard C3D8R (8-node linear brick, reduced integration, hourglass control) elements were used for all parts.

These Finite Element models based on different connection plate configurations and retrofitting schemes were used to study web-gap stresses due to differential deflections of adjacent girders.

CHAPTER 3 – STRESS ANALYSIS PROCEDURES

Fatigue life estimates of welded structures are usually based on a nominal stress distribution away from the point a crack is thought to initiate. The problem with this kind of analysis is that a nominal stress can be extremely difficult to define in complex welded structures (Kim and Kang 2008). Given that high stress gradients occur in the vicinity of welds, combined with the fact that it is very difficult to define a nominal stress in complex welded structures, S-N curves in the American Association of State Highway and Transportation Officials (AASHTO) Code (AASHTO 2002), which are based on nominal stresses, are not a good tool to estimate the number of loading cycles to crack initiation. Because of the aforementioned limitations, alternate analysis methods have been developed (Maddox 2002, Nihei 1997, Dong and Hong 2003) using results from Finite Element (FE) analyses to estimate the number of loading cycles to crack initiation. Two alternate methods, in particular, are called Hot-Spot Stress (HSS) and Structural Stress (SS) analyses.

3.1 WHY USE NEW STRESS ANALYSIS?

The FE models described in Chapter 2 were developed to study the distortion in web-gaps caused by differential deflections of adjacent girders. For the single span system that was analyzed, positive bending would be expected to produce the highest web-gap stresses (Roddis and Zhao 2001). Different mesh

densities in the web-gap were studied to determine the effect of mesh density on web-gap stress. This was important in terms of convergence; it would be ideal for the web-gap stress not to depend on mesh density.

The effect of mesh density on the web-gap stresses was studied using the finite element models of the KU Test Bridge described in Chapter 2. All models used in the convergence study were built using the procedures described in Section 2.3, except for the seeding of the part instance designated "Girders and Concrete Deck – Inside". The only difference between the meshing procedure used in the convergence study and the FE models described in Section 2.3 was that seeding in the web-gap region (shown in Figure 2-17) of the convergence study models ranged from 0.01 to 0.1 in./element. In addition to these nine (9) models, one (1) FE model used a seeding of 0.05 in./element in the web-gap region and 0.05 inches/element on the connection plate shown in Figure 2-19. A total of ten (10) models were analyzed for the convergence study.

The results of the FE study showed that web-gap stress increased as mesh density increased, as shown in Figure 3-2. Because the calculated stress demand diverged, it was difficult to identify with any certainty the magnitude of stresses occurring in the web-gap region.

As discussed before, it is difficult to define the nominal stress range that should be used to calculate the number of loading cycles to crack initiation. Because of this, different forms of stress analysis were performed to obtain a more consistent understanding of the magnitude of web-gap stresses. Using these

alternate forms of analysis was important because different situations may utilize different mesh densities and therefore may produce inconsistent stress values. Alternate analysis procedures are discussed in the following sections.

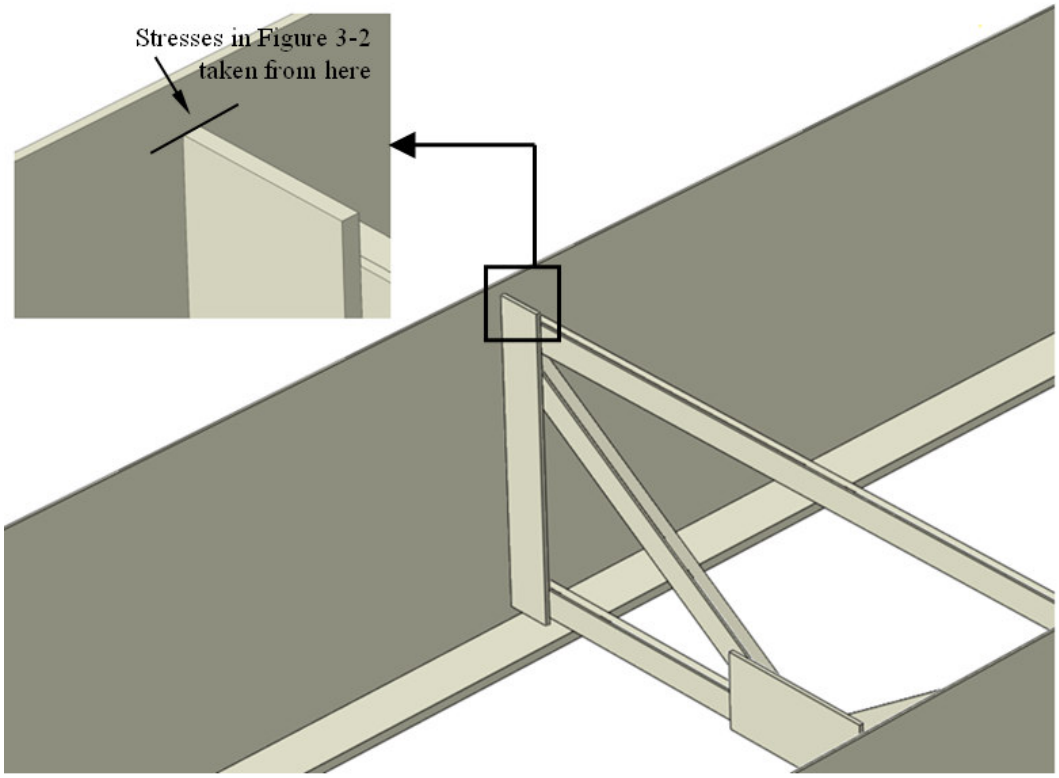

Figure 3-1 3D view of KU test setup (concrete deck and top flanges removed)

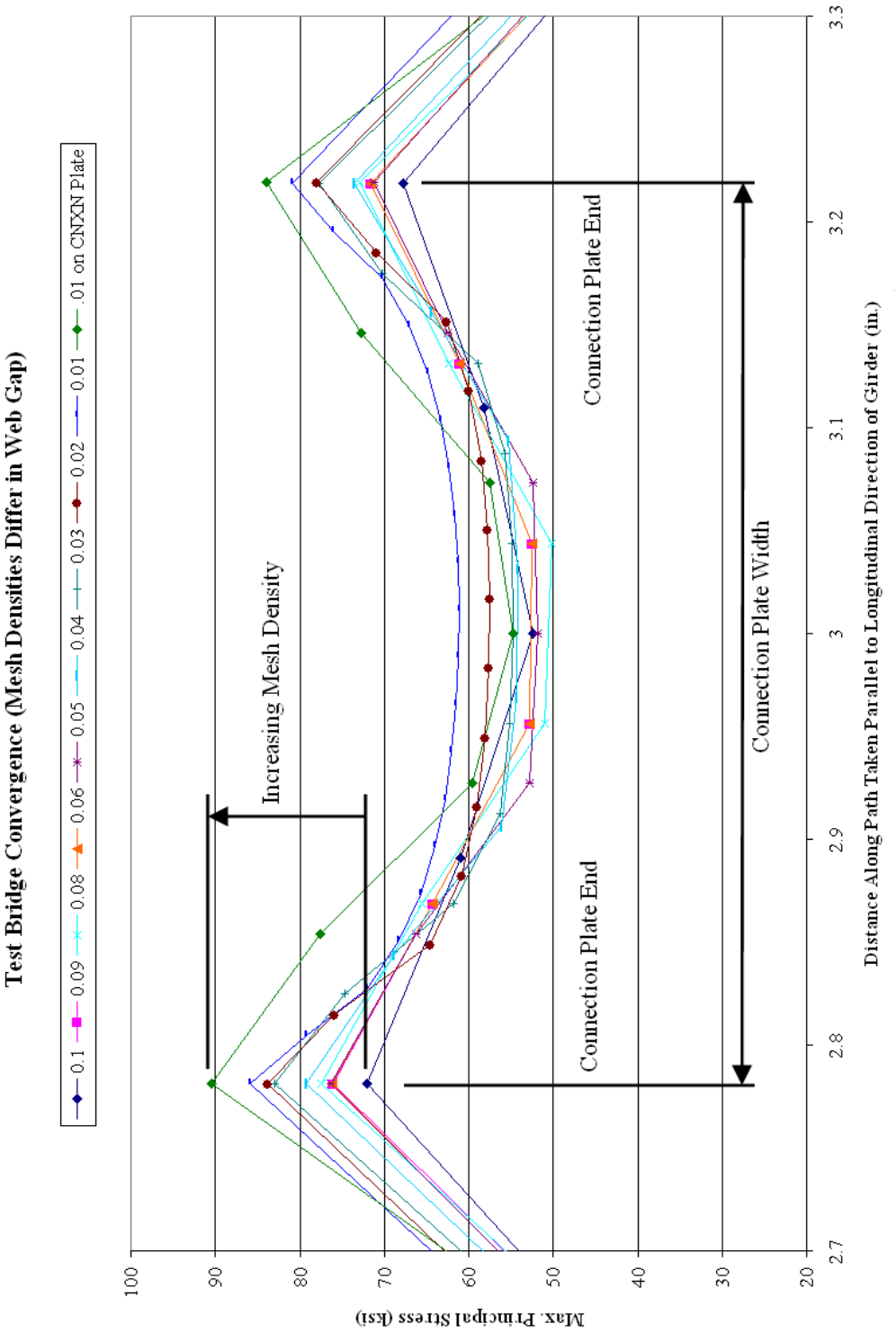

Figure 3-2 Mesh density and principal stresses

3.2 STRESS ANALYSIS METHODS

There are two common procedures for estimating the level of stress demand at the weld toe of a structure. The first is called Hot Spot Stress (HSS) analysis which is defined as the sum of the bending and membrane stresses at a structural discontinuity (Marquis and Kahonen 1996). Membrane stress is defined as the stress resulting from the effect of axial load only (axial load/area). This analysis procedure was first developed for use in the offshore industry where it has been used as an accurate way of performing fatigue assessments of welded structures (Marquis and Kahonen 1996); however, HSS analysis is not limited to only this particular field. HSS analysis was developed because nominal stresses in offshore structures were almost impossible to define. HSS analysis utilizes either a one-point procedure or a two-point extrapolation procedure to estimate the level of stress at the weld toe. The process of HSS analysis starts with reading computed stress levels a predetermined distance away from the weld toe. The locations where the stress levels are read must be far enough away so that the stresses are not influenced by the discontinuity at the weld toe. The distance from the weld toe is calculated based on plate thickness and/or weld length. Niemi (1993) listed several cases where the HSS analysis may be more suitable than the conventional nominal stress analysis:

1. There is no clearly defined nominal stress due to complicated geometric effects.

2. The structural discontinuity is not comparable with any classified details included in design specifications.
3. The finite element method is used.
4. Field testing of a prototype structure is performed using hot spot strain gauge measurements.
5. Offset or angular misalignments exceed the fabrication tolerances, invalidating some of the basic conditions for using the nominal stress approach.

Although stresses are considered at points away from the weld toe, HSS analysis is known to be dependent on mesh element type and extrapolation technique (discussed in Section 3.3); this dependency is not ideal. However, because conditions 1 through 3 above are met (a nominal stress cannot be clearly defined, the structural discontinuity is unique to every detail, and the finite element method is used), the HSS analysis approach is one of the best alternatives for the study of distortion-induced fatigue in transverse stiffener web-gaps.

The second procedure considered for estimating the magnitude of stress at a weld toe is called Structural Stress (SS) analysis, and is also defined as the sum of the bending and membrane stresses at a structural discontinuity. However, this method calculates the bending and membrane stresses independently rather than using extrapolation. This can be done by using both normal and shear stresses at a plane a predetermined distance from the weld toe or by using a set of equations which combine average stresses from two different planes away from the weld

toe. This type of analysis has been known to be mesh insensitive (Poutiainen et al. 2004); meaning that element size and type are not thought to influence the amount of structural stress at the weld toe.

Both the HSS and SS analyses were expected to provide a more consistent estimation of the magnitude of stress at the web-gap and at the weld toe attaching the connection plate to the girder web of the KU Test Bridge model described in Chapter 2. Specific procedures for these methods are further discussed in the following sections.

3.3 HOT SPOT STRESS ANALYSIS

As discussed in the previous section, HSS analysis utilizes either a one-point procedure or a two-point extrapolation procedure to estimate the magnitude of stress in the vicinity of the weld toe.

3.3.1 TWO-POINT EXTRAPOLATION PROCEDURE

There are several different two-point extrapolation procedures that can be used to estimate the level of hot spot stress demand at a weld toe of a connection. Both two-point procedures described below are based on stress values calculated from a predetermined distance from the weld toe; this distance is a function of the plate thickness (in this case, girder web thickness). With regards to the FE models created for the KU Test Bridge described in Chapter 2, a path was defined

through the top edge of the connection plate along the web face (parallel to longitudinal direction of girder web), as shown in Figure 3-1. The two extrapolation procedures can be completed as follows, based on the stress profile along the previously defined path:

- *0.4t/1.0t (Recommended by the International Institute of Welding (IIW)) (Maddox 2002).* This procedure requires that stresses be read from distances of 0.4(t) and 1.0(t) away from the weld toe where t is the plate thickness. A straight line is then drawn through these points and continued until the line reaches the location of the weld toe. The corresponding HSS value is determined where the straight line intersects the weld toe.
- *0.5t/1.5t (Maddox 2002).* This extrapolation procedure is very similar to the previous 0.4t/1.0t method. However, new distances of 0.5(t) and 1.5(t) are used where t is the plate thickness. Again, the HSS is determined by drawing a straight line through these two points and calculated where this line crosses the point of interest on the weld toe.

Both of these procedures are illustrated in Figure 3-3. In general, the 0.5t/1.5t procedure yields lower HSS values than the 0.4t/1.0t procedure.

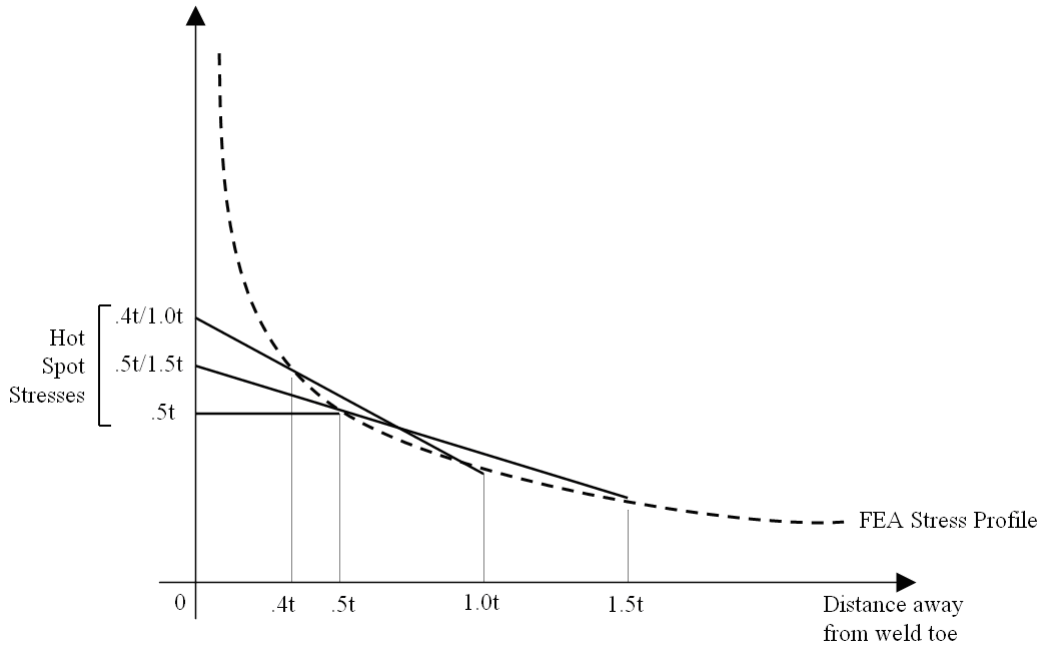

Figure 3-3 Hot spot stress procedure – 0.4t/1.0t, 0.5t/1.5t, and 0.5t techniques

Fatigue research based on HSS analysis has produced various versions of S-N curves that make no distinction in terms of which fatigue category a connection belongs to. This type of S-N curve is not dependent on geometry of the connection as the AASHTO S-N curves are. Marquis and Kahonen (1996) cited that the International Institute of Welding (IIW) has generated an S-N curve based on this kind of analysis (Figure 3-4). Although this is the curve based on the recommended HSS procedure (0.4t/1.0t), other HSS S-N curves have been generated and can be found in Marquis and Kahonen (1996).

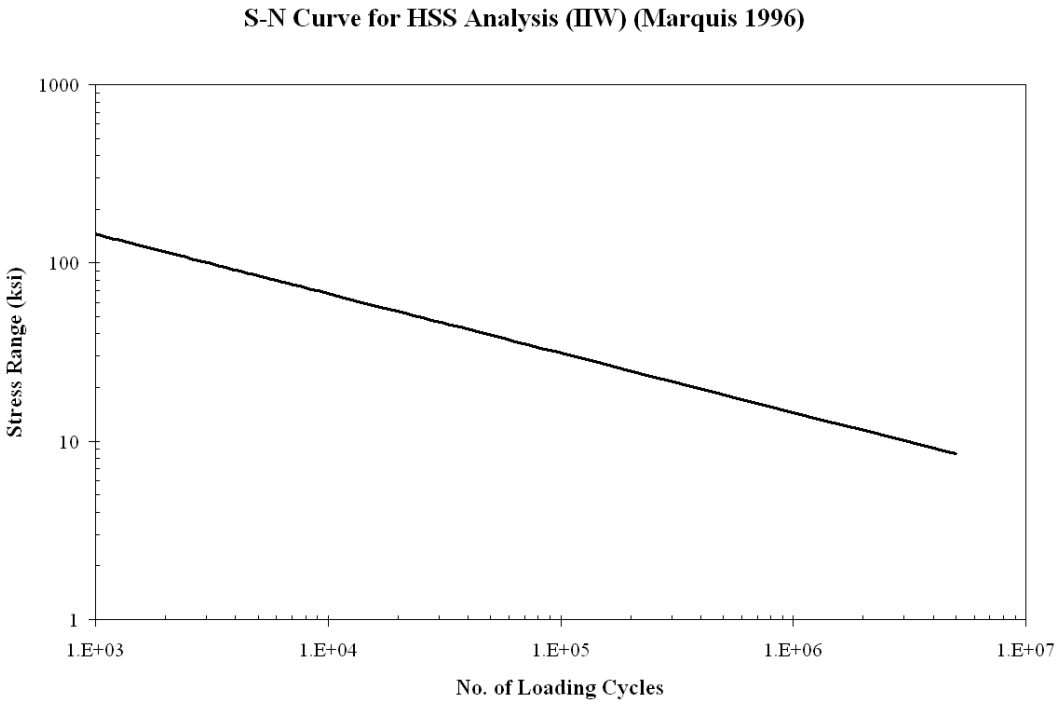

Figure 3-4 S-N curve for HSS analysis (Marquis and Kahonen 1996)

The above S-N curve is valid for a maximum of 5 million cycles. After this, Marquis and Kahonen (1996) state this curve can no longer be used but do not designate whether this number of loading cycles corresponds to "infinite" fatigue life.

3.3.2 ONE-POINT ANALYSIS PROCEDURE

Instead of using a two-point extrapolation procedure as discussed in the previous section, HSS values may alternately be read from a single point at a pre-defined distance away from the weld toe. This distance is either a function of thickness alone or thickness and weld length.

- *0.5t (Maddox 2002).* The calculated HSS value using this method is read from a point at a distance of 0.5(t) away from the weld toe, where t is the plate thickness, as shown in Figure 3-3.
- *Nihei HSS Method (Nihei 1997).* This single point analysis method involves reading a stress value a predetermined distance from the weld toe. The distance from the weld toe is defined by Eqn 3.1 and is a function of the weld length l and the plate thickness t. According to Eqn 3.1, the distance from the weld toe is calculated by multiplying X_{hss}/t by the plate thickness t. The parameters a, b, and c in Eqn 3.1 are a function of the connection geometry and are defined in Figure 3-5.

$$\frac{x_{hss}}{t} = f\left(\frac{l}{t}\right) = \frac{c \cdot a \cdot \left(\frac{l}{t}\right) + b \cdot \left(\frac{l}{t}\right)^2}{a + \left(\frac{l}{t}\right)^2} \qquad \textbf{Eqn 3.1}$$

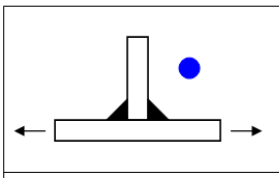	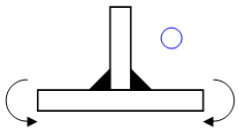	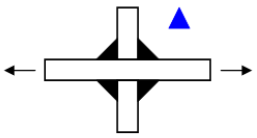	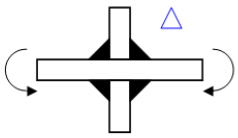
a = 0.03	a = 0.06	a = 0.05	a = 0.01
b = 0.25	b = 0.19	b = 0.23	b = 0.19
c = 1.40	c = 1.50	c = 2.00	c = 1.30

Figure 3-5 Nihei (1997) hot spot stress constants

Figure 3-6 presents the results of Eqn 3.1 graphically. The symbols used for each line correspond to the connection geometries shown in Figure 3-5. As shown in Figure 3-6, as the l/t ratio increased, all of the functions reached an

asymptotic value; Figure 3-6 also shows that small *l/t* ratios can produce very different X_{hss}/t values. The Nihei (1997) HSS value should be read at a distance of X_{hss}/t * plate thickness away from the weld toe.

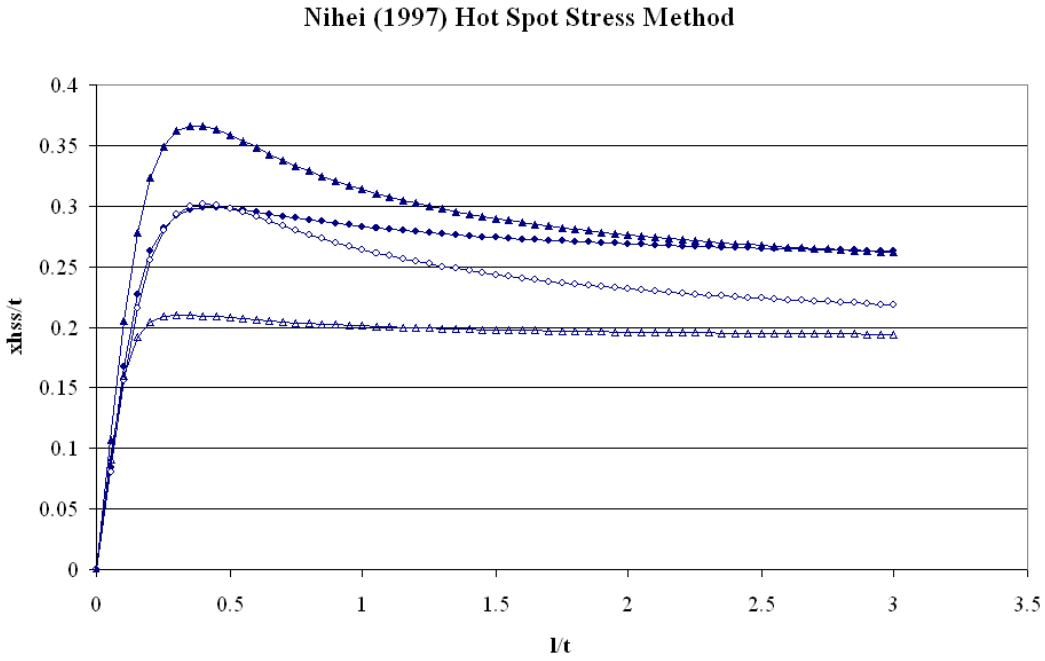

Figure 3-6 Nihei (1997) hot spot stress graph (legend provided in Fig. 3.5)

3.4 STRUCTURAL STRESS ANALYSIS

There were two primary procedures available with which to calculate the magnitude of structural stress at a weld toe found in the literature (Dong and Hong 2003). These two procedures utilize either one or two planes through the thickness of the plate at a predetermined distance away from the weld toe.

3.4.1 ONE-PLANE ANALYSIS PROCEDURE (DONG AND HONG 2003)

The one-plane procedure utilizes stress gradients through the thickness of a plate to calculate a structural stress at a particular location. This plane should be normal to the expected structural stress direction and should pass through a point away from the weld toe. Structural Stress values are calculated using both a force and moment balance to calculate membrane (σ_m) and bending (σ_b) stresses through a plane at the weld toe; equations for these force and moment balances are shown in Eqn 3.2, 3.3, and 3.4 along with a sketch illustrating the procedure in Figure 3-7.

$$\sigma_s = \sigma_m + \sigma_b \qquad \textbf{Eqn 3.2}$$

$$\sigma_m = \frac{1}{t}\int_0^t \sigma_x(y)\,dy \qquad \textbf{Eqn 3.3}$$

$$\sigma_m \frac{t^2}{2} + \sigma_b \frac{t^2}{6} = \int_0^t \sigma_x(y)\cdot y\,dy + \delta\int_0^t \tau_{xy}(y)\,dy \qquad \textbf{Eqn 3.4}$$

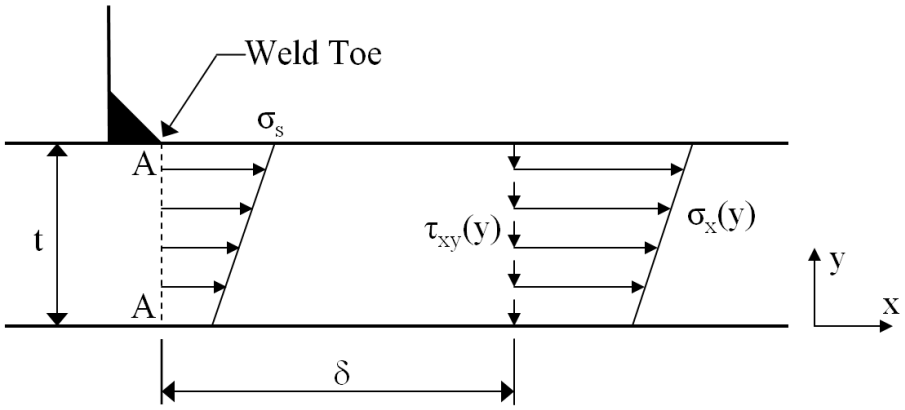

Figure 3-7 One-plane structural stress method

As shown above, the force and moment balance equations are calculated at plane A-A. The moment balance equation is taken about a point with y = 0.

3.4.2 TWO-PLANE ANALYSIS PROCEDURE (DONG AND HONG 2003)

This simpler, two-plane structural stress procedure can only be used when the stress distribution between the two planes is approximately linear near the weld toe. It was observed that the stress distributions near the weld toe of the plate-girder connection calculated with the FE models were, in fact, linear throughout the thickness of the web. As shown in Eqns 3.5 through 3.8 and Figure 3-8, bending stresses are calculated at both planes B-B and C-C by taking half of the difference between the stresses at the top and bottom of the plate. These bending stresses are used to extrapolate the magnitude of the structural stress at plane A-A through the weld toe.

$$\sigma_b^B = \frac{1}{2}\left(\sigma_{Top}^B - \sigma_{Bot}^B\right) \qquad \textbf{Eqn 3.5}$$

$$\sigma_b^C = \frac{1}{2}\left(\sigma_{Top}^C - \sigma_{Bot}^C\right) \qquad \textbf{Eqn 3.6}$$

$$\sigma_b^A = \sigma_b^B + \frac{L}{\delta}\left(\sigma_b^C - \sigma_b^B\right) \qquad \textbf{Eqn 3.7}$$

$$\sigma_s = \sigma_{Top}^B + \frac{L}{\delta}\left(\sigma_b^C - \sigma_b^B\right) \qquad \textbf{Eqn 3.8}$$

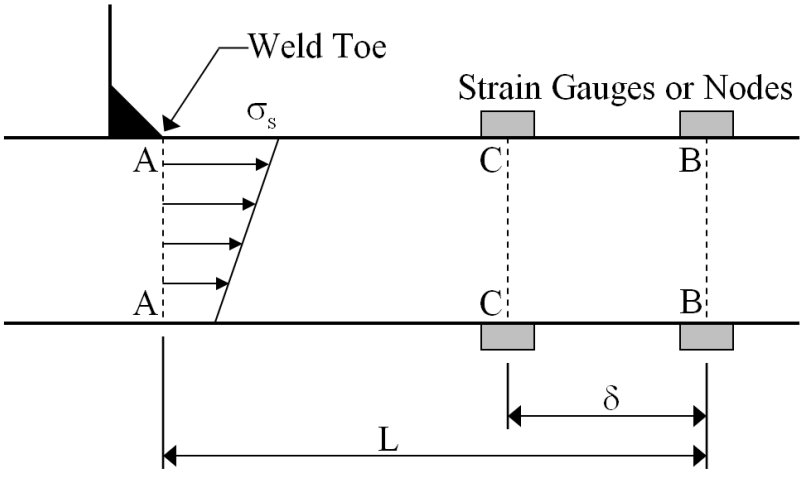

Figure 3-8 Two-plane structural stress method

3.5 STRESS ANALYSIS PROCEDURE ADOPTED IN THE STUDY

Finite Element (FE) models were created to study the effect of mesh density in the web-gap region on the magnitude of the stresses around the weld toe of the connection plate. As shown in Figure 3-2, the magnitude of principal stresses differed by as much as 20 ksi for the range of mesh densities that were analyzed. Because of this discrepancy, the use of stress analysis procedures was investigated to determine if a more consistent and accurate measure of stress at the weld toe of the structure could be obtained. The manner in which the stress analysis methods were implemented is discussed below.

- *0.4t/1.0t HSS Method* – Because the thickness of the girder web was 0.25 in., stress values were read at 0.1 in. and 0.25 in. away from the weld toe, and the HSS value at the weld toe was extrapolated based on these two points.
- *0.5/1.5t HSS Method* – Because the web thickness was 0.25 in., stress values were obtained at distances of 0.125 in. and 0.375 in. away from the weld toe. Extrapolation was used to find the HSS value at the discontinuity.
- *0.5t HSS Method* – The HSS value was read at a distance of 0.125 in. away from the weld toe.
- *Nihei HSS Method* – Because the connection plate configuration was a combination of both of the T-shaped joints shown in Figure 3-5 and Figure

3-6 (the girder web was under neither pure axial load nor pure bending), an X_{hss}/t value corresponding to a l/t ratio of 1.75 was used. Using this X_{hss}/t value, the HSS was read at a distance of 0.0625 in. away from the weld toe.

- *One-Plane SS Procedure* – This procedure was only performed twice on one particular mesh density model. Two different planes were studied to determine if a similar SS value was obtained from both planes (Figure 3-9). Discussion as to why this analysis was only performed twice is described in Section 3.6.5.
- *Two-Plane SS Procedure* – Structural stresses were calculated for each mesh density based on stresses calculated at planes through the two nodes closest to the weld toe (Figure 3-10). In addition, structural stresses were calculated based on a different set of planes to determine if a similar SS value could be obtained using different sets of planes that were also close to the weld toe (Figure 3-11).

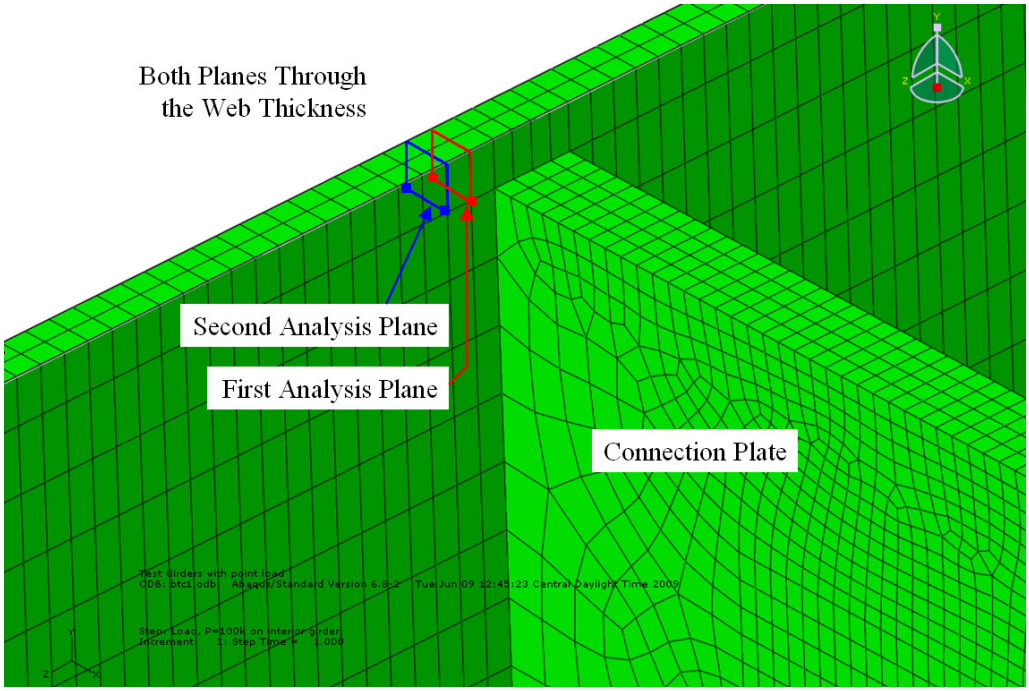

Figure 3-9 One-plane SS analysis planes (same angle as Figure 3-1)

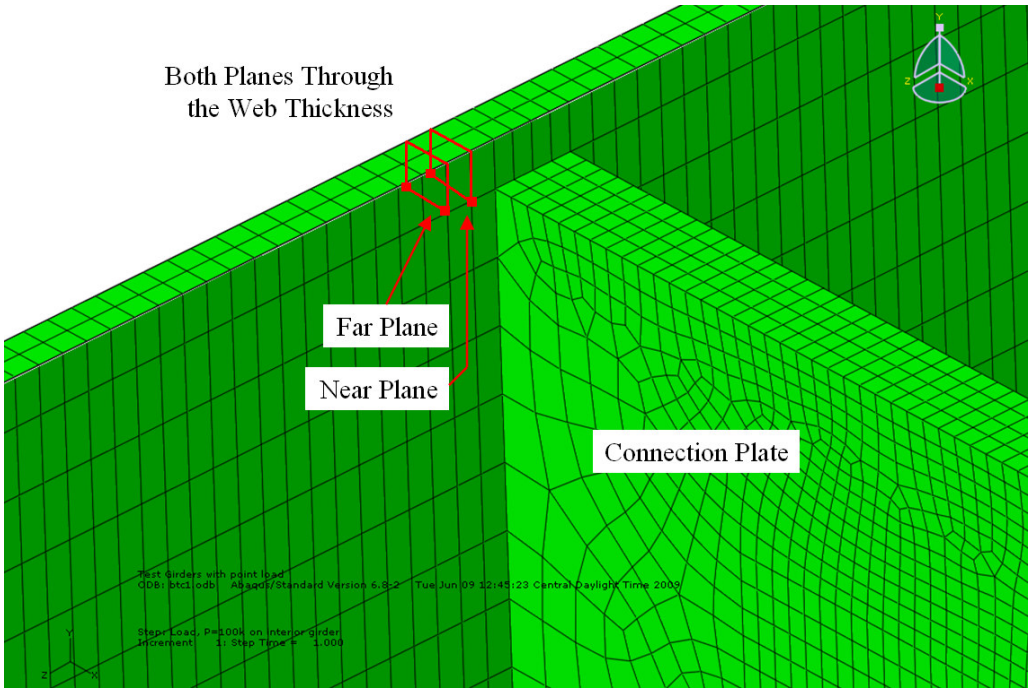

Figure 3-10 Two-plane SS analysis planes. First calculation (same angle as Figure 3-1)

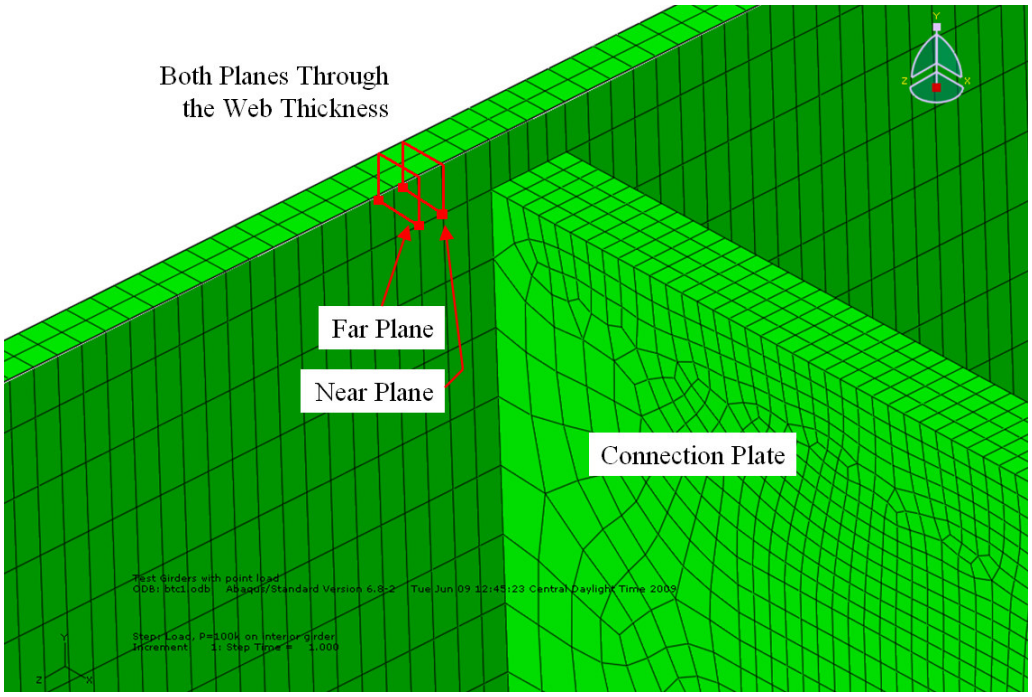

Figure 3-11 Two-plane SS analysis planes. Second calculation (same angle as Figure 3-1)

3.6 RESULTS

Results of the different stress analysis procedures along with the maximum stress values from the FE models are presented and discussed in this section. The different stress analysis procedures were applied to the Maximum Principal, S_{11}, S_{22}, and S_{33} stress distributions in the region where the connection plate intersects the girder web as shown in Figure 3-1.

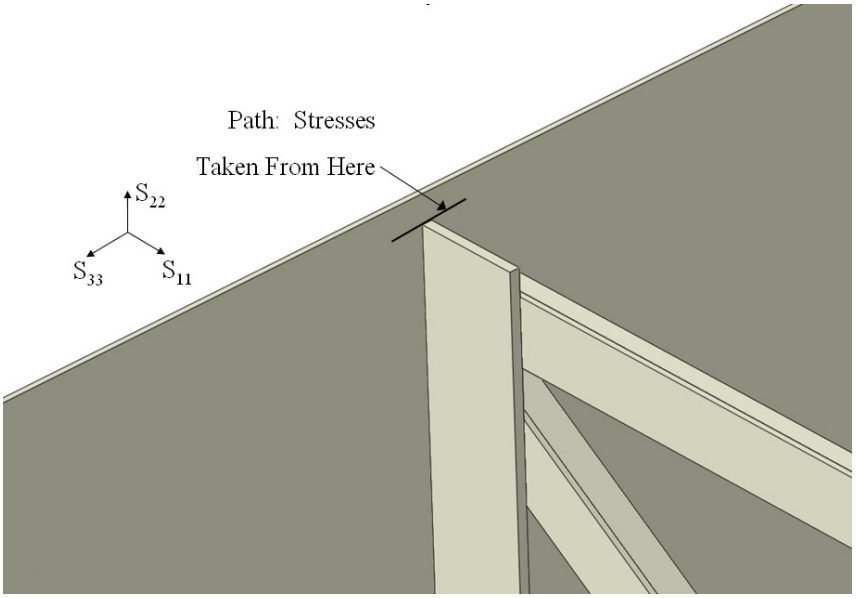

Figure 3-12 Stress directions for analysis (same angle as Figure 3-1)

Results of the convergence study using different stress analysis procedures are summarized in Tables 3-1 through 3-9. The mesh densities listed on the left side of the table are in units of *in./element*, meaning that a smaller mesh number is indicative of a finer mesh. It is important to note that there were significant fluctuations in the magnitude of the calculated stresses depending on the mesh density and the type of stress analysis procedure. The Two-Plane Structural Stress procedure was based on stress values at two planes through the two nodes closest to the connection plate as shown in Figure 3-10. A second calculation using two different planes (shown in Figure 3-11) will be discussed in Section 3.6.6 to illustrate inconsistencies that were found while using this method. Also, the One-Plane Structural Stress procedure is not presented in the tables; results

were omitted because the calculations yielded inconsistent values depending on which nodes the plane was drawn through.

3.6.1 MAXIMUM PRINCIPAL STRESS RESULTS

The main disadvantage of adopting the maximum principal stress as a stress indicator is the inability to estimate correctly the direction at which a crack will propagate. As shown in Table 3-1, there was a variation of 18.5 ksi in the calculated maximum principal stress within the range of mesh densities of the study. Although this table shows a finite number of different models, there is no limit to the number of possible mesh densities, and consequently it is possible that the stress level would likely diverge even more with different mesh sizes. To overcome this problem, the following stress analysis procedures were used and the results were as follows:

Table 3-1 Maximum Principal Stress - Convergence Study Stress Values

MAXIMUM PRINCIPAL STRESSES (ksi)

Mesh (in./element)	FEA Max	0.4t/1.0t	0.5t/1.5t	0.5t	Nihei	Structural Stress (2-Plane)
0.1	72.0	62.3	54.3	44.4	58.2	38.8
0.09	76.1	64.0	55.0	44.9	60.4	38.8
0.08	77.4	63.8	53.8	43.7	60.5	39.5
0.06	76.2	65.3	56.5	45.8	61.0	38.3
0.05	76.4	65.0	56.4	45.9	61.0	38.2
0.04	79.2	67.1	58.3	47.0	63.0	39.0
0.03	83.0	70.6	60.9	49.0	65.8	38.5
0.02	83.9	73.9	64.6	51.5	67.4	39.0
0.01	85.9	76.0	66.3	52.8	69.2	39.8
0.01-plate	90.5	72.3	60.0	47.6	69.0	37.8
Average	80.1	68.0	58.6	47.3	63.6	38.8

Table 3-2 Maximum Principal Stress - Convergence Study % Difference

MAXIMUM PRINCIPAL STRESSES (% difference from FEA Max)

Mesh (in./element)	0.4t/1.0t	0.5t/1.5t	0.5t	Nihei	Structural Stress (2-Plane)
0.1	-13.5	-24.6	-38.3	-19.2	-46.1
0.09	-15.9	-27.7	-41.0	-20.6	-49.0
0.08	-17.6	-30.5	-43.5	-21.8	-49.0
0.06	-14.3	-25.9	-39.9	-19.9	-49.7
0.05	-14.9	-26.2	-39.9	-20.2	-50.0
0.04	-15.3	-26.4	-40.7	-20.5	-50.8
0.03	-14.9	-26.6	-41.0	-20.7	-53.6
0.02	-11.9	-23.0	-38.6	-19.7	-53.5
0.01	-11.5	-22.8	-38.5	-19.4	-53.7
0.01-plate	-20.1	-33.7	-47.4	-23.8	-58.2
Average	-15.0	-26.7	-40.9	-20.6	-51.4

- *0.4t/1.0t HSS Method* – Using this extrapolation method, the maximum principal hot spot stress ranged between 62.3 and 76.0 ksi. These HSS values averaged 15.0% lower than the maximum principal stress values calculated directly at the weld toe from the models. The HSS had a standard deviation of 4.80 ksi which was lower than the FE maximum principal stress calculated at the weld toe standard deviation of 5.61 ksi.
- *0.5t/1.5t HSS Method* – Values obtained when using this method were lower than the absolute maximum principal stress values calculated directly at the weld toe using the FE models by 26.7%. The range of HSS values using this method was 53.8 to 66.3 ksi. The HSS had a standard deviation of 4.30 ksi which was lower than the maximum principal stress calculated at the weld toe standard deviation of 5.61 ksi.

- *0.5t HSS Method* – This one point extrapolation procedure produced HSS values within the range of 43.7 to 52.8 ksi. These HSS values averaged 40.9% lower than the FEA maximum principal stress values calculated directly at the weld toe. The HSS standard deviation was 3.02 ksi which was lower than the FEA maximum principal stress value calculated at the weld toe standard deviation of 5.61 ksi.
- *Nihei HSS Method* – Using this one point extrapolation method based on the plate thickness and weld length produced HSS values in the range of 58.2 to 69.2 ksi. The HSS values averaged 20.6% lower than the FEA maximum principal stress values calculated directly at the weld toe. The HSS had a standard deviation of 3.98 ksi which was lower than the FEA maximum principal stress calculated at the weld toe standard deviation of 5.61 ksi.
- *Two-Plane Structural Stress Method* – Using two planes through the two nodes closest to the weld toe produced very consistent results. The range of SS values was 37.8 to 39.5 ksi and averaged 51.4% lower than the FEA maximum values calculated directly at the weld toe. However, the same range of values was not achieved when using two different planes as discussed with greater detail in Section 3.6.6.

3.6.2 S_{11} STRESS RESULTS

The S_{11} stress results (Tables 3-3 and 3-4) were examined because a crack would likely initiate and propagate in a direction perpendicular to these stresses (the 1-1 direction is shown in Figure 3-12). The range of maximum stress values calculated with the FE models in the 1-1 direction was found to be 16.8 ksi, and the stress magnitudes were obviously lower than the principal stress values obtained from the FE models (shown in

Table 3-3). The results of the stress analysis procedures are discussed below:

Table 3-3 S_{11} - Convergence Study Stress Values

S_{11} (ksi)

Mesh (in/element)	FEA Max	0.4t/1.0t	0.5t/1.5t	0.5t	Nihei	Structural Stress (2-Plane)
0.1	55.0	26.9	9.80	6.50	31.0	-0.96
0.09	58.8	29.0	10.5	7.00	33.0	-1.01
0.08	59.8	29.1	11.1	7.50	33.5	-0.41
0.06	58.9	32.3	13.9	9.30	34.0	-0.96
0.05	60.0	33.0	14.3	9.50	35.0	-0.92
0.04	62.8	34.2	15.5	10.5	36.5	-0.19
0.03	67.1	41.5	20.9	14.0	40.5	-0.21
0.02	68.7	45.7	25.3	16.5	42.5	-1.23
0.01	71.3	47.2	27.0	18.0	44.5	-0.28
0.01-plate	71.8	39.6	17.3	11.5	42.0	-0.43
Average	63.4	35.9	16.6	11.0	37.3	-0.70

Table 3-4 S_{11} - Convergence Study % Difference

S_{11} (% difference from FEA Max)

Mesh (in/element)	0.4t/1.0t	0.5t/1.5t	0.5t	Nihei	Structural Stress (2-Plane)
0.1	-51.1	-82.3	-88.2	-43.6	-101.7
0.09	-50.7	-82.1	-88.1	-43.9	-101.7
0.08	-51.3	-81.4	-87.5	-44.0	-100.7
0.06	-45.2	-76.4	-84.2	-42.3	-101.6
0.05	-45.0	-76.2	-84.2	-41.7	-101.5
0.04	-45.5	-75.3	-83.3	-41.9	-100.3
0.03	-38.2	-68.9	-79.1	-39.6	-100.3
0.02	-33.5	-63.2	-76.0	-38.1	-101.8
0.01	-33.8	-62.1	-74.8	-37.6	-100.4
0.01-plate	-44.8	-75.9	-84.0	-41.5	-100.6
Average	-43.9	-74.4	-82.9	-41.4	-101.1

- *0.4t/1.0t HSS Method* – The HSS values ranged from 26.9 to 47.2 ksi. These values averaged 43.9% lower than the FEA maximum S_{11} values calculated directly at the weld toe. The HSS standard deviation was 7.21 ksi which was higher than the FEA S_{11} stress calculated at the weld toe standard deviation of 5.88 ksi. However, the range of stress values for this extrapolation method was higher than the FEA S_{11} maximum stress range.
- *0.5t/1.5t HSS Method* – These HSS values averaged 74.4% lower than the FEA maximum S_{11} stress values calculated directly at the weld toe. The HSS had a standard deviation of 6.06 ksi which was higher than the FEA maximum S_{11} stress calculated at the weld toe standard deviation of 5.88 ksi. The HSS values ranged from 9.8 to 27.0 ksi; the magnitude of this range was very similar to the range of the maximum S_{11} values found from the FE models which were calculated at the weld toe.

- *0.5t HSS Method* – This one point extrapolation procedure yielded HSS values ranging between 6.5 and 18.0 ksi which averaged 82.9% lower than the FEA maximum S_{11} stress values calculated directly at the weld toe. The standard deviation of HSS values was 3.98 ksi which was lower than the standard deviation of FEA S_{11} values at 5.88 ksi.
- *Nihei HSS Method* – The HSS values determined using this one point extrapolation procedure averaged 41.4% lower than the FEA maximum S_{11} values calculated directly at the weld toe. The standard deviation for this method was 4.72 ksi which is lower than standard deviation of FEA S_{11} values calculated at the weld toe of 5.88 ksi.
- *Two-Plane Structural Stress Method* – Two planes were used through the two nodes closest to the weld toe and the calculated forces were in compression, which were not consistent the finite element and HSS results. The average SS value was 101.1% lower than the maximum FEA S_{11} values. The SS had a standard deviation of 0.391 ksi which was lower than the FEA maximum S_{11} stress calculate at the weld toe standard deviation of 5.88 ksi.

3.6.3 S_{22} STRESS RESULTS

The S_{22} stress results were examined because a crack might initiate and propagate perpendicular to this direction (the 2-2 direction is shown in Figure 3-12). The range of maximum S_{22} stresses from the FE models was found to be 14.1 ksi (Table 3-5), and the maximum S_{22} values were significantly lower than the maximum principal stresses obtained from the FE models calculated directly at the weld toe (Tables 3-5 and 3-6). The results of the stress analysis procedures are discussed below:

Table 3-5 S_{22} - Convergence Study Stress Results

S_{22} (ksi)

Mesh (in/element)	FEA Max	0.4t/1.0t	0.5t/1.5t	0.5t	Nihei	Structural Stress (2-Plane)
0.1	52.3	52.0	58.1	47.1	49.6	69.9
0.09	52.6	52.6	58.4	47.1	49.9	69.3
0.08	50.1	50.1	52.8	43.8	47.0	66.6
0.06	52.7	52.7	58.6	47.1	49.9	69.4
0.05	52.8	52.8	58.5	47.1	50.0	68.0
0.04	55.2	57.9	64.0	50.3	52.7	71.1
0.03	56.6	58.5	64.6	50.5	53.5	70.8
0.02	60.2	71.0	75.3	56.7	58.4	74.4
0.01	64.2	81.7	77.0	57.3	65.0	78.9
0.01-plate	55.3	57.3	62.5	48.8	52.0	67.2
Average	55.2	58.7	63.0	49.6	52.8	70.6

Table 3-6 S_{22} - Convergence Study % Difference

S_{22} (% difference from FEA Max)

Mesh (in/element)	0.4t/1.0t	0.5t/1.5t	0.5t	Nihei	Structural Stress (2-Plane)
0.1	-0.57	11.1	-9.94	-5.16	33.7
0.09	0.00	11.0	-10.5	-5.13	31.7
0.08	0.00	5.39	-12.6	-6.19	32.9
0.06	0.00	11.2	-10.6	-5.31	31.7
0.05	0.00	10.8	-10.8	-5.30	28.8
0.04	4.89	15.9	-8.88	-4.53	28.8
0.03	3.36	14.1	-10.8	-5.48	25.1
0.02	17.9	25.1	-5.81	-2.99	23.6
0.01	27.3	19.9	-10.7	1.25	22.9
0.01-plate	3.62	13.0	-11.8	-5.97	21.5
Average	5.65	13.8	-10.2	-4.48	28.1

- *0.4t/1.0t HSS Method* – The HSS values were very consistent until a relatively fine mesh was used (mesh seed size = 0.01 in./element) where the HSS value jumped to 81.7 ksi, while the low stress value was 50.1 ksi. For larger mesh densities (mesh seed size = 0.1 to 0.03 in./element), the HSS values compared very similarly to the FEA S_{22} values calculated directly at the weld toe. The average HSS value was 5.6% higher than the maximum FEA S_{22} values. The HSS had a standard deviation of 10.1 ksi which was higher than the FEA maximum S_{22} stress calculated at the weld toe standard deviation of 4.23 ksi.
- *0.5t/1.5t HSS Method* – It was interesting to see that the HSS values for this procedure were generally higher than the 0.4t/1.0t extrapolation method. The average HSS value was 13.8% higher than the FEA maximum S_{22} values calculated directly at the weld toe. The HSS had a

standard deviation of 7.75 ksi which was higher than the FEA maximum S_{22} stress calculated at the weld toe standard deviation of 4.23 ksi.

- *0.5t HSS Method* – This method produced very consistent results across the range of mesh densities (except for a low value of 43.8 ksi at a mesh density of 0.08 in./element). The average HSS value was 10.2% lower than the FEA maximum S_{22} values calculated directly at the weld toe. The HSS had a standard deviation of 4.35 ksi which was higher than the FEA maximum S_{22} stress calculated at the weld toe standard deviation of 4.23 ksi.
- *Nihei HSS Method* – Using this one point HSS method also produced very consistent results (except for a high outlier of 65.0 ksi at a mesh density of 0.01 in./element). The average HSS value was 4.5% lower than the FEA maximum S_{22} values calculated directly at the weld toe. The HSS had a standard deviation of 5.27 ksi which was higher than the FEA maximum S_{22} stress calculated at the weld toe standard deviation of 4.23 ksi.
- *Two-Plane Structural Stress Method* – Very consistent values were obtained using the planes through the two nodes closest to the weld toe, the average SS value was 28.1% higher than the FEA maximum S_{22} value calculated directly at the weld toe with a standard deviation of 3.67 ksi. Again, different results tended to occur when using different planes, as discussed in Section 3.6.6.

3.6.4 S_{33} STRESS RESULTS

As discussed in the Sections 3.6.2 and 3.6.3 (describing results for S_{11} and S_{22} stresses), stresses in the S_{33} direction were studied because a crack may initiate and propagate normal to this direction (the 3-3 direction is shown in Figure 3-12). The magnitude of maximum S_{33} stress values from the FE models calculated directly at the weld toe was fairly consistent ranging from 37.1 to 42.4 ksi. Many of the stress analysis methods yielded results that were very close to this range, as discussed below:

Table 3-7 S_{33} - Convergence Study Stress Results

S_{33} (ksi)

Mesh (in/element)	FEA Max	0.4t/1.0t	0.5t/1.5t	0.5t	Nihei	Structural Stress (2-Plane)
0.1	37.1	38.9	38.9	30.1	33.6	39.5
0.09	37.5	39.5	39.3	30.2	33.9	39.6
0.08	36.5	38.3	38.2	29.6	33.0	38.8
0.06	37.3	39	38.8	30.1	33.6	39.3
0.05	37.4	38.8	38.7	30.1	33.8	39.1
0.04	38.7	39.8	39.8	30.9	34.8	39.9
0.03	39.1	39.8	39.8	30.8	34.9	39.7
0.02	40.2	40.8	40.5	31.4	35.8	39.9
0.01	42.4	42.7	42.5	32.7	37.6	41.1
0.01-plate	37.8	39	38.3	29.8	33.8	38.6
Average	38.4	39.7	39.5	30.6	34.5	39.6

Table 3-8 S_{33} - Convergence Study % Difference

S_{33} (% difference from FEA Max)

Mesh (in/element)	0.4t/1.0t	0.5t/1.5t	0.5t	Nihei	Structural Stress (2-Plane)
0.1	4.85	4.85	-18.9	-9.43	6.47
0.09	5.33	4.80	-19.5	-9.60	5.60
0.08	4.93	4.66	-18.9	-9.59	6.30
0.06	4.56	4.02	-19.3	-9.92	5.36
0.05	3.74	3.48	-19.5	-9.63	4.55
0.04	2.84	2.84	-20.2	-10.1	3.10
0.03	1.79	1.79	-21.2	-10.7	1.53
0.02	1.49	0.75	-21.9	-10.9	-0.75
0.01	0.71	0.24	-22.9	-11.3	-3.07
0.01-plate	3.17	1.32	-21.2	-10.6	2.12
Average	3.34	2.87	-20.3	-10.2	3.12

- *0.4t/1.0t HSS Method* – Most of the HSS values calculated using this method compared were very close to the FE analysis results calculated directly at the weld toe. The average HSS value was 3.34% higher than the FEA maximum S_{33} values. The HSS had a standard deviation of 1.28 ksi which was lower than the FEA maximum S_{33} stress calculated at the weld toe standard deviation of 1.78 ksi.
- *0.5t/1.5t HSS Method* – The average HSS value using this method was 2.87% higher than the FEA maximum S_{33} values calculated directly at the weld toe. The HSS standard deviation was 1.28 ksi which was lower than the FEA S_{33} standard deviation of 1.78 ksi.
- *0.5t HSS Method* – These HSS values were very consistent across the range of mesh densities. The average HSS value was 20.3% lower than the FEA maximum S_{33} value calculated directly at the weld toe. The HSS

has a standard deviation of 0.926 ksi which is lower than the FEA maximum S_{33} stress calculated at the weld toe standard deviation of 1.78 ksi.

- *Nihei HSS Method* – The average HSS value was 10.2% lower than the FEA maximum S_{33} values calculated directly at the weld toe and had a standard deviation of 1.36 ksi. The HSS standard deviation of 1.36 ksi was lower than the FEA maximum S_{33} standard deviation of 1.78 ksi.
- *Two-Plane Structural Stress Method* – Two planes passing through the two nodes closest to the weld toe were used to calculate the structural stress. The average value of SS was 3.12% higher than the FEA maximum S_{33} value calculated directly at the weld toe. The SS standard deviation was 0.700 ksi which was lower than the FEA maximum S_{33} standard deviation of 1.78 ksi.

As shown in Tables 3-1 through 3-8, different methods produced different stress values depending on mesh density.

3.6.5 ONE-PLANE STRUCTURAL STRESS ANALYSIS

As discussed above, this analysis method was completed twice on two different planes for the same mesh density to determine if consistent results could be achieved. Because stresses normal to the plane through the weld toe were the

most important to estimate fatigue initiation life, this analysis procedure was only completed on S_{33} data for a mesh density of 0.05 in./element. The two planes that were studied intersected points adjacent to the weld toe as shown in Figure 3-9. Results from these two calculations are discussed below:

- Analysis 1 – Based on stress data at a plane that intersects the first node closest to the weld toe (red plane in Figure 3-9): Using stresses in the 3-3 direction, along with shear stresses normal to this direction and through the thickness of the web, a structural stress of 2.86 ksi was calculated (Appendix A). This structural stress value was very low compared to the HSS values shown in Table 3-7.
- Analysis 2 – Based on stress data at a plane that intersects the second node closest to the weld toe (blue plane in Figure 3-9): Using the stresses in the same direction as those in Analysis 1, a structural stress value was calculated as -16.8 ksi which indicated compression (Appendix A). This value did not correspond well with the value calculated in Analysis 1 using this method.

Because of the large difference in results and the inconsistency found in Analysis 2, it was decided to avoid the use of the one-plane structural stress method for this study.

3.6.6 TWO-PLANE STRUCTURAL STRESS ANALYSIS

As previously discussed, inconsistent results were found using two different sets of planes for the same mesh density. Using maximum principal stress values, SS analyses were performed on the two sets of planes shown in Figure 3-10 and Figure 3-11. The first set of planes (Figure 3-10) produced a SS value of 38.2 ksi. The second set of planes (Figure 3-11) produced a SS value of 27.5 ksi. This 10.7 ksi difference was considered to be quite large because the two sets of planes were very close to each other. The reason this difference was important is because the placement of strain gauges will not be as exact as the placement of the nodes in the FE model.

Because the calculated values of SS were very sensitive to the location of the intersecting planes, it was decided that this method would not be used for this study.

3.7 CONVERGENCE STUDY CONCLUSIONS

Finite element models were developed for a single span, three girder bridge system (described in Chapter 2) to study the magnitude of web-gap stresses that occur in the exterior girders of the bridge when subjected to a single point load on the interior girder. These models were used to determine if the magnitude of the critical web-gap stress between the connection plate and the top flange would converge with increasing mesh density. From the results of the FE models,

it was shown that the magnitude of maximum principal stress did not converge with increasing mesh density. Because of this, different stress analysis procedures were evaluated in an attempt to quantify in a more precise manner the stress demand at the weld toe of the structure. The stress analysis techniques evaluated included the Hot Spot Stress (HSS) analysis, which involves a one-point procedure or a two-point extrapolation procedure, and the Structural Stress (SS) procedure.

After analyzing results obtained with the different stress analysis procedures, it was concluded that both the one-plane and two-plane SS methods did not provide a precise measure of stress demand at the weld toe of the web-gaps investigated in this study. Stress demands calculated using both of these methods gave very inconsistent results, and therefore were not used for any further analysis.

The HSS analysis procedures provided more acceptable results. As shown in Table 3-1, all of the analysis procedures provided fairly consistent results across the range of mesh densities (with a few outliers). The easiest, and seemingly most reliable procedures, were found to be the 0.5t/1.5t two-point procedure and the 0.5t one-point procedure. These two procedures produced the lowest range of stress values for the range of mesh densities that were considered.

Although these HSS analysis procedures produced consistent results, there was some level of discrepancy in the calculated stress demands for the various mesh densities. However, both methods represented an improvement over the use

of peak stresses obtained directly from the FE model, and both methods were useful in eliminating the variability introduced by the mesh configuration of different FE models.

For the purpose of comparing the stress demands calculated with FE models in the un-retrofitted and retrofitted bridge details, the 0.5t HSS method was adopted because it produced the lowest standard deviation using the maximum principal stresses (the structural stress procedure had already been eliminated for an analysis method). Therefore, all stress demands calculated for comparison of un-retrofitted and retrofitted details (shown in Chapter 4) were read at a distance of 0.5t away from the weld toe. The use of hot spot stresses on maximum principal stress results may be the best indicator of retrofit effectiveness because of the inability to estimate correctly which direction a crack will propagate. For this reason, the maximum principal hot spot stress results will be the primary tool for investigating retrofit effectiveness. S_{11}, S_{22}, and S_{33} stress directions will also be studied but will not be the primary factor in identifying effective retrofits.

Table 3-9 Convergence Study Standard Deviations

Standard Deviations of Stress Analysis Procedures (ksi)

	FEA Max	**0.4t/1.0t**	**0.5t/1.5t**	**0.5t**	**Nihei**	**Structural Stress (2-Plane)**
Max. Principal Stress	5.61	4.80	4.30	3.02	3.98	0.602
S_{11}	5.88	7.21	6.06	3.98	4.72	0.391
S_{22}	4.23	10.1	7.75	4.35	5.27	3.67
S_{33}	1.78	1.28	1.28	0.926	1.36	0.700

CHAPTER 4 – RETROFIT INVESTIGATION

Finite element (FE) models of the KU Test Bridge model described in Chapter 2 were created to study the behavior of the transverse stiffener web-gap detail described in Chapter 1. Several models of the non-retrofitted (shown in Figure 2-7) and retrofitted (shown in Figure 2-8) configurations were built using the commercially available finite element software ABAQUS v.6.8-2. In addition to established retrofitting schemes, other retrofit measures to reduce the magnitude of stress demand at the web-gap were examined. The new retrofit schemes that were evaluated rely on the use of Carbon Fiber Reinforced Polymers (CFRP, both chopped and continuous fiber configurations) to stiffen the web-gap region and to provide an additional load path for secondary stresses. These two effects combine to reduce the stress demand at the weld toe. Both continuous and chopped fiber reinforced polymers were examined to determine if there was a difference in the effectiveness of the two retrofit measures. Chopped fiber composites may be better suited for application in the field because the material can be sprayed onto the web-gap region saving time and money on manufacturing costs (continuous fiber reinforced polymers must be prefabricated in a shop and attached in the field).

4.1 CFRP MATERIAL PROPERTIES

The material properties for the CFRP (chopped and continuous fiber) were obtained from tensile tests consistent with ASTM D3039 (2000) – Standard Test Method for Tensile Properties of Polymer Matrix Composite Materials. Both composite materials were modeled as isotropic linear-elastic. It is worth noting that this assumption has its limitations because depending on the orientation of the fibers, composite materials may be significantly anisotropic. In the case of the two types of composite materials evaluated, the chopped fiber composites would be closest to exhibiting isotropic behavior due to the random orientation of the fibers. The modulus of elasticity of the chopped fiber composite was measured from tensile tests, and it was found to be 2,000 ksi, with a Poisson's ratio of 0.1; the modulus of elasticity for the continuous fiber composite was measured as 3,858 ksi, with a Poisson's ratio of 0.1.

4.2 CFRP CONFIGURATIONS

Multiple CFRP retrofit configurations were modeled to determine the effectiveness of each scheme in reducing the stress demand in the web-gap region. The configuration of the CFRP overlays was developed based on two established retrofit measures for this type of detail. The first of the two established retrofit measures is based on the idea of fixing the connection plate to the top flange, which creates a positive attachment and decreases the level of web-

gap stress. The second retrofit measure, developed at the University of Kansas by Kaan (2008), uses CFRP overlays to create an alternative load path to reduce the magnitude of stress at the weld toe of a partial length cover plate, shown in Figure 1-23. The combination of these two concepts led to the CFRP shapes shown in Figures 4-1 through 4-11. All of the shapes were assumed to be adhesively bonded to the connection plate, girder web, and the underside of the top flange of the girder.

The first retrofit measure (shown in Figure 4-1) used CFRP (variations utilizing chopped and continuous fiber were considered) on both sides of the connection plate. It is important to note that this configuration did not include placement of composite material in the web-gap region above the connection plate.

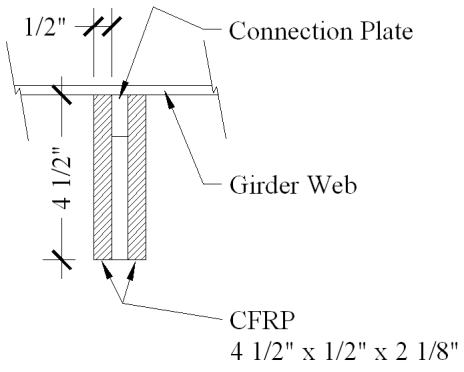

Figure 4-1 CFRP (chopped and continuous) retrofit A - 0.5 in. thick composite (plan view)

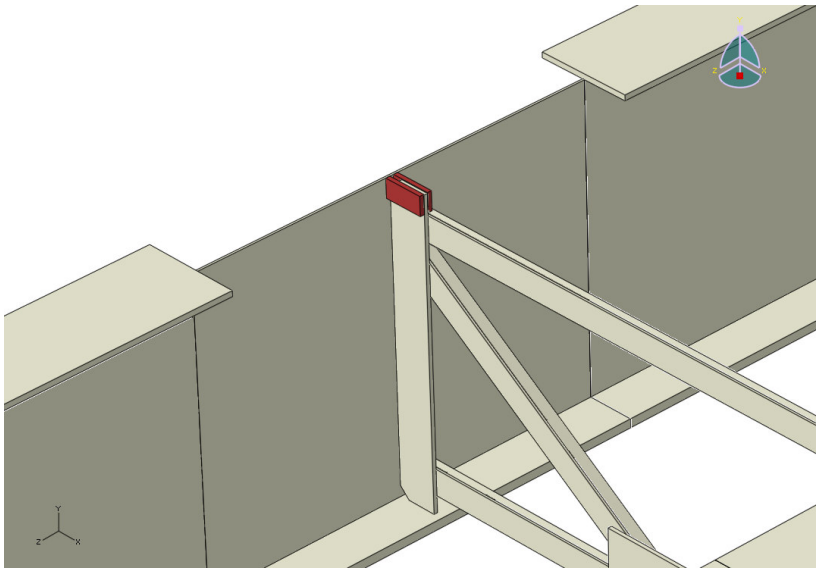

Figure 4-2 3D view of CFRP (chopped and continuous) retrofit A - 0.5 in. thick composite (concrete deck and portion of top flange removed)

The second retrofit measure (shown in Figure 4-3) is very similar to the configuration shown in Figure 4-1. The only difference is that the configuration shown in Figure 4-3 utilizes composite material above the connection plate in the web-gap region. The 3D view of this retrofit measure is similar to Figure 4-2, except that composite material does exist in the web-gap.

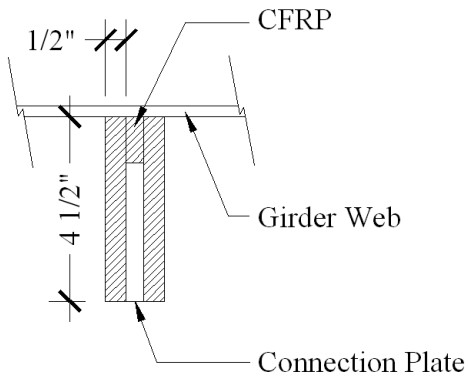

Figure 4-3 CFRP (chopped and continuous) retrofit A - 0.5 in. thick composite gap filled (plan view)

The third retrofit measure (Figure 4-4) was also a variation of the configuration shown in Figure 4-1. This configuration, however, was twice as thick and also did not include composite material above the connection plate in the web-gap region.

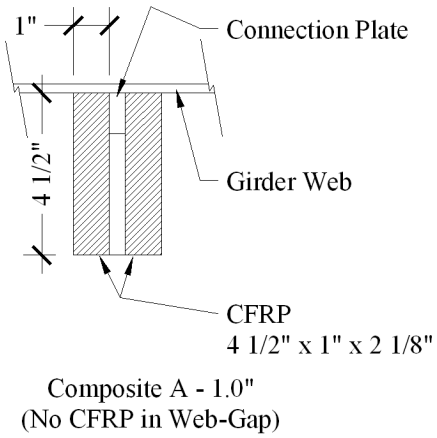

Figure 4-4 CFRP (chopped and continuous) retrofit A - 1.0 in. thick composite (plan view)

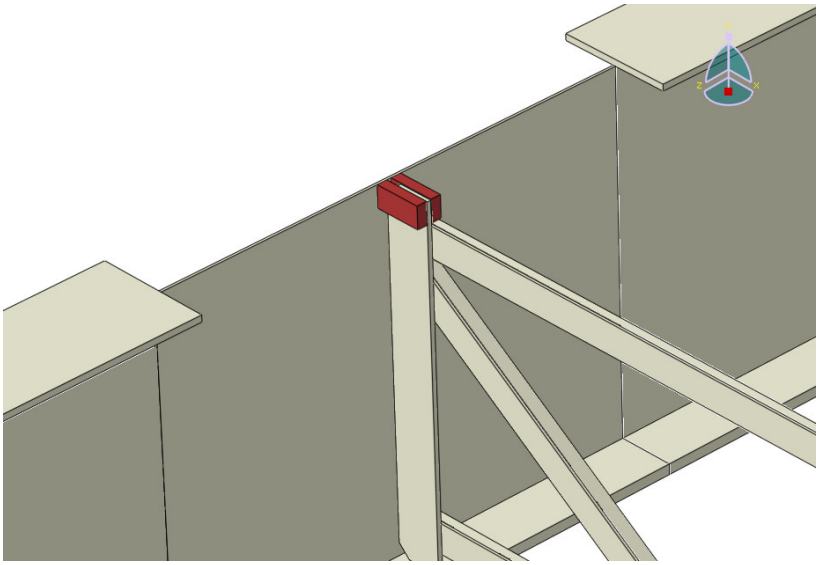

Figure 4-5 3D view of CFRP (chopped and continuous) retrofit A - 1.0 in. thick composite (concrete deck and portion of top flange removed)

The fourth retrofit was also a variation of the first retrofit shown in Figure 4-1. This retrofit involved using a 1/8 in. epoxy resin layer between the composite and all contacted steel surfaces. The resin layer was modeled having a modulus of elasticity of 500 ksi and a Poisson's ratio of 0.1. The resin layer was modeled to investigate the effect of field installation on the effectiveness of prefabricated composite overlays. For this reason, this model was only analyzed using continuous carbon fiber.

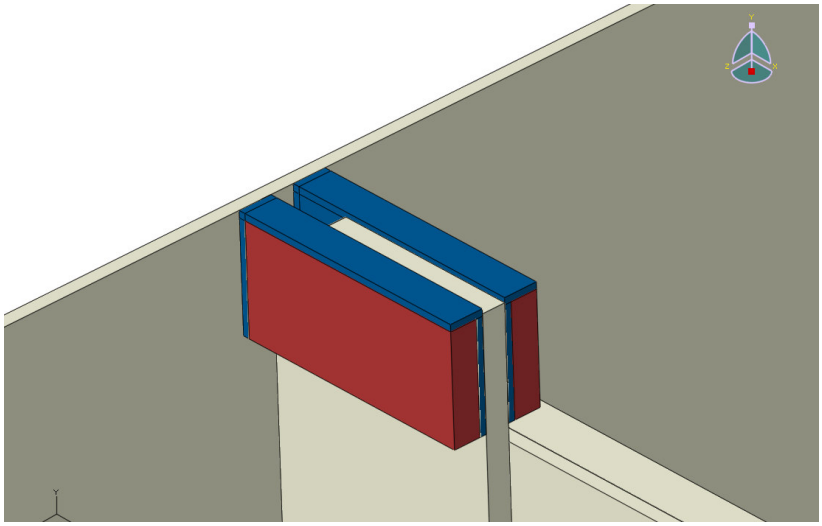

Figure 4-6 3D view of CFRP (continuous fiber) retrofit A - 0.5 in. thick composite with 1/8 in. resin layer (resin layer designated in blue)

A different geometry was used in the fifth retrofit measure (Figure 4-7), in which an L-shape was used to determine the effect of the length of the overlay on the magnitude of web-gap stress. The composite overlay had a thickness of 0.5 in. and extended for a length of 1 ft. – 0 in. on each side of the connection plate. No composite material was utilized above the connection plate in the web-gap region.

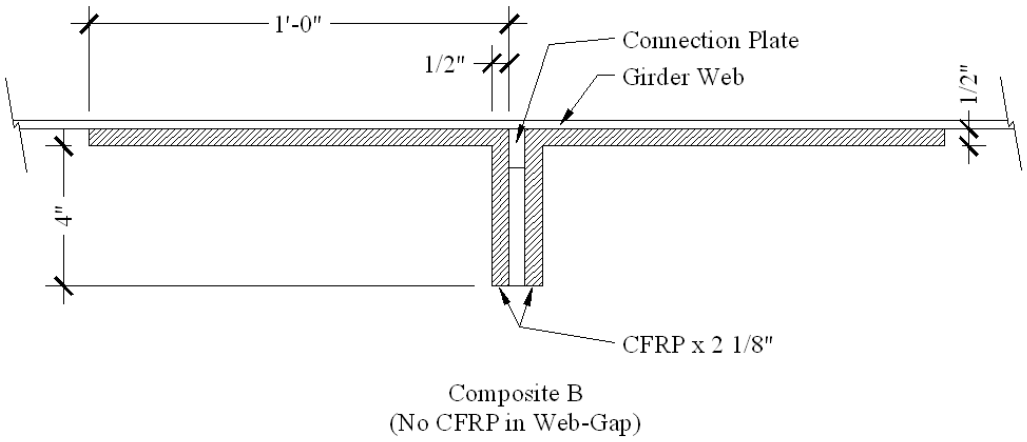

Figure 4-7 CFRP (chopped and continuous) L-shaped retrofit B (plan view)

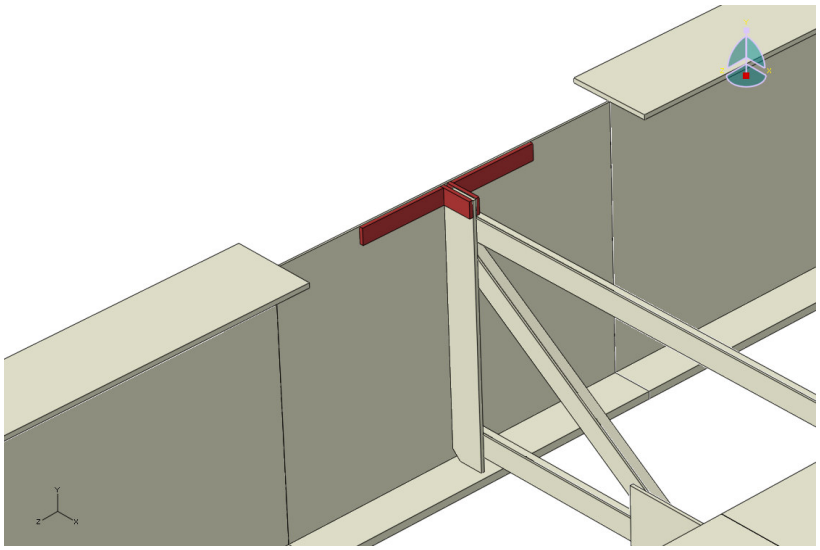

Figure 4-8 3D view of CFRP (chopped and continuous) L-shaped retrofit B (concrete deck and portion of top flange removed)

The sixth and final retrofit configuration (Figure 4-9) was a modified version of the scheme shown in Figure 4-7, except that the L-shape was thickened to stiffen the region on both sides of the connection plate. Composite material was not used above the connection plate in the web-gap region.

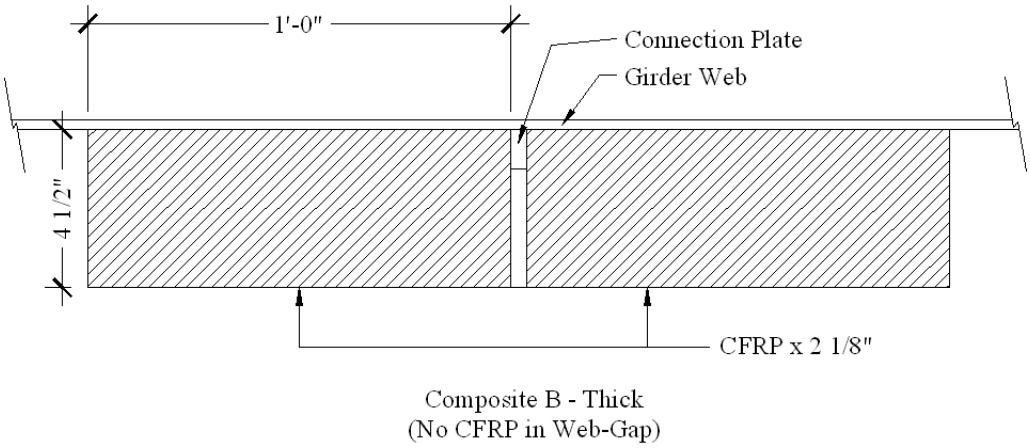

Figure 4-9 CFRP (chopped and continuous) retrofit B – thick (plan view)

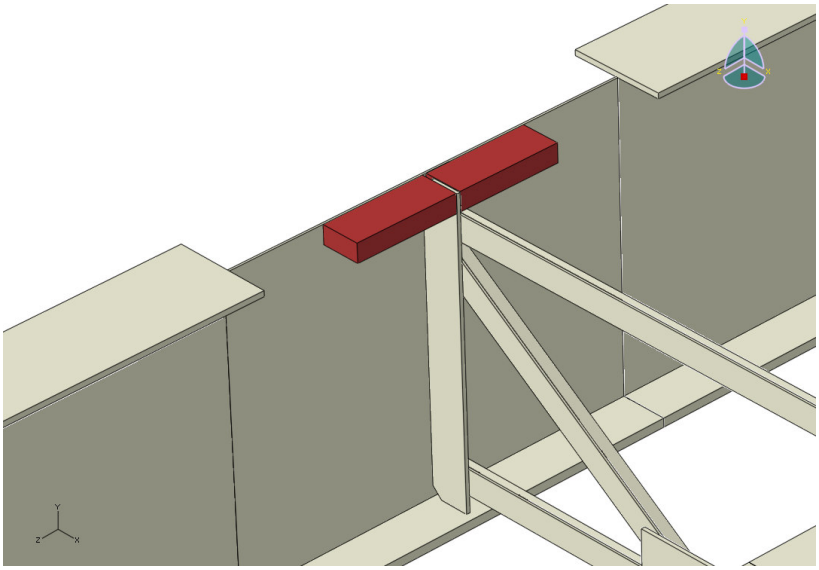

Figure 4-10 3D view of CFRP (chopped and continuous) retrofit B - thick (concrete deck and portion of top flange removed)

All of the above retrofitting schemes had the same length (2 1/8”). The controlling factor on the length of these CFRP material overlays was the location of the cross-bracing; the composite materials were stopped short of the bracing for modeling purposes as shown in Figure 4-11.

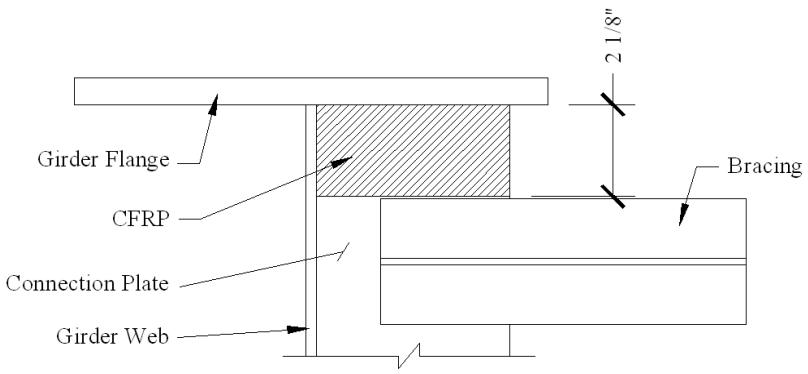

Figure 4-11 All CFRP retrofits (section view)

Stress demands from retrofitting schemes using CFRP material overlays were compared with those resulting from the implementation of the established retrofit measures found in the literature (slot repair and positive attachment repair) and with the stress demands calculated for the non-retrofitted web-gap detail.

4.3 FINITE ELEMENT RESULTS

Maximum principal, S_{11}, S_{22}, and S_{33} stress paths with Hot Spot Stresses (HSS) were examined to study the effectiveness of the established and the developed CFRP retrofits. Stress paths were defined for both the chopped and continuous fiber reinforced polymer retrofits and are shown in Figure 4-12 through Figure 4-19; these stresses were taken along the path shown in Figure 3-12. Also, HSS values were calculated for each retrofit measure and are shown in Tables 4-1 and 4-2. Deformed shapes of the non-retrofitted and retrofitted details were also given along with maximum principal stress fringe plots for each model.

4.3.1 NOTATION

The following notation was used in the following figures and sections to describe the non-retrofitted and retrofitted transverse stiffener web-gap details.

- *Non-Retrofitted – Rect*: a rectangular connection plate was used with a 1 1/4" web-gap as shown in Figure 2-7 (a).
- *Non-Retrofitted – Clip:* a clip connection plate with a 1 1/4" web-gap was used as shown in Figure 2-7 (b).
- *Fixed Repair:* the clip connection plate was rigidly connected to the top flange as shown in Figure 2-8 (a).
- *Slot Repair:* a slot was created in the clip connection plate to soften the connection as shown in Figure 2-8 (b).
- *Carbon Fiber A – 0.5 in:* chopped and continuous fiber retrofits with a thickness of 0.5" on both sides of the clip connection plate were used as shown in Figure 4-1.
- *Carbon Fiber A – 0.5 in Gap Filled:* chopped and continuous fiber retrofits with a thickness of 0.5" on both sides of the clip connection plate were used. Also, the gap between the connection plate and top flange was filled with composite as shown in Figure 4-3.
- *Carbon Fiber A – 1.0 in:* chopped and continuous fiber retrofits with a thickness of 1.0" on both sides of the clip connection plate were used as shown in Figure 4-4.

- *Cont. Fiber A – 0.5 in w/ resin:* continuous fiber retrofit with a thickness of 0.5" including a 1/8" resin layer between the composite and all steel surfaces was used.
- *Carbon Fiber B:* chopped and continuous fiber retrofits in an "L" shaped were used on both sides of the clip connection plate as shown in Figure 4-7.
- *Carbon Fiber B – Thick:* chopped and continuous fiber retrofits of the thickened "L" shape were used on both sides of the clip connection plate as shown in Figure 4-9.

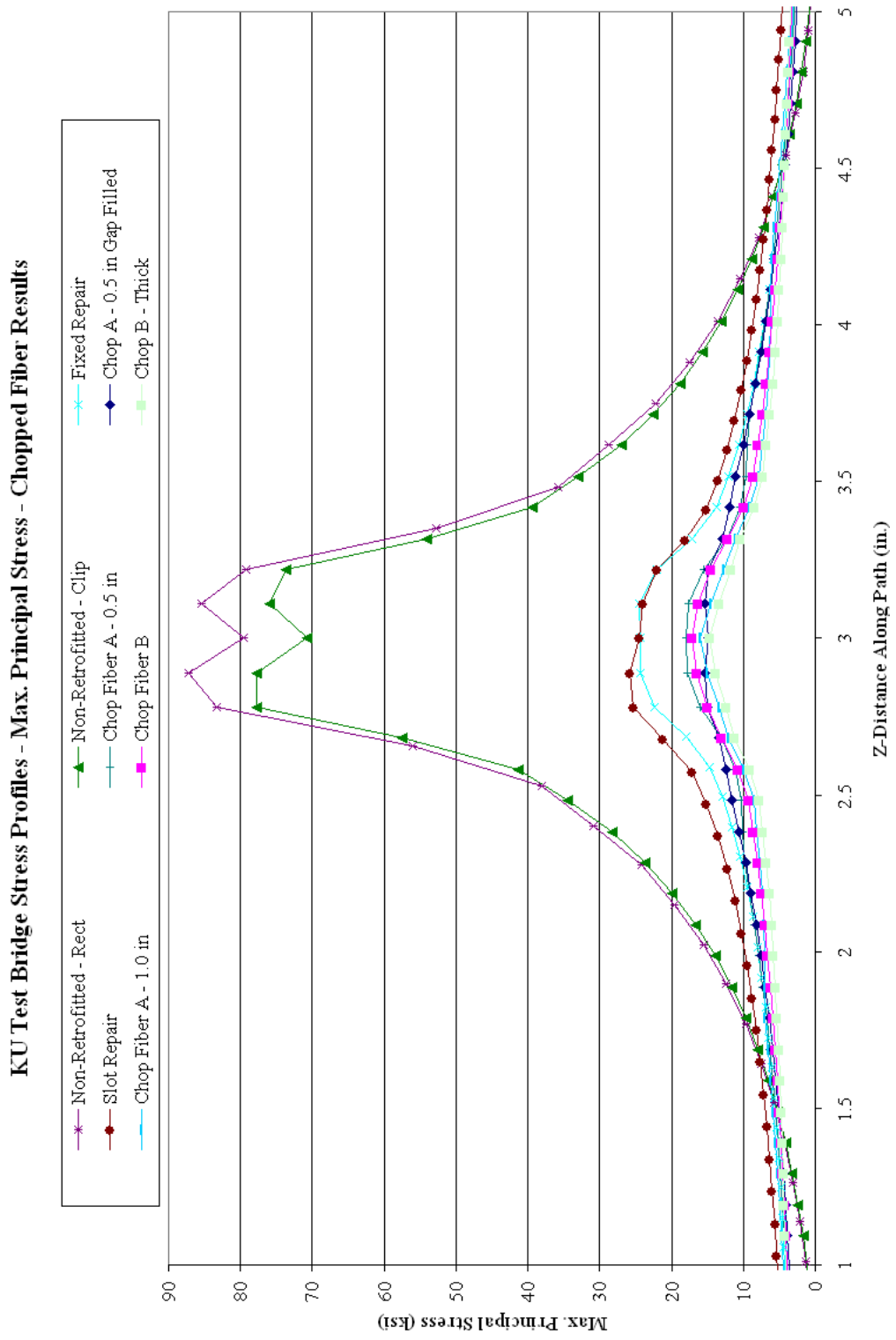

Figure 4-12 Maximum principal stress - chopped fiber retrofit results

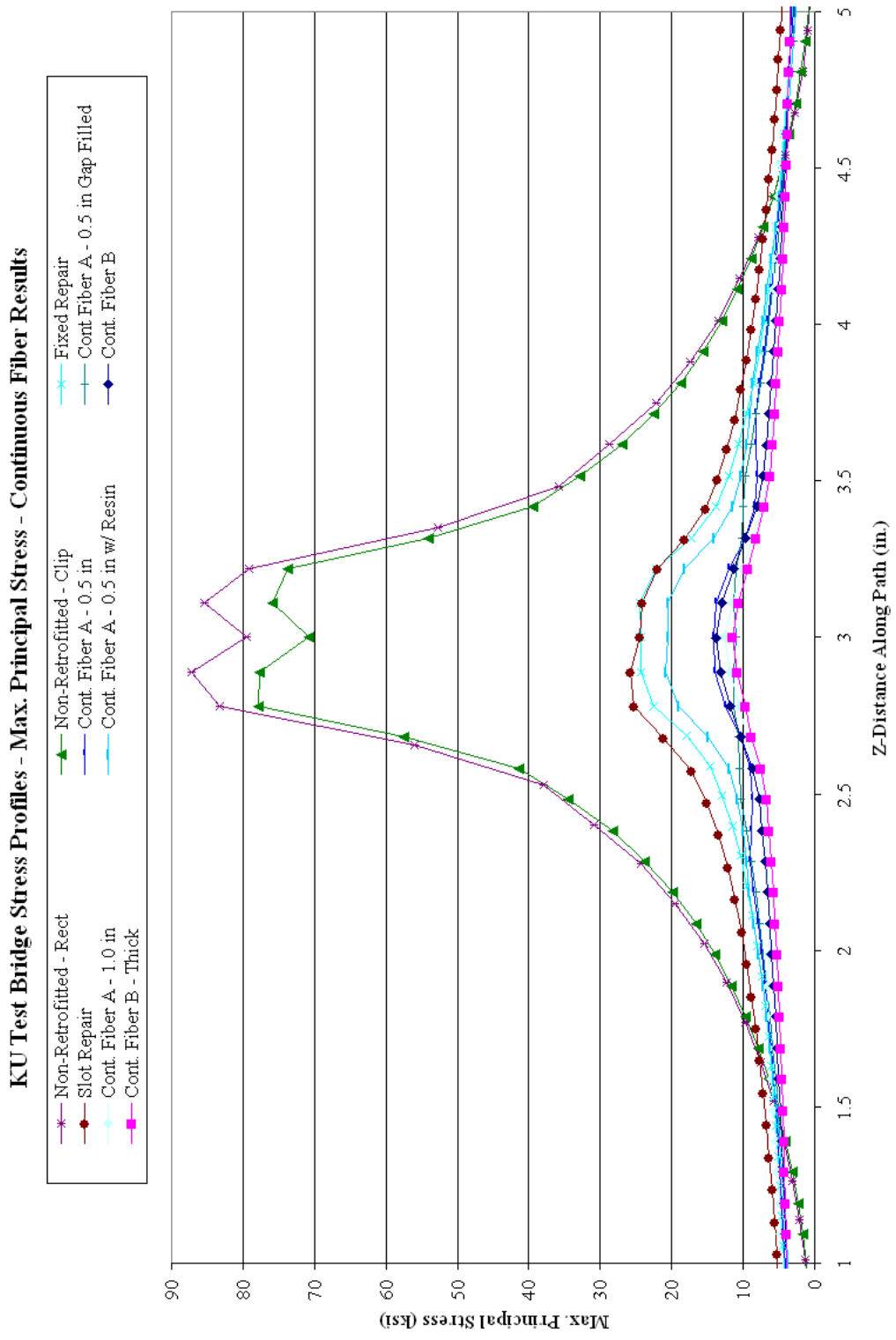

Figure 4-13 Maximum principal stress - continuous fiber retrofit results

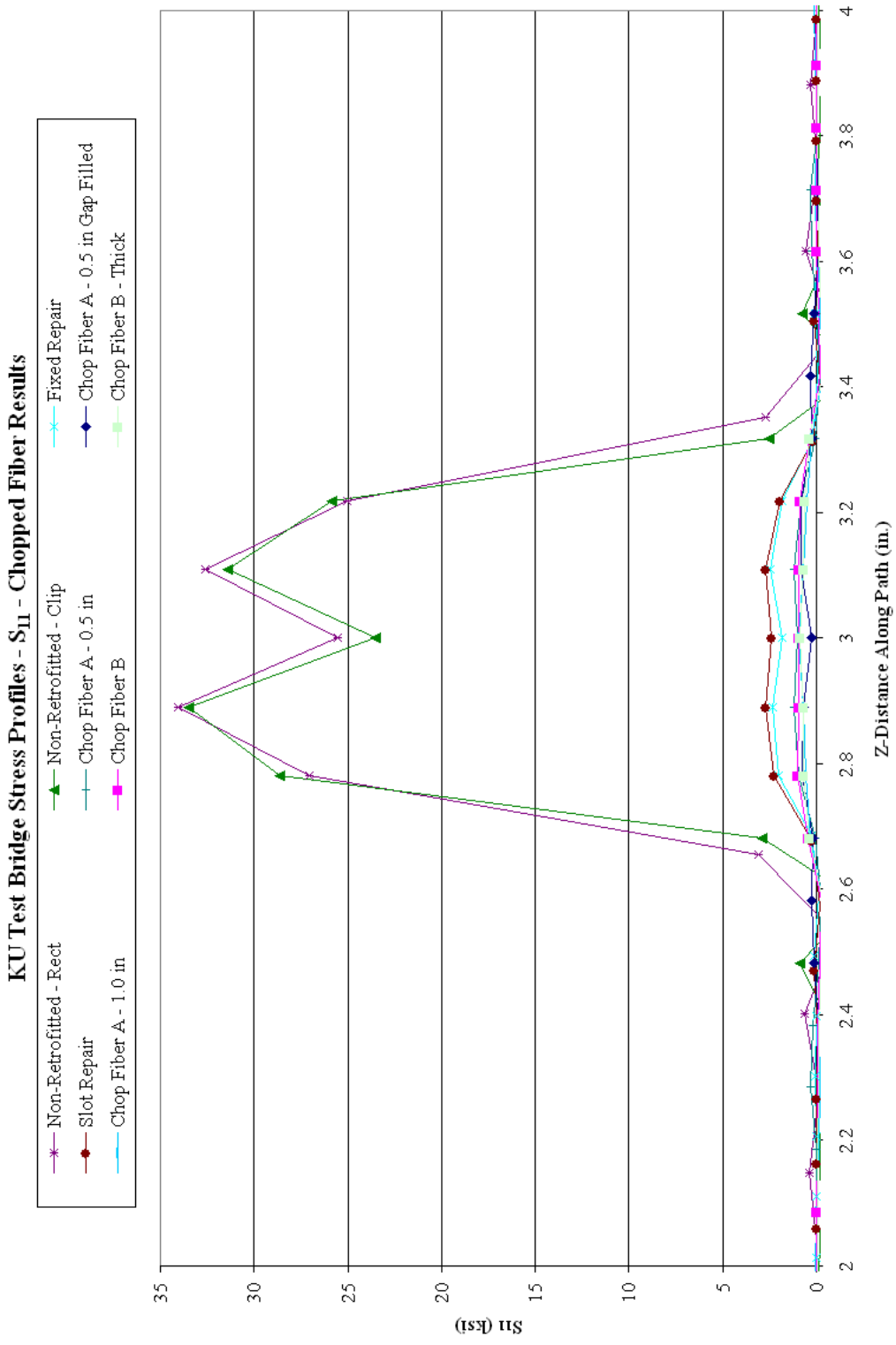

Figure 4-14 S_{11} - chopped fiber retrofit results

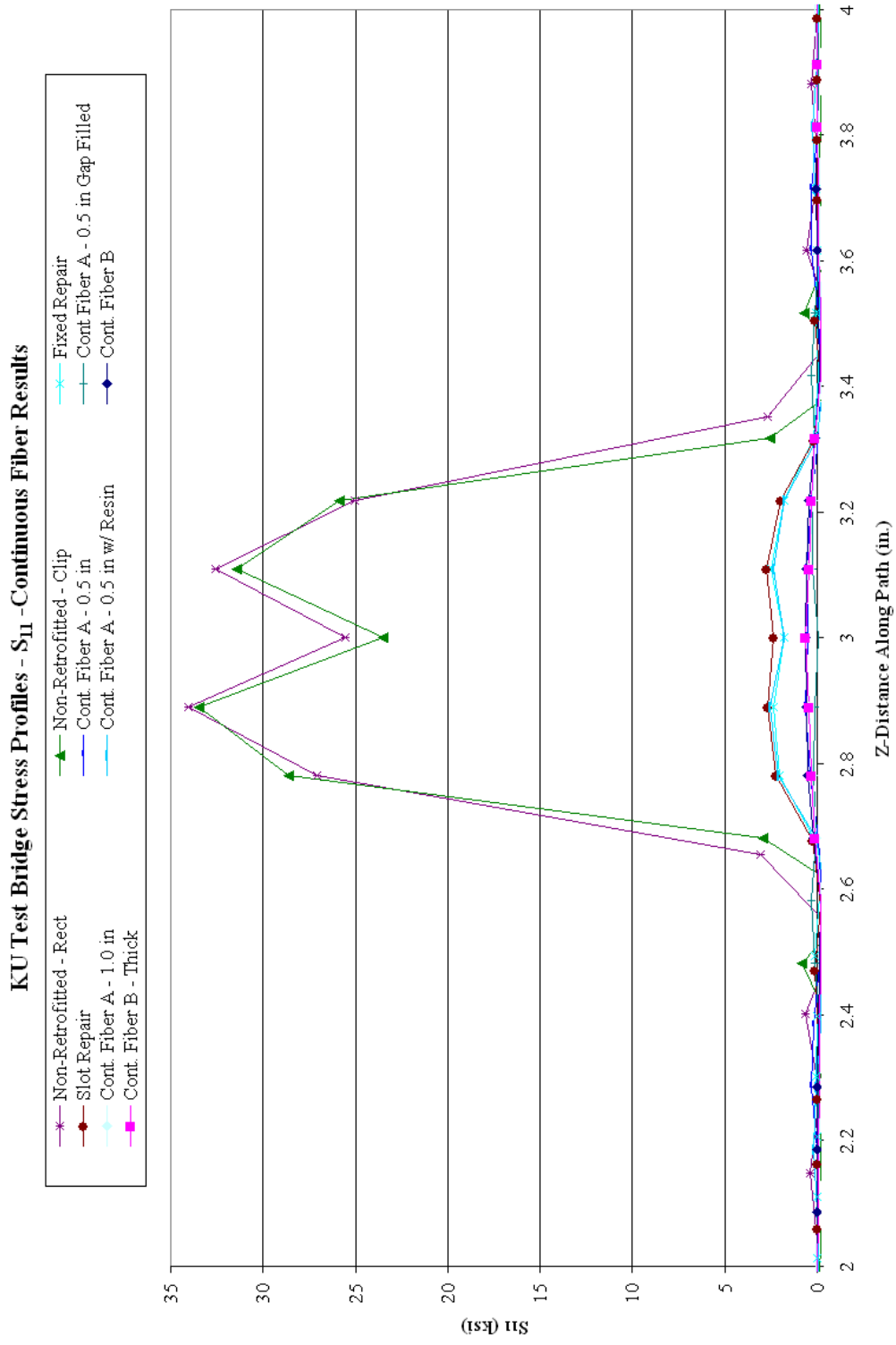

Figure 4-15 S_{11} - continuous fiber retrofit results

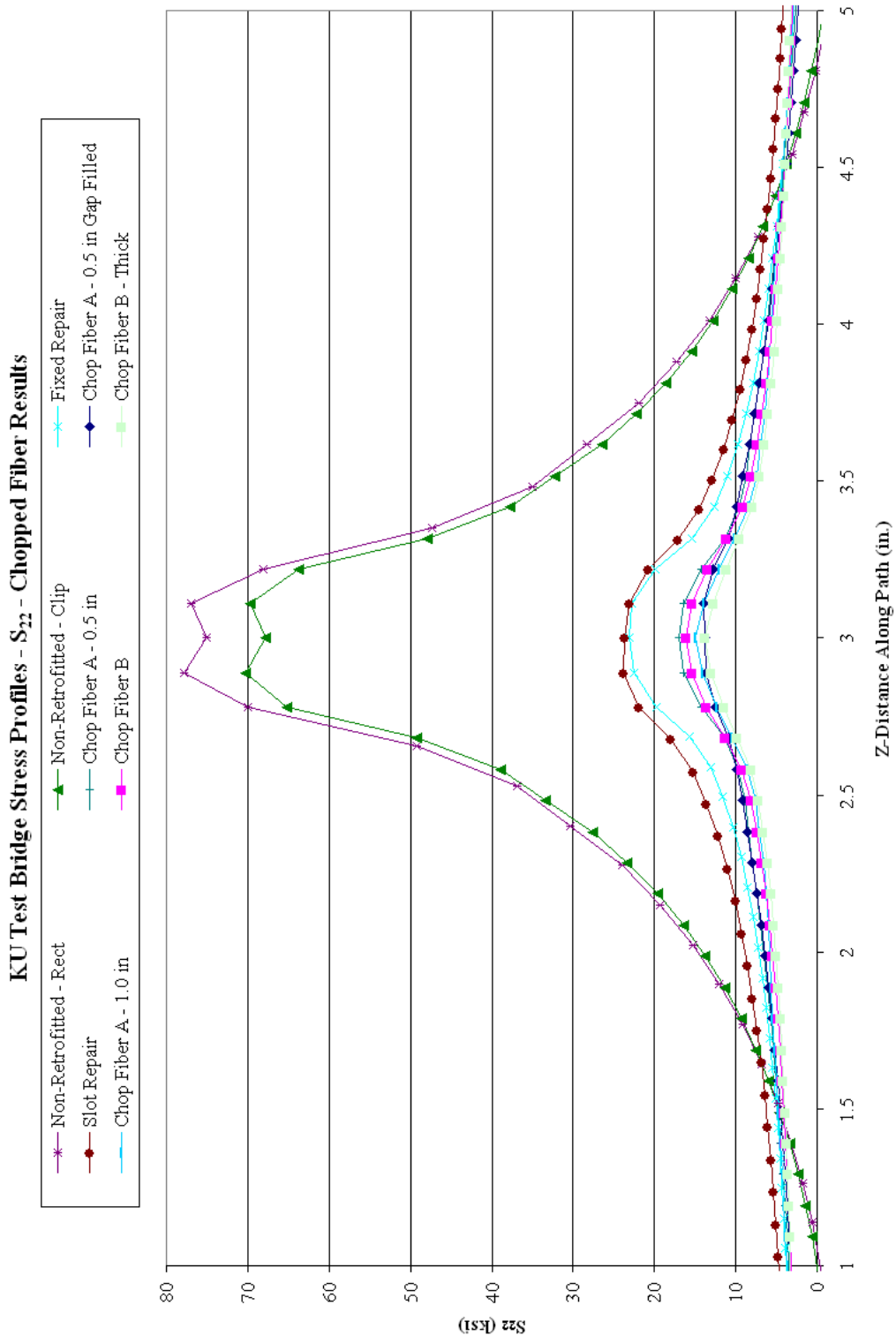

Figure 4-16 S_{22} - chopped fiber retrofit results

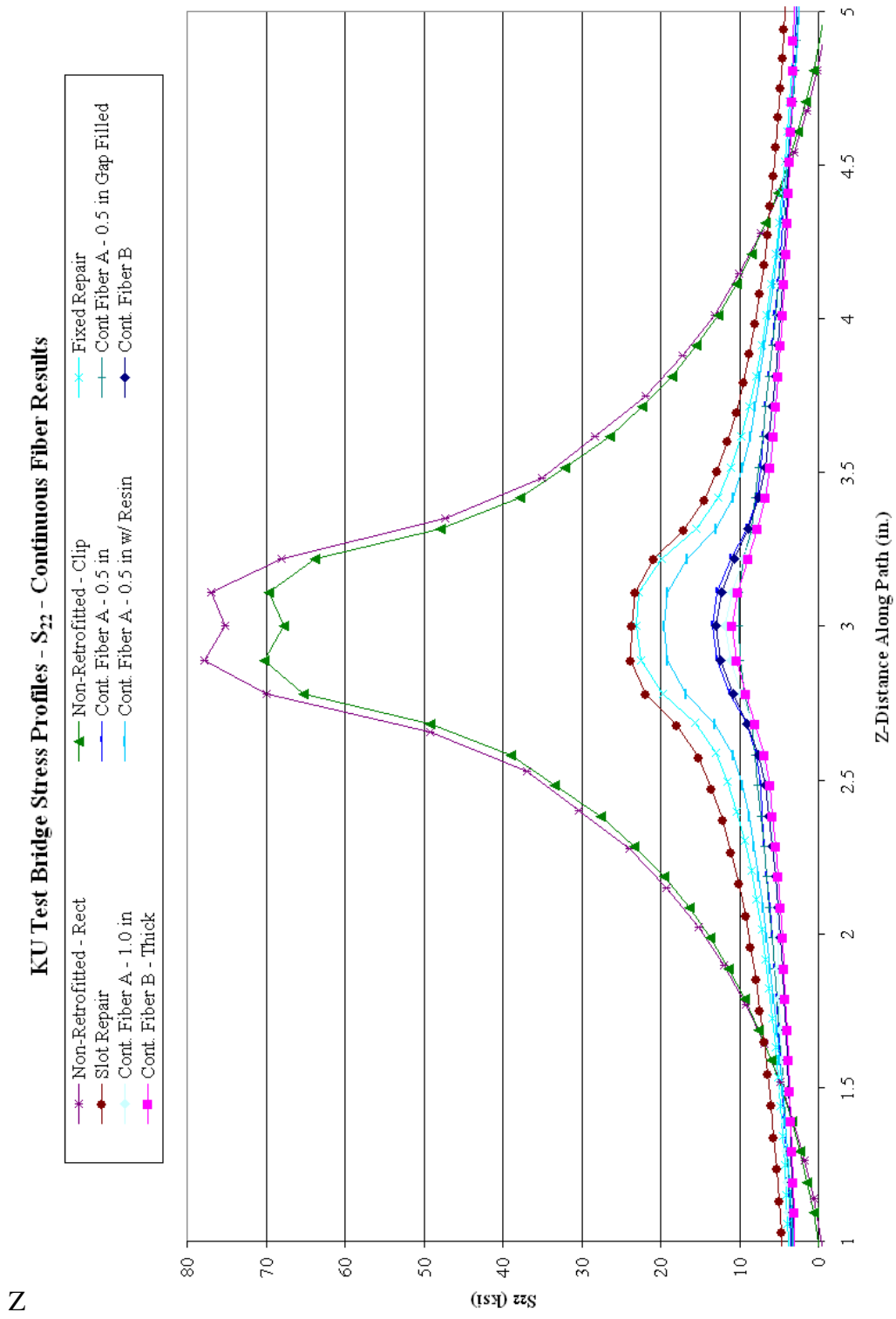

Figure 4-17 S_{22} - continuous fiber retrofit results

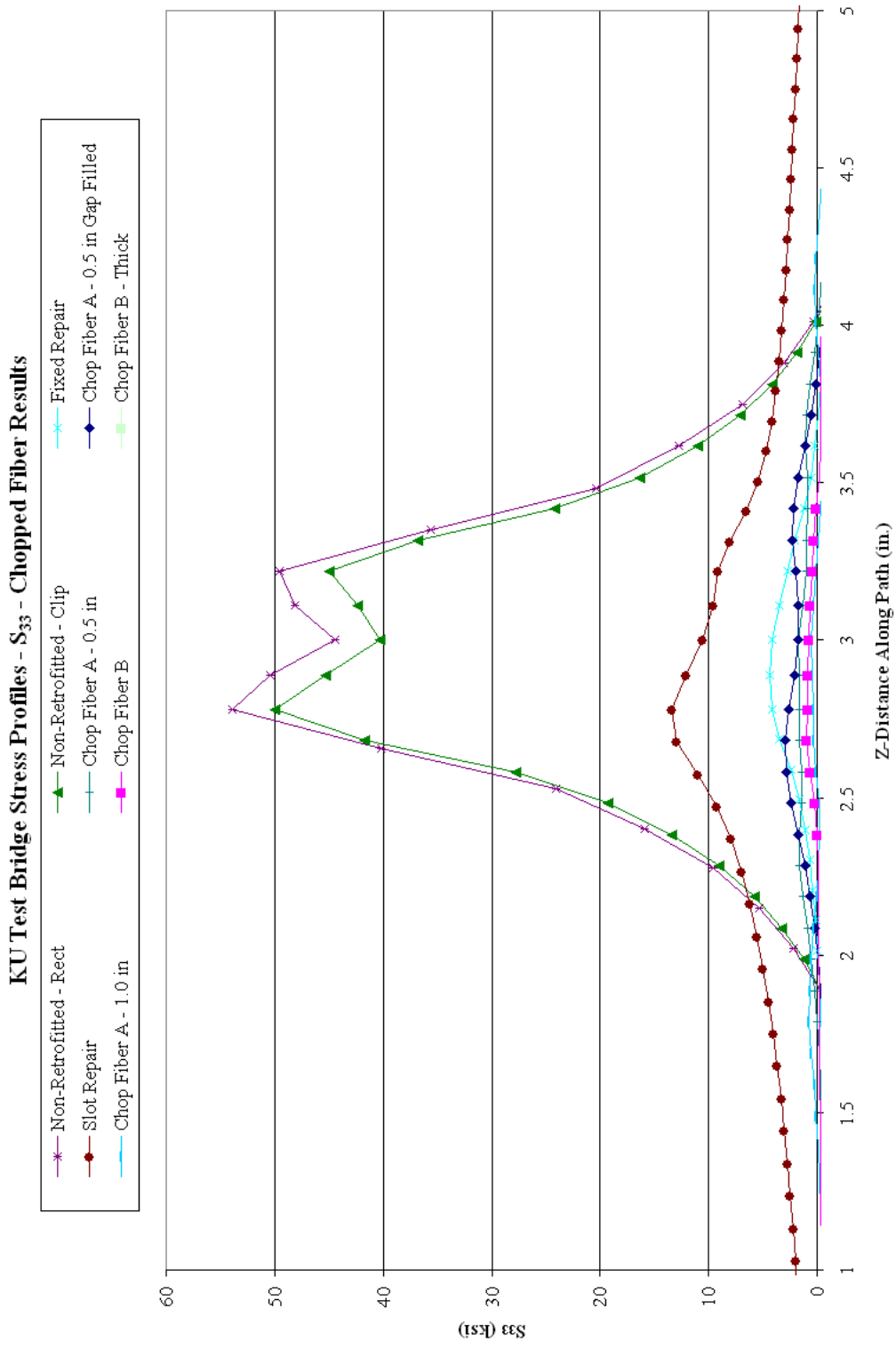

Figure 4-18 S_{33} - chopped fiber retrofit results

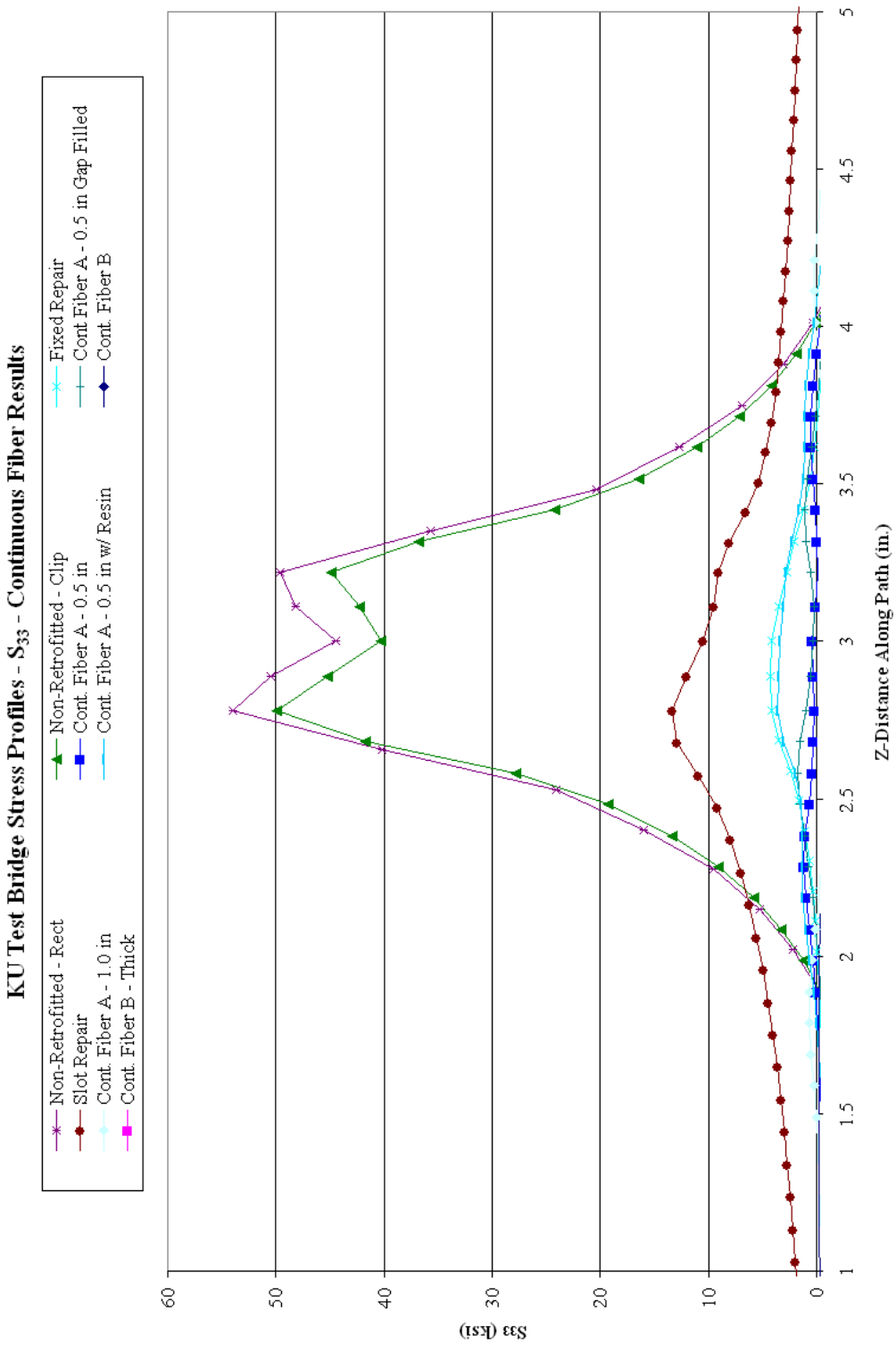

Figure 4-19 S_{33} - continuous fiber retrofit results

Table 4-1 Chopped Fiber Retrofit HSS Results

	Hot Spot Stresses (ksi)			
	Max. Principal	S_{11}	S_{22}	S_{33}
As Is - Rect. Plate	56.2	3.30	49.5	40.5
As Is - Clip Plate	53.2	1.50	46.4	37.9
Fixed to Top Flange	16.9	0.20	14.8	3.20
Slot Repair	20.3	0.20	17.4	12.5
Chopped Fiber A - 0.5"	12.5	0.03	10.9	1.50
Chopped Fiber A - 0.5" Gap Filled	13.1	0.20	10.6	2.90
Chopped Fiber A - 1.0"	11.6	0.20	10.0	0.20
Chopped Fiber B	12.4	0.30	10.8	0.90
Chopped Fiber B - Thick	10.6	0.20	9.40	-0.90

Table 4-2 Continuous Fiber Retrofit HSS Results

	Hot Spot Stresses (ksi)			
	Max. Principal	S_{11}	S_{22}	S_{33}
As Is - Rect. Plate	56.2	3.30	49.5	40.5
As Is - Clip Plate	53.2	1.50	46.4	37.9
Fixed to Top Flange	16.9	0.20	14.8	3.20
Slot Repair	20.3	0.20	17.4	12.5
Cont. Fiber A - 0.5"	10.0	-0.10	8.80	0.40
Cont. Fiber A - 0.5" Gap Filled	10.7	0.10	8.30	1.60
Cont. Fiber A - 1.0"	9.10	0.02	8.10	-0.70
Cont. Fiber A - 0.5" w/ Resin	14.1	-0.10	12.5	2.80
Cont. Fiber B	9.90	0.10	8.70	-0.40
Cont. Fiber B - Thick	8.50	0.03	7.70	-2.20

4.3.2 MAXIMUM PRINCIPAL STRESS RESULTS

From the stress paths shown in Figure 4-12 and Figure 4-13, it can be seen that both the chopped and carbon fiber reinforced polymer retrofits reduced the magnitude of web-gap stress more than the slot and positive attachment repairs. This can also be seen from the HSS values shown in Tables 4-1 and 4-2. The CFRP retrofits reduced the magnitude of HSS from approximately 55 ksi for the

non-retrofitted detail to approximately 12 ksi for the chopped fiber and 10 ksi for the continuous fiber. The CFRP retrofits performed better than the slot and positive attachment repairs by approximately 4 to 8 ksi for the chopped fiber and 6 to 10 ksi for the continuous fiber. The retrofit with the resin layer performed slightly better than the slot and positive attachment repairs; this was expected because the stiffness of the overlay decreases when the resin is explicitly modeled. Based on the results from the Finite Element analyses, it is concluded that the CFRP retrofits were very effective in reducing the magnitude of web-gap stress demand, and at least as effective as the other established retrofit measures.

4.3.3 S_{11} STRESS RESULTS

The S_{11} stress path results presented in Figure 4-14 and Figure 4-15 show that attaching CFRP overlays reduced web-gap stress demand more than the slot and positive attachment repairs. The HSS results did not show a significant stress demand in the S_{11} direction for the non-retrofitted or retrofitted details, meaning that the largest stress demands occurred over the width of the connection plate. The CFRP repair with the resin layer performed approximately the same as the slot and positive attachment repairs. The results show that the CFRP retrofits significantly reduced the magnitude of S_{11} stress demand in the web-gap region as compared to the non-retrofitted details.

4.3.4 S_{22} STRESS RESULTS

Stress profiles for the S_{22} direction are shown in Figure 4-16 and Figure 4-17. Both figures show that the CFRP retrofit measures reduced the magnitude of web-gap stress more than the slot and positive attachment repairs. The HSS paralleled these results; the CFRP retrofit measures resulted in lower stress demands in the S_{22} direction, on the order of approximately 6 ksi for the chopped fiber and 8 ksi for the continuous fiber. The CFRP retrofit measure reduced the magnitude of the HSS from approximately 48 ksi to 10 ksi for the chopped fiber and 8 ksi for the continuous fiber. Also, the CFRP retrofit measure with the resin layer performed slightly better than the slot and positive attachment repairs. These reductions in stress demand show that the CFRP overlays constitute an effective retrofit measure in the application studied.

4.3.5 S_{33} STRESS RESULTS

Stress profiles for S_{33} are shown in Figure 4-18 and Figure 4-19. These two figures show that the CFRP retrofit measures reduced the magnitude of web-gap stress demand more than the slot and positive attachment retrofit measures. The HSS results for the chopped and continuous fiber retrofit measures showed a stress demand of approximately 1.0 ksi. This value was significantly lower than the corresponding demand for the slot repair (12.5 ksi), and slightly lower than the positive attachment repair (3.2 ksi). After retrofit, the magnitude of web-gap S_{33} HSS dropped from approximately 39 ksi to 1 ksi for both the chopped and

continuous fibers. The CFRP repair with the resin layer performed much better than the slot repair and slightly better than the positive attachment repair. These reductions in stress demand show that the carbon fiber retrofit measures were effective.

4.3.6 FINITE ELEMENT FRINGE PLOTS

Maximum principal stress fringe plots for non-retrofitted and retrofitted details are presented in this section to show how the retrofit measures decrease the stress demand in the web-gap. Figure 4-20 through Figure 4-58 show maximum principal stress gradients on un-deformed web-gaps on an exterior girder. The legend in the upper left corner of each figure ranges from -20,000 psi to 100,000 psi.

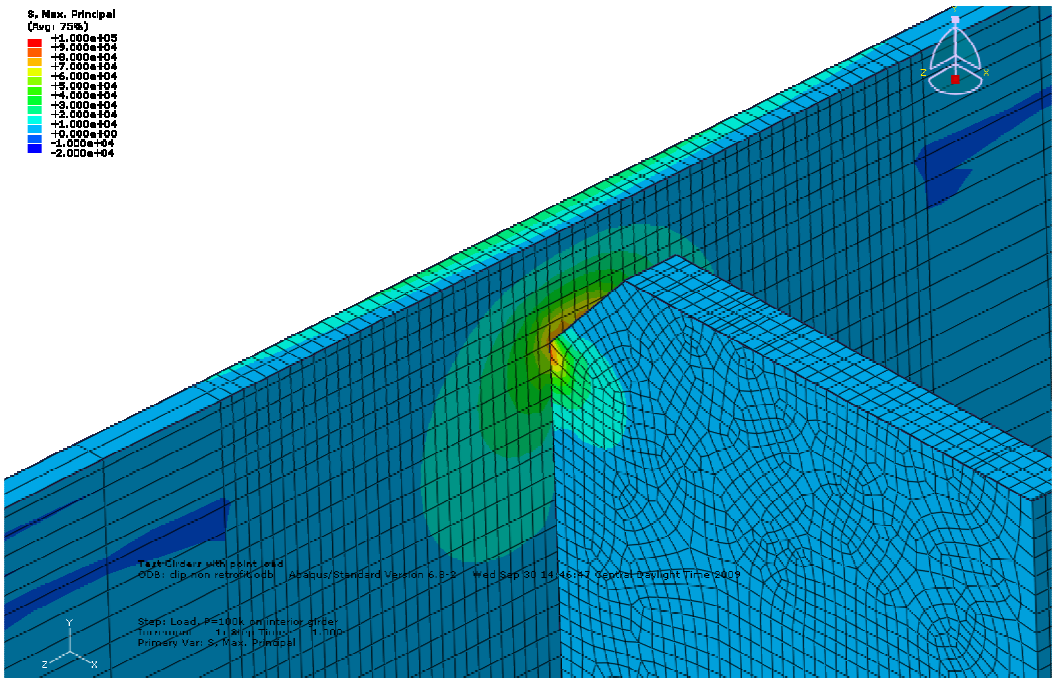

Figure 4-20 Non-retrofitted – clip fringe plot

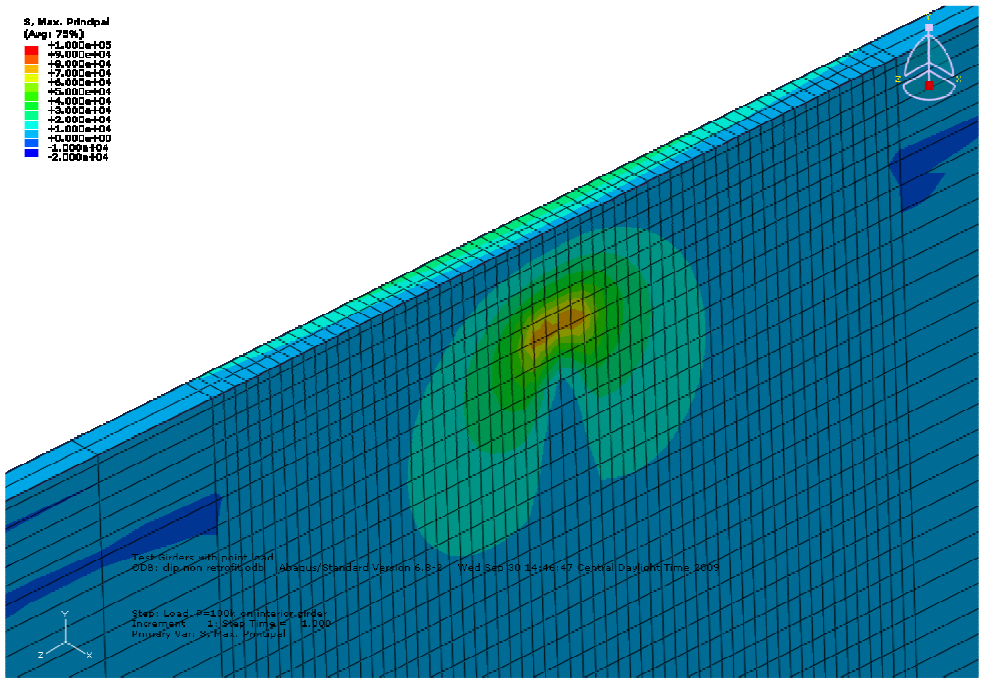

Figure 4-21 Non-retrofitted - clip fringe plot (connection plate removed)

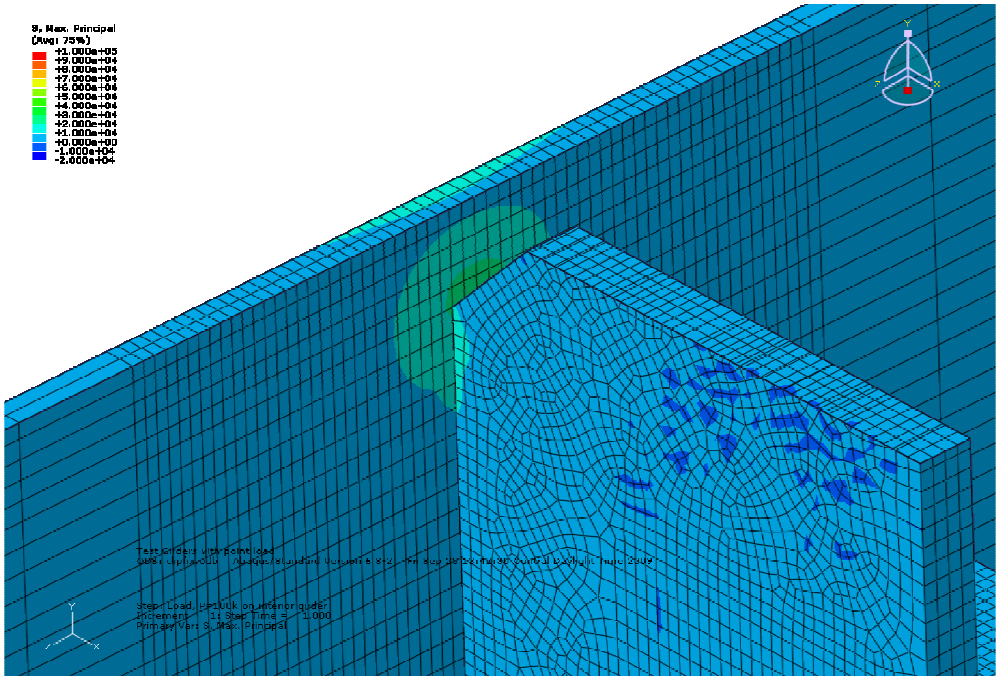

Figure 4-22 Fixed repair fringe plot

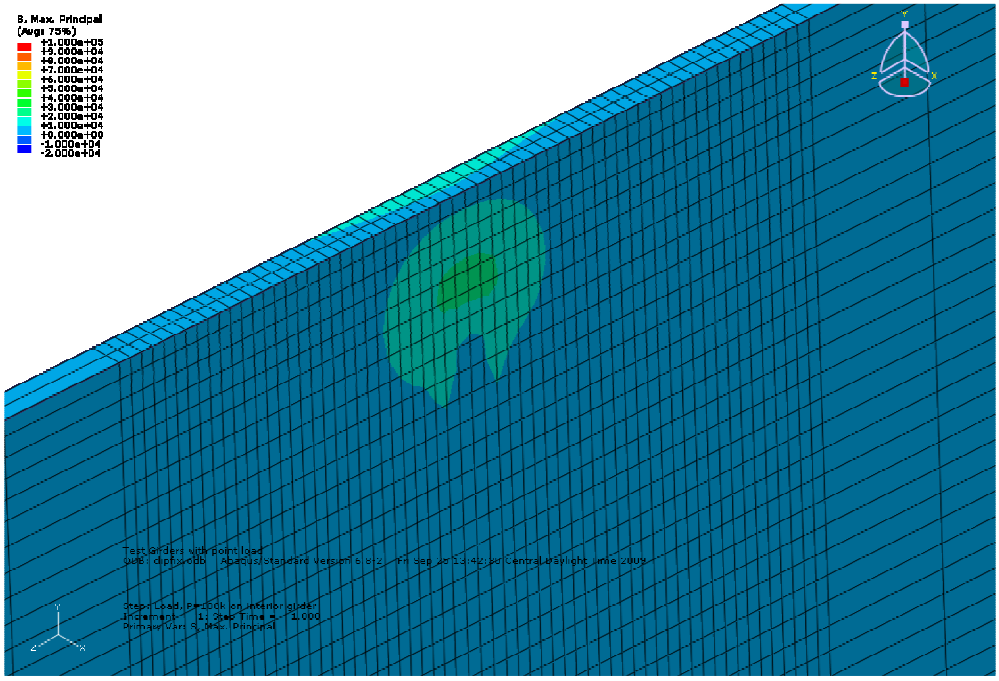

Figure 4-23 Fixed repair fringe plot (connection plate removed)

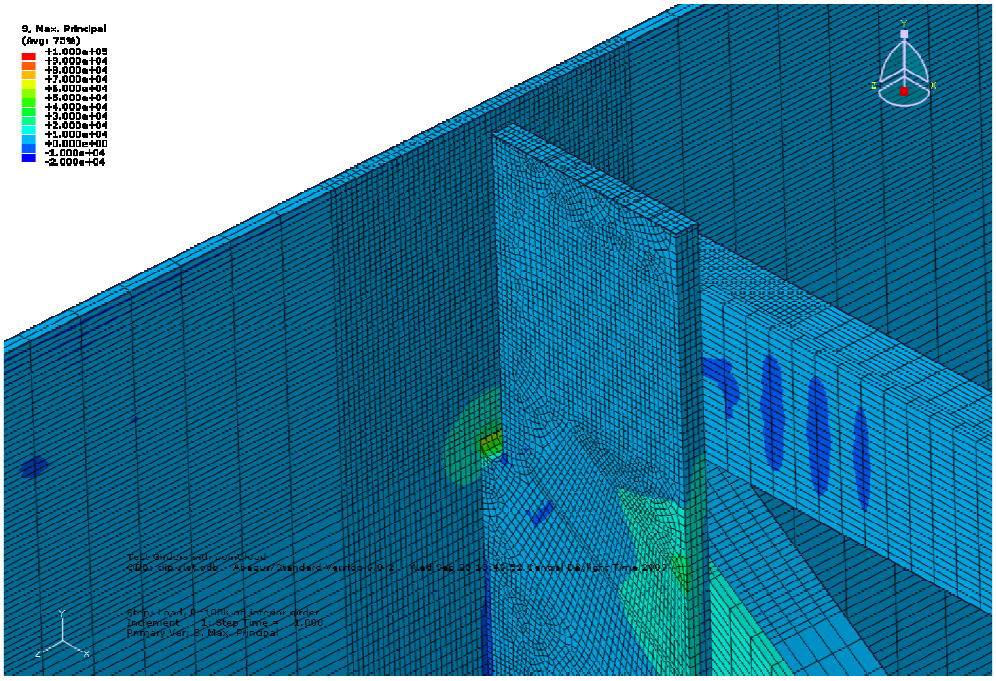

Figure 4-24 Slot repair fringe plot

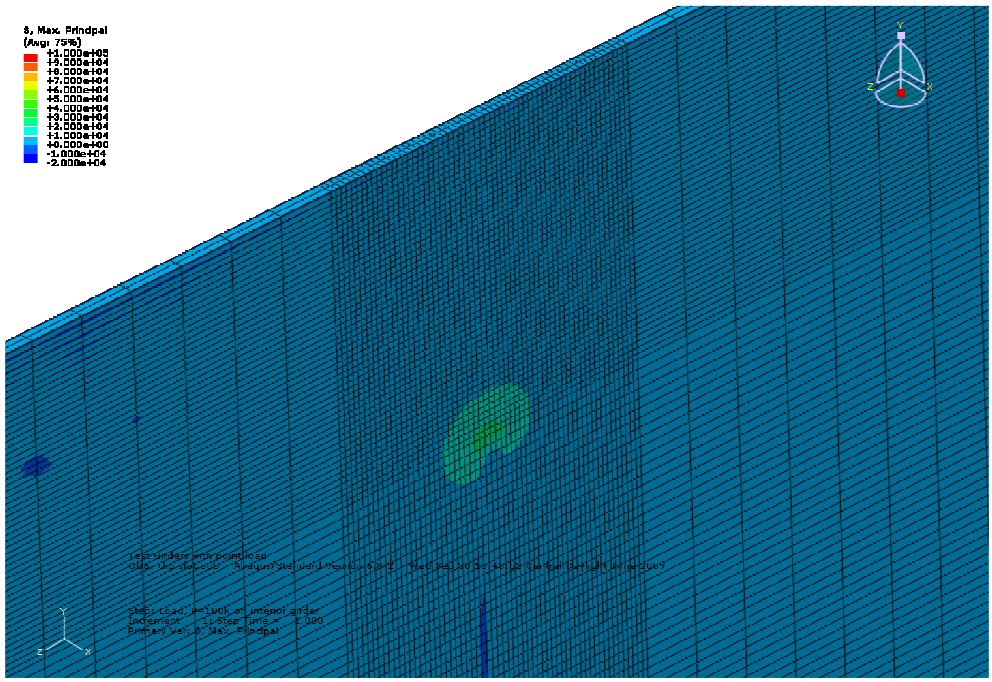

Figure 4-25 Slot repair fringe plot (connection plate removed)

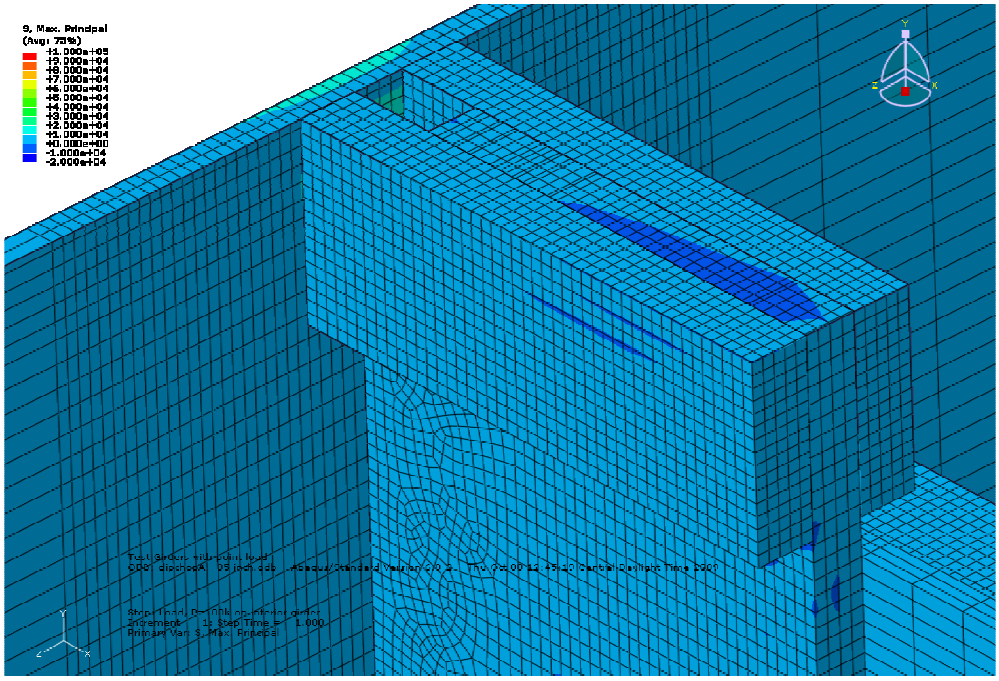

Figure 4-26 Chopped fiber A – 0.5 in. fringe plot

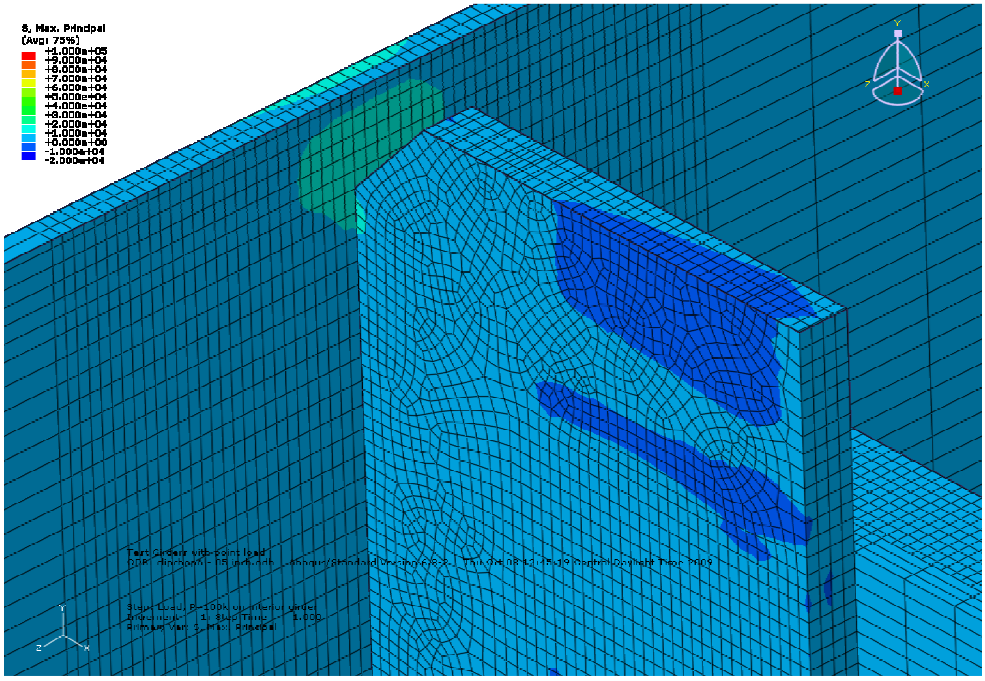

Figure 4-27 Chopped fiber A - 0.5 in fringe plot (composite removed)

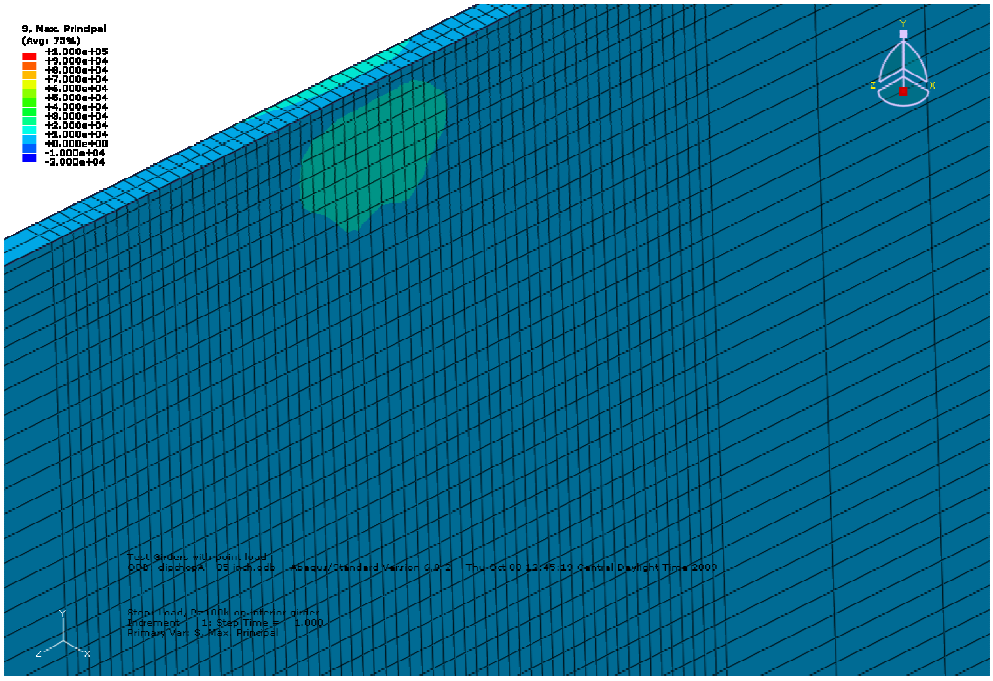

Figure 4-28 Chopped fiber A - 0.5 in fringe plot (composite and connection plate removed)

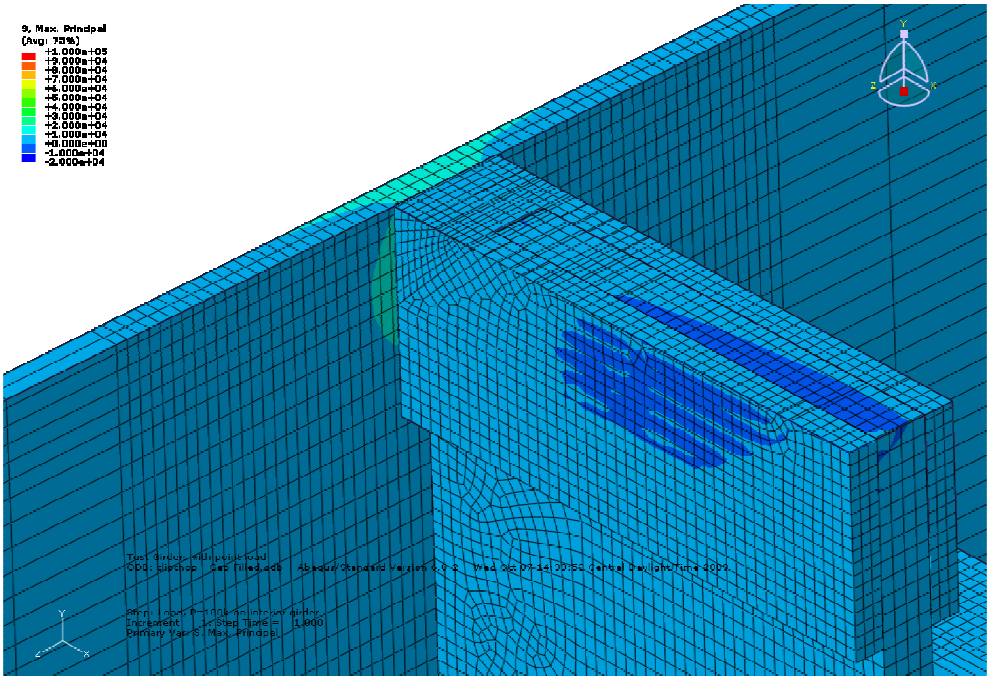

Figure 4-29 Chopped fiber A - 0.5 in. gap filled fringe plot

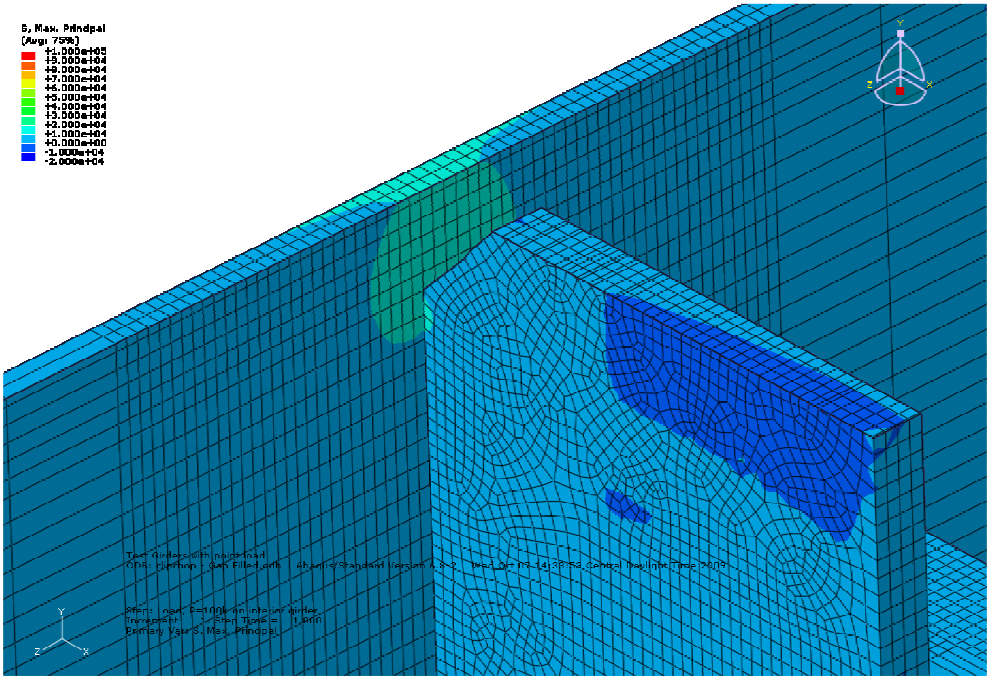

Figure 4-30 Chopped fiber A - 0.5 in. gap filled fringe plot (composite removed)

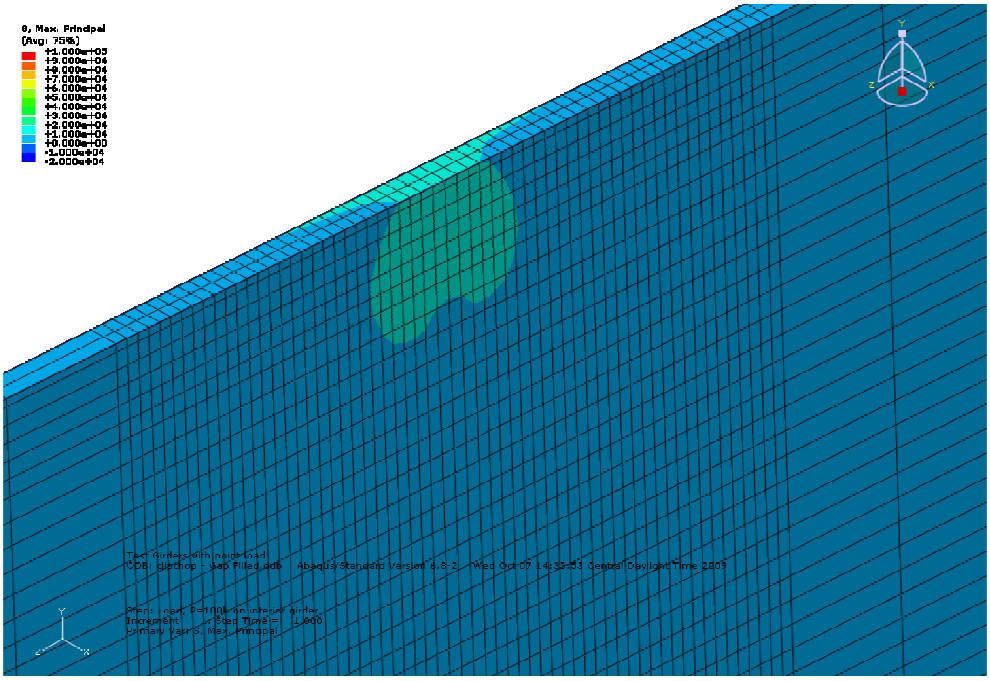

Figure 4-31 Chopped fiber A - 0.5 in gap filled fringe plot (composite and connection plate removed)

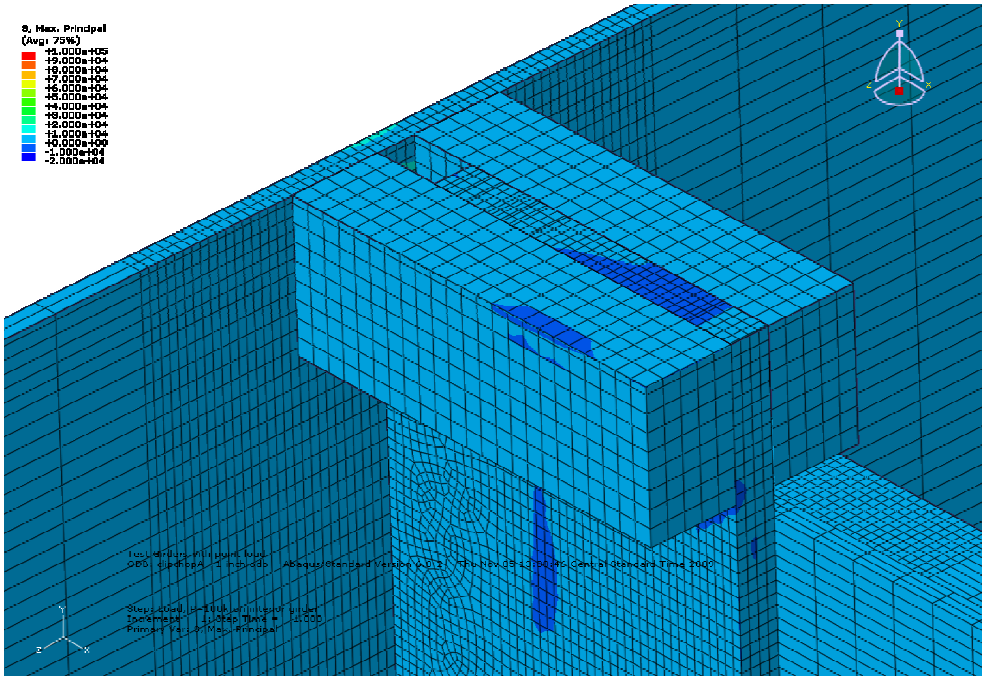

Figure 4-32 Chopped fiber A - 1.0 in. fringe plot

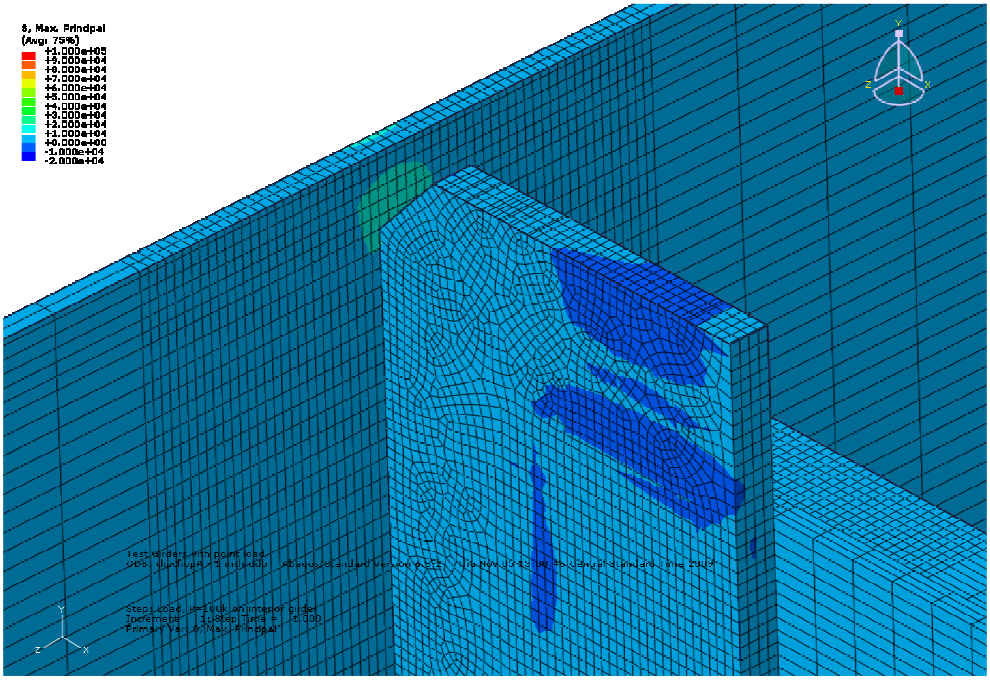

Figure 4-33 Chopped fiber A - 1.0 in. fringe plot (composite removed)

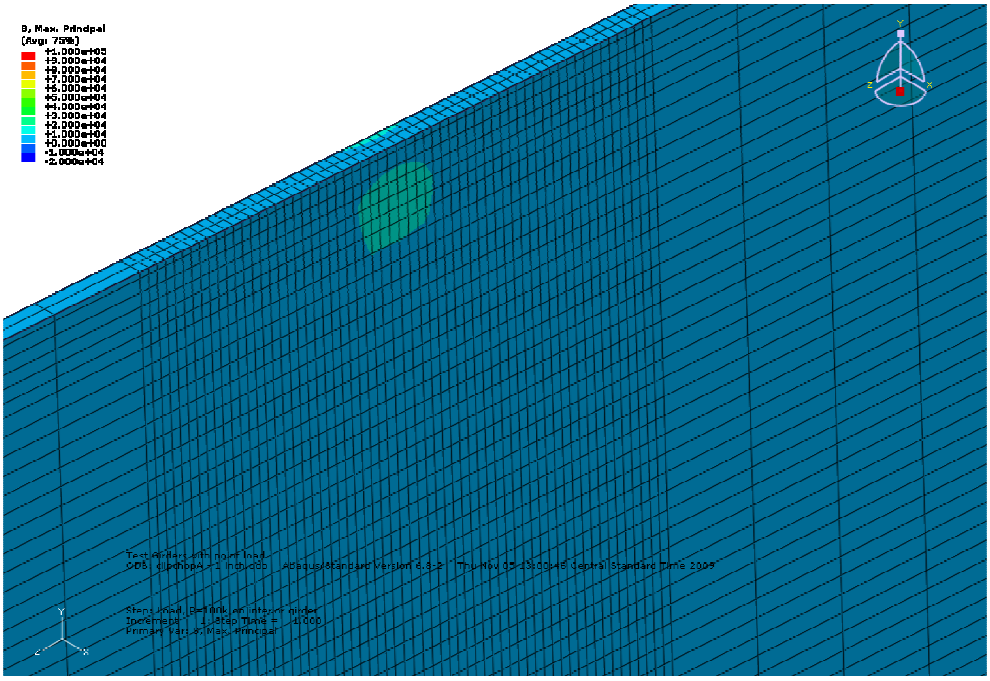

Figure 4-34 Chopped Fiber A - 1.0 in fringe plot (composite and connection plate removed)

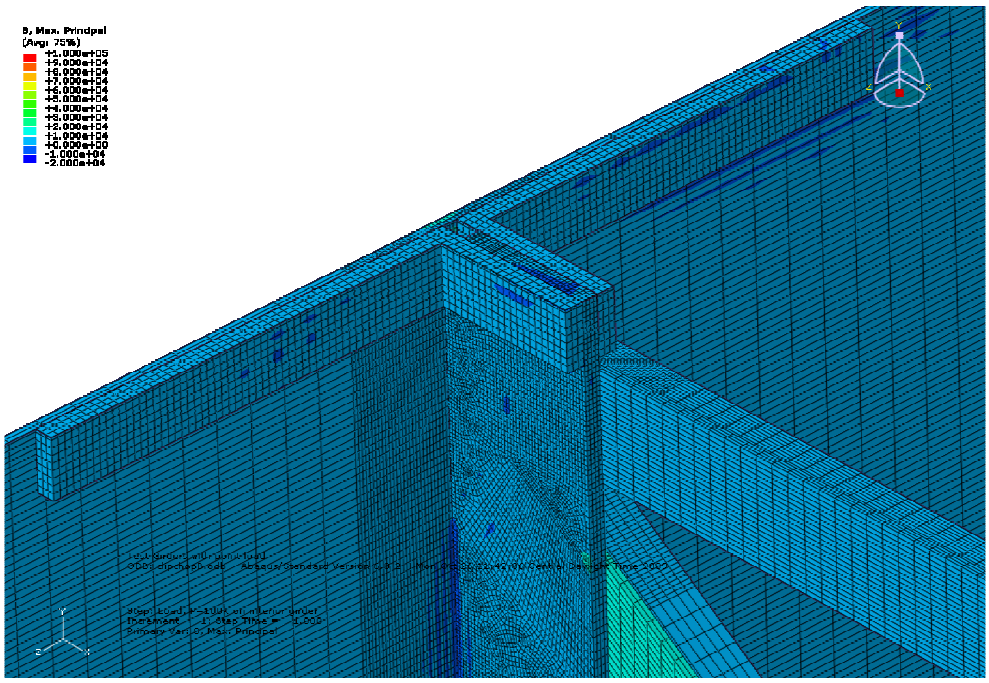

Figure 4-35 Chopped fiber B fringe plot

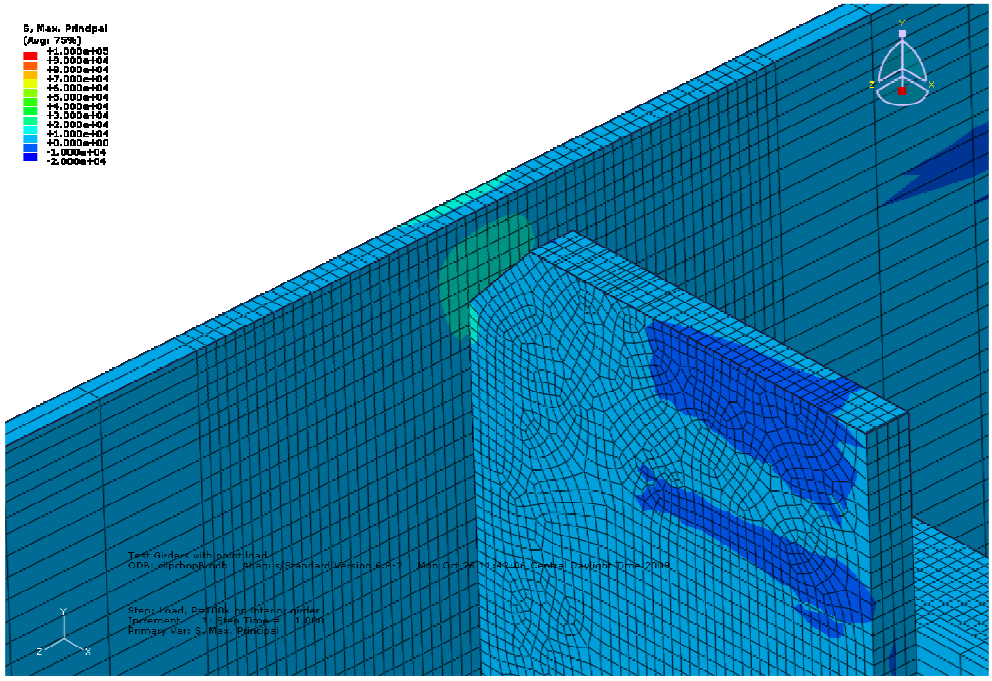

Figure 4-36 Chopped fiber B fringe plot (composite removed)

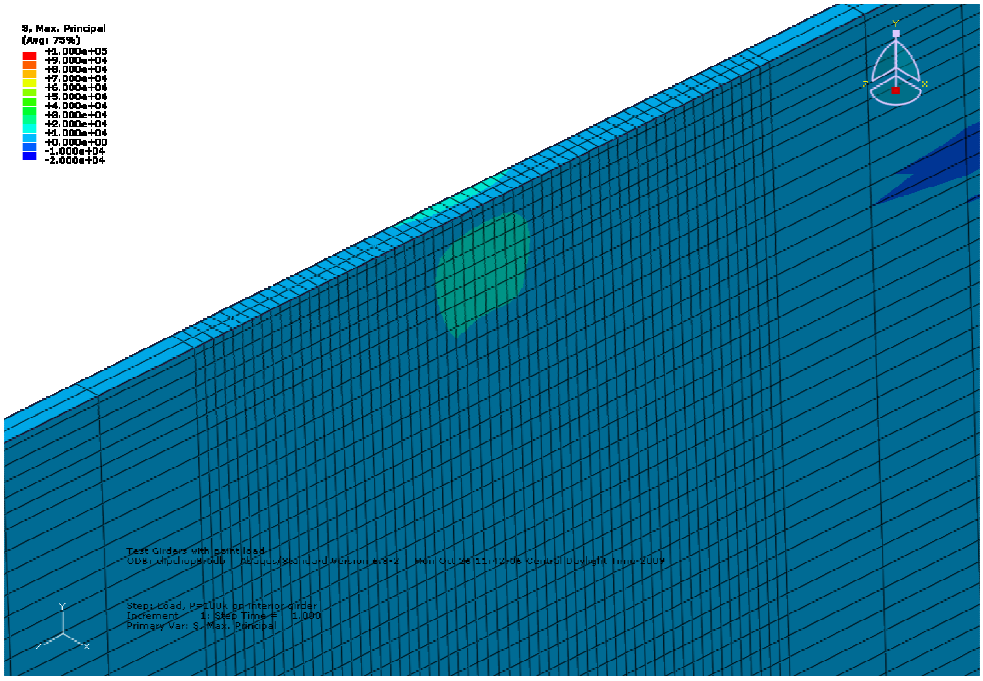

Figure 4-37 Chopped fiber B fringe plot (composite and connection plate removed)

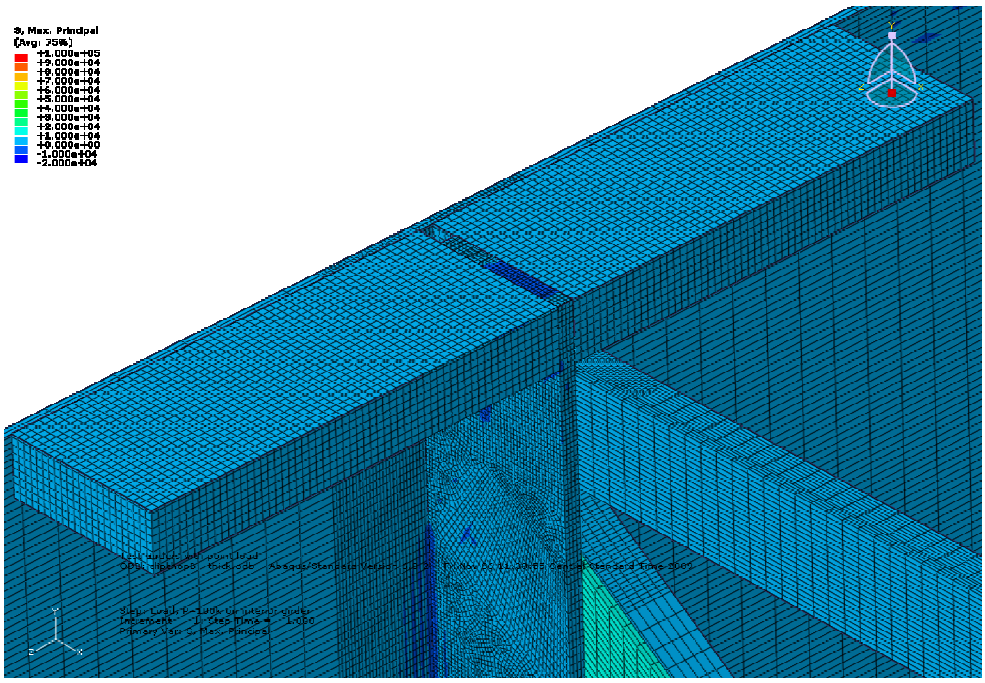

Figure 4-38 Chopped fiber B - thick fringe plot

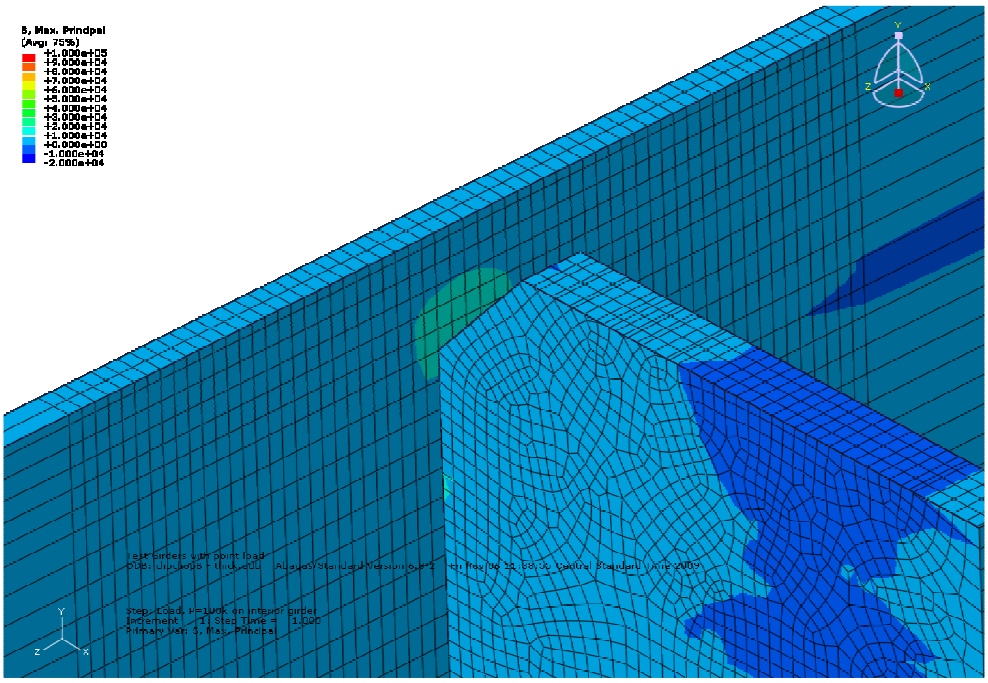

Figure 4-39 Chopped fiber B - thick fringe plot (composite removed)

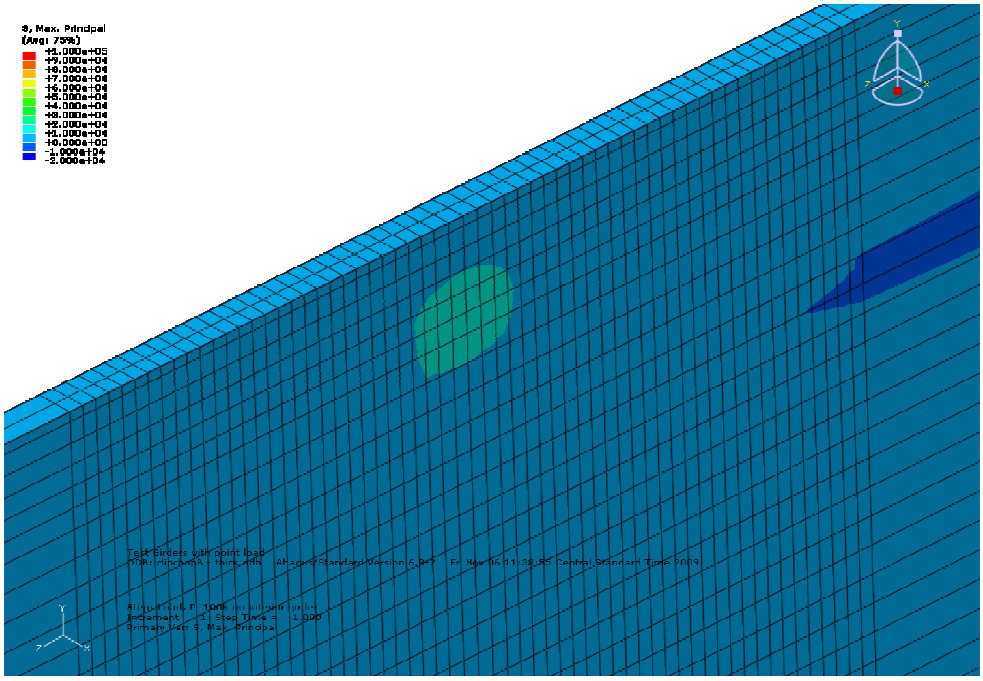

Figure 4-40 Chopped fiber B - thick fringe plot (composite and connection plate removed)

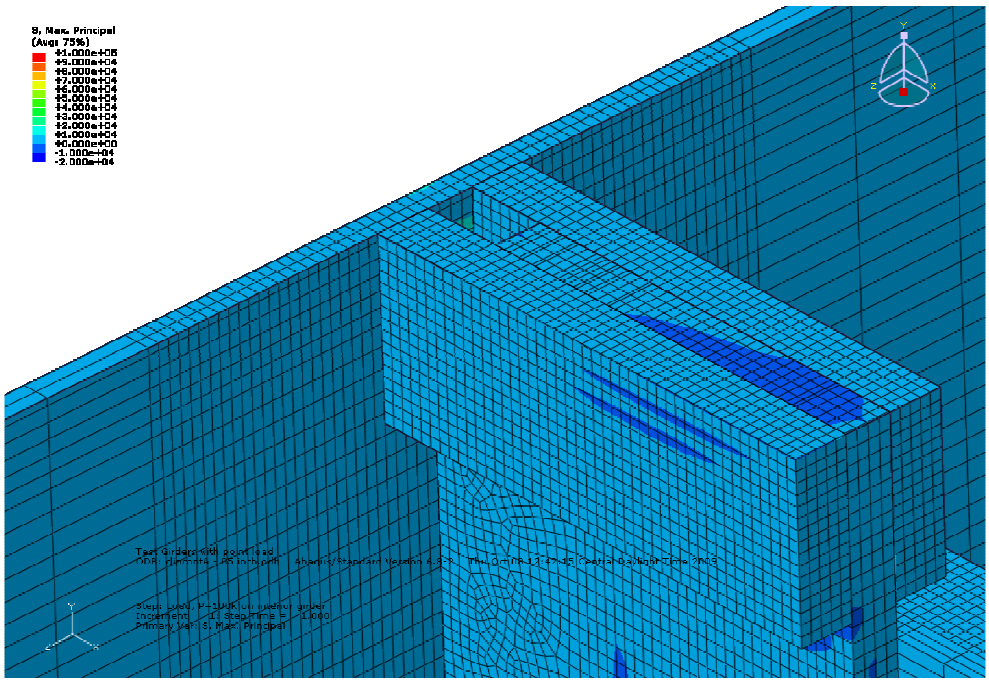

Figure 4-41 Continuous fiber A - 0.5 in. fringe plot

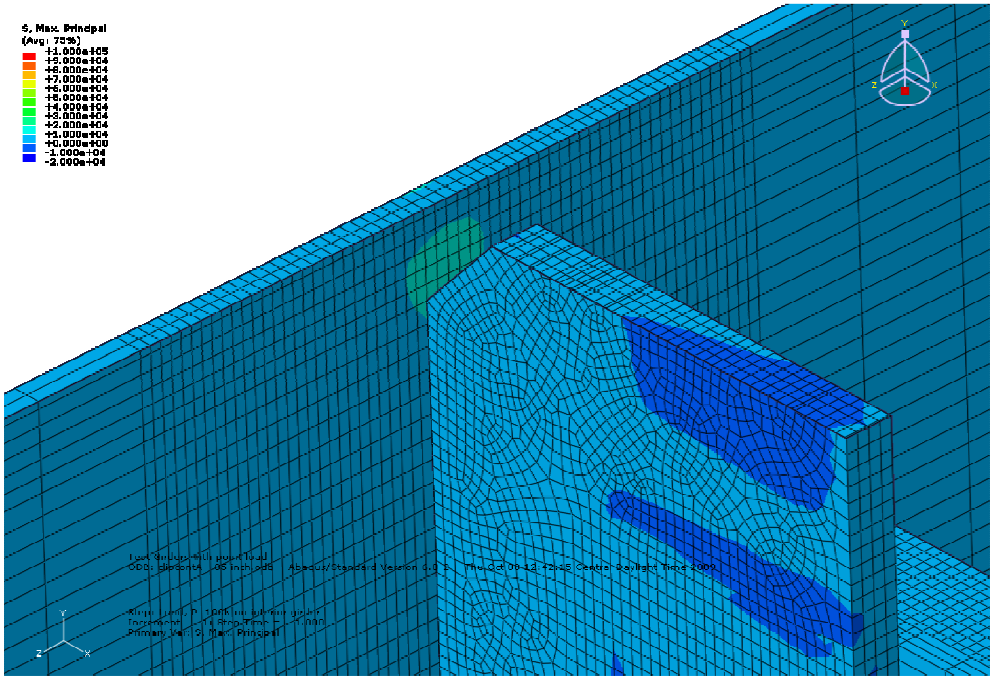

Figure 4-42 Continuous fiber A - 0.5 in. fringe plot (composite removed)

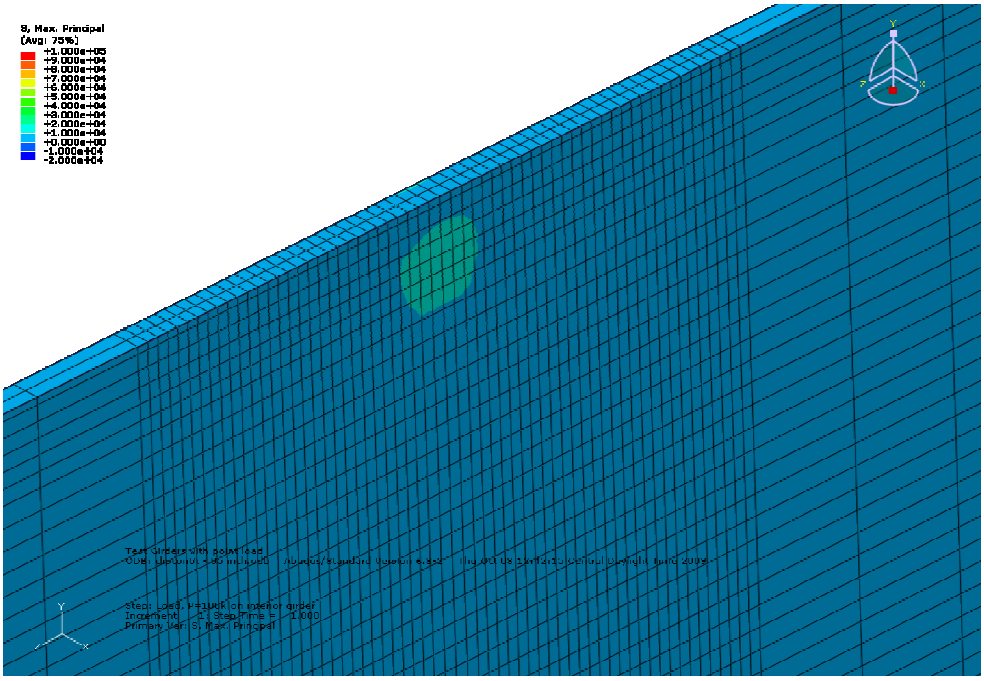

Figure 4-43 Continuous fiber A - 0.5 in. fringe plot (composite and connection plate removed)

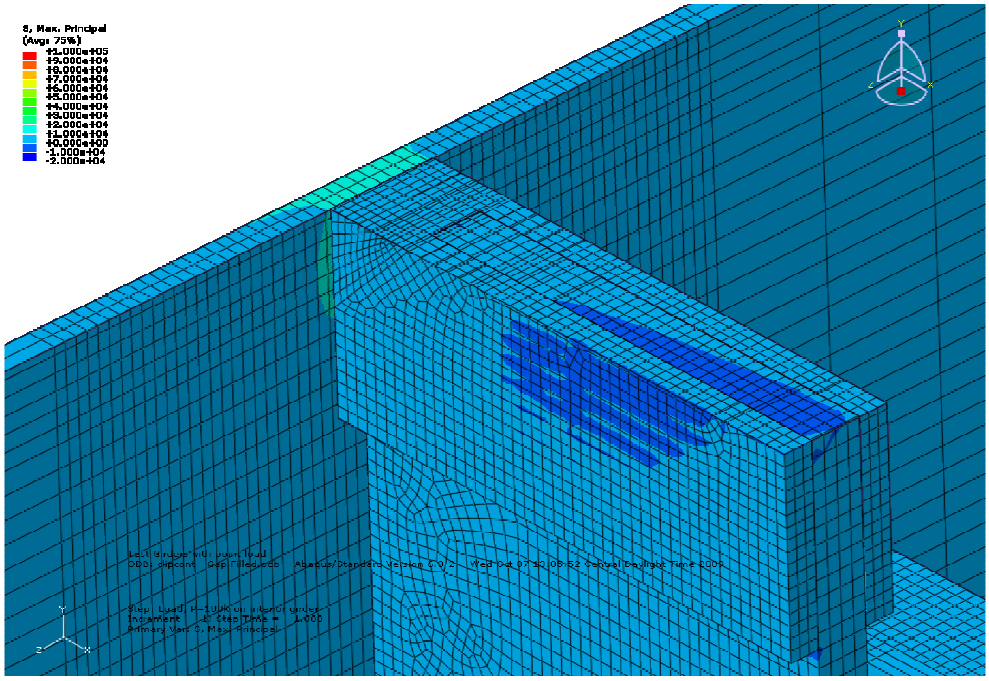

Figure 4-44 Continuous fiber A - 0.5 in gap filled fringe plot

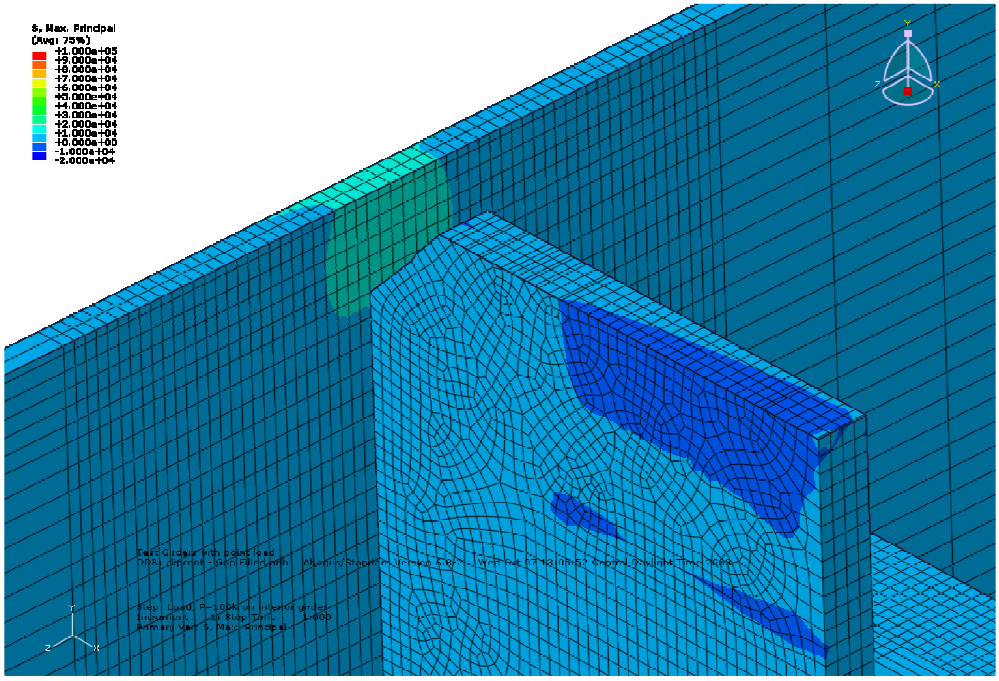

Figure 4-45 Continuous fiber A - 0.5 in gap filled fringe plot (composite removed)

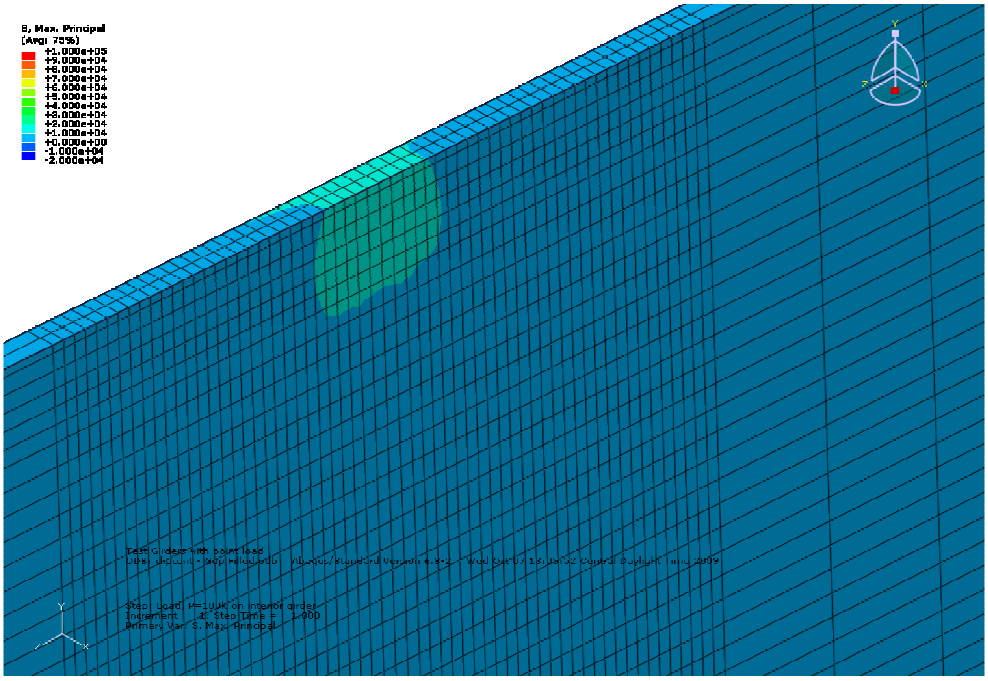

Figure 4-46 Continuous fiber A - 0.5 in gap filled fringe plot (composite and connection plate removed)

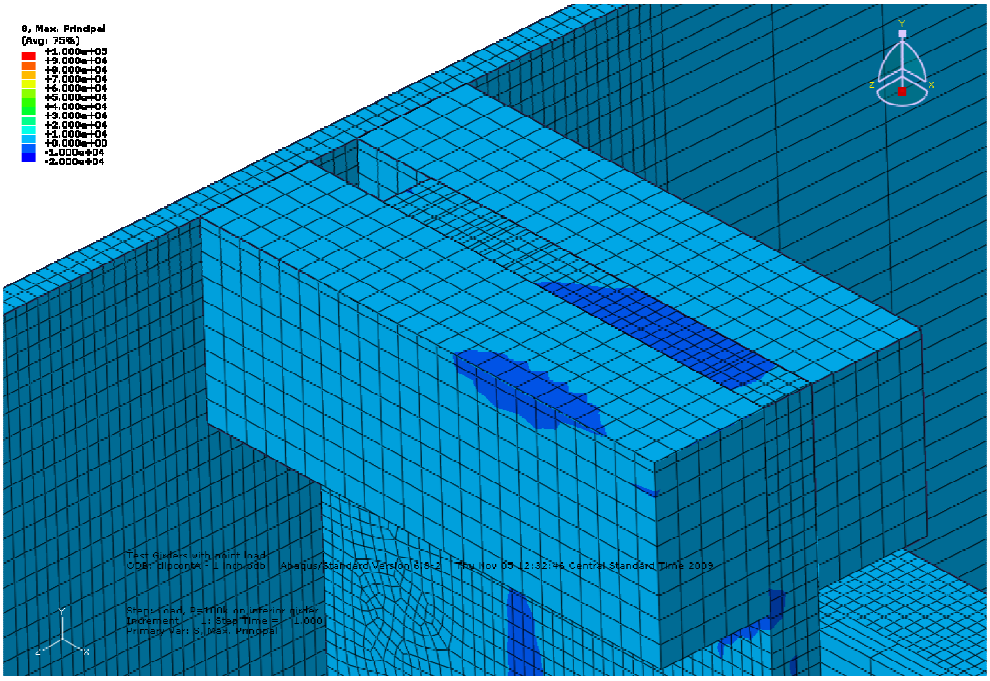

Figure 4-47 Continuous fiber A - 1.0 in. fringe plot

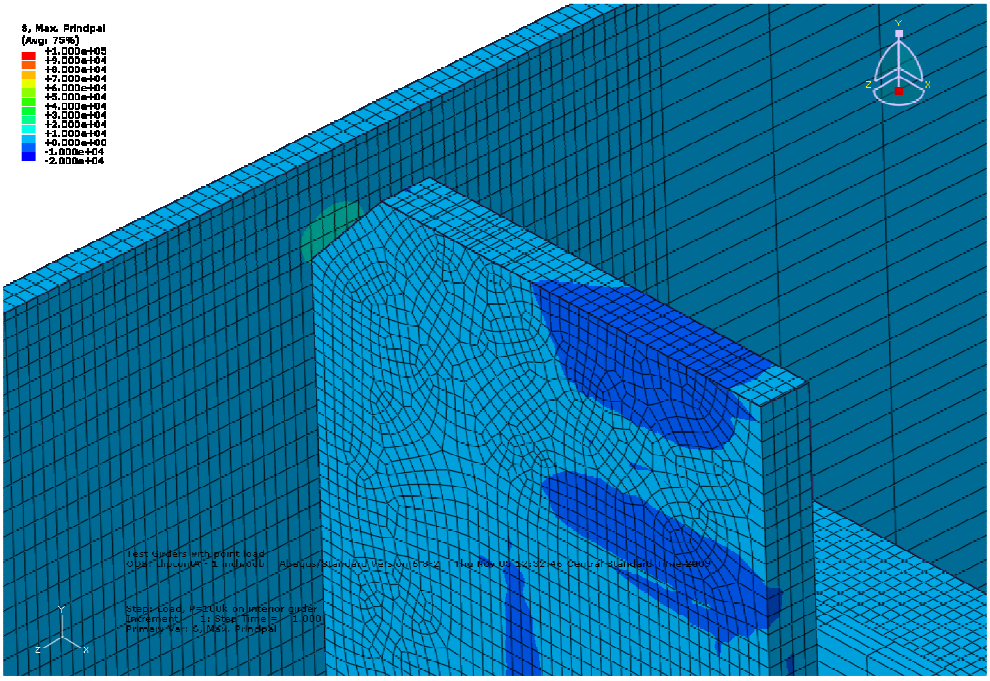

Figure 4-48 Continuous fiber A - 1.0 in. fringe plot (composite removed)

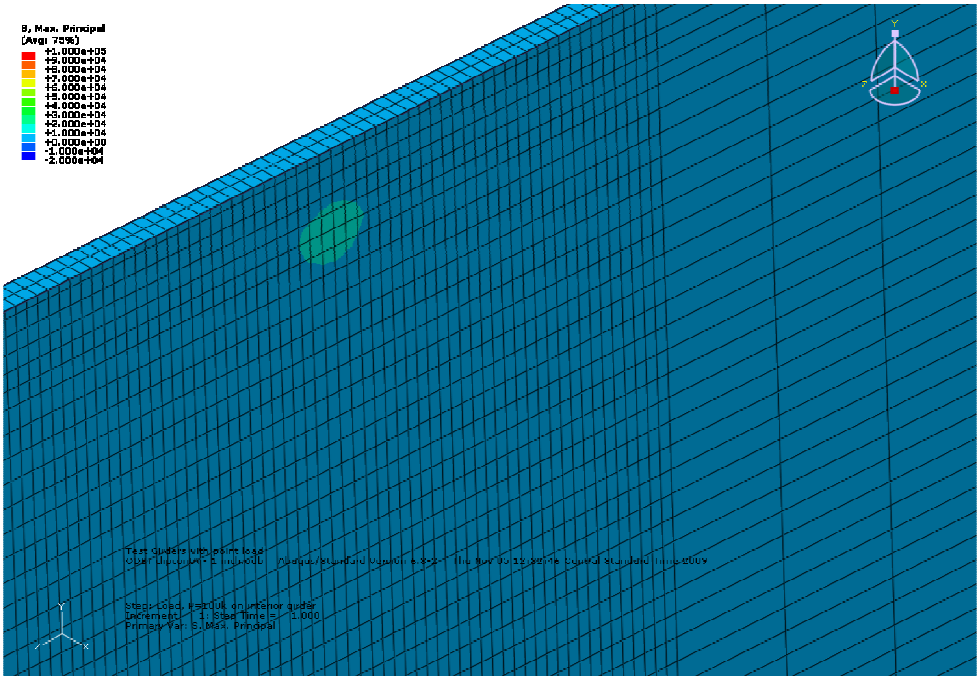

Figure 4-49 Continuous fiber A - 1.0 in. fringe plot (composite and connection plate removed)

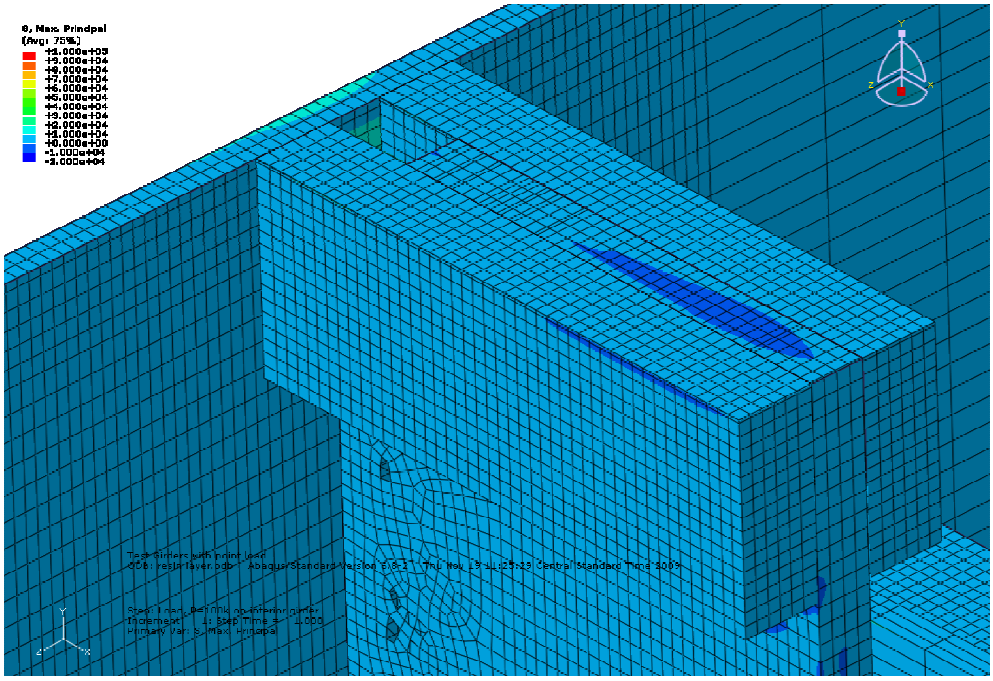

Figure 4-50 Continuous fiber A - 0.5 in w/ resin fringe plot

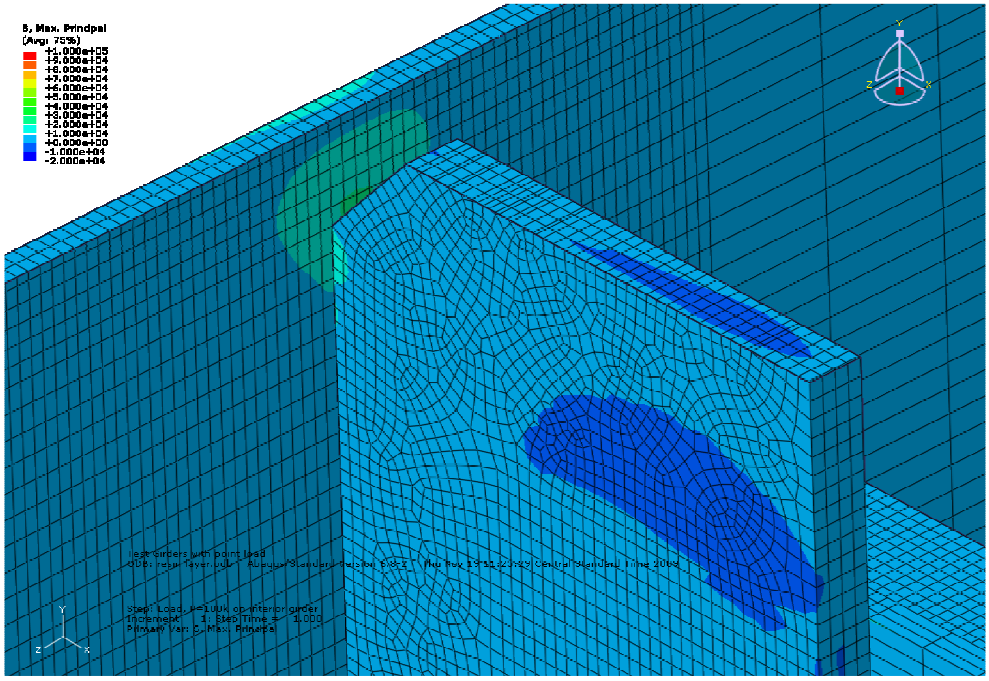

Figure 4-51 Continuous fiber A - 0.5 in. w/ resin fringe plot (composite removed)

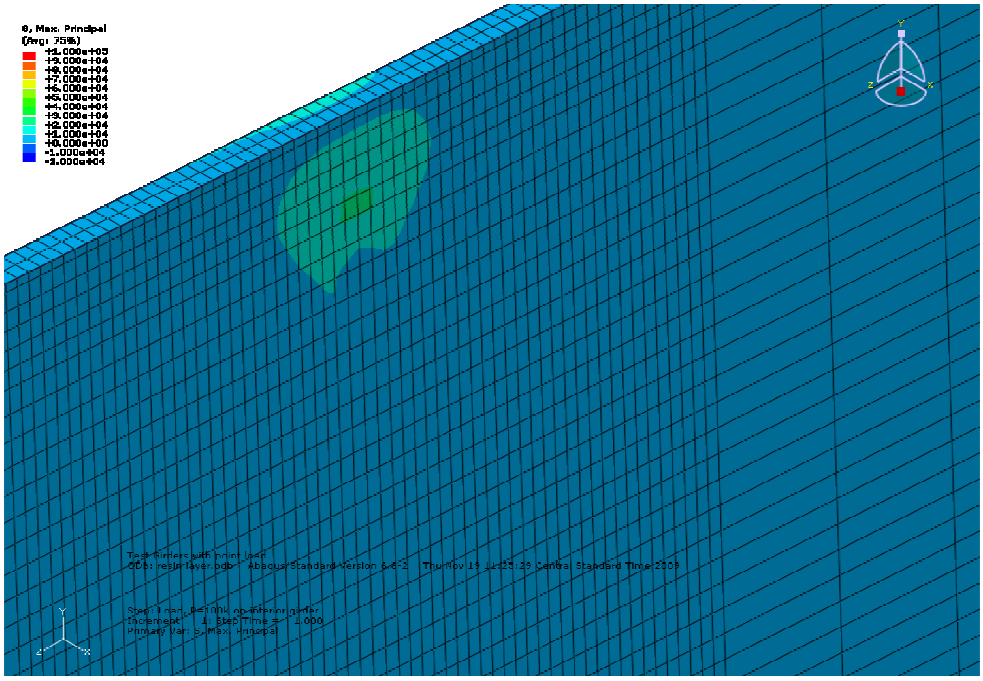

Figure 4-52 Continuous fiber A - 0.5 in. w/ resin layer fringe plot (composite and connection plate removed)

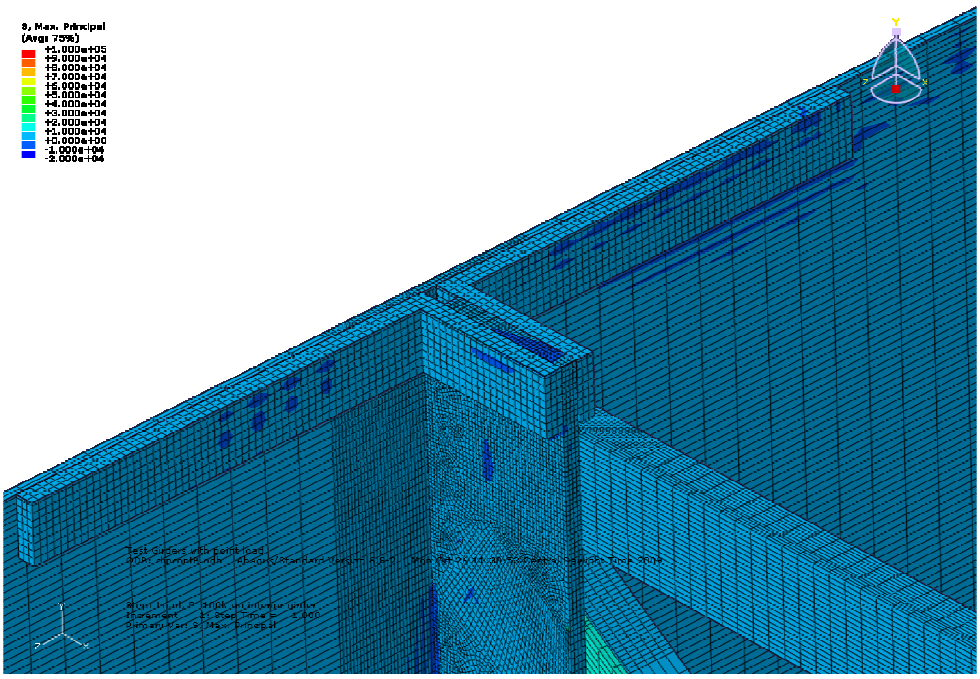

Figure 4-53 Continuous fiber B fringe plot

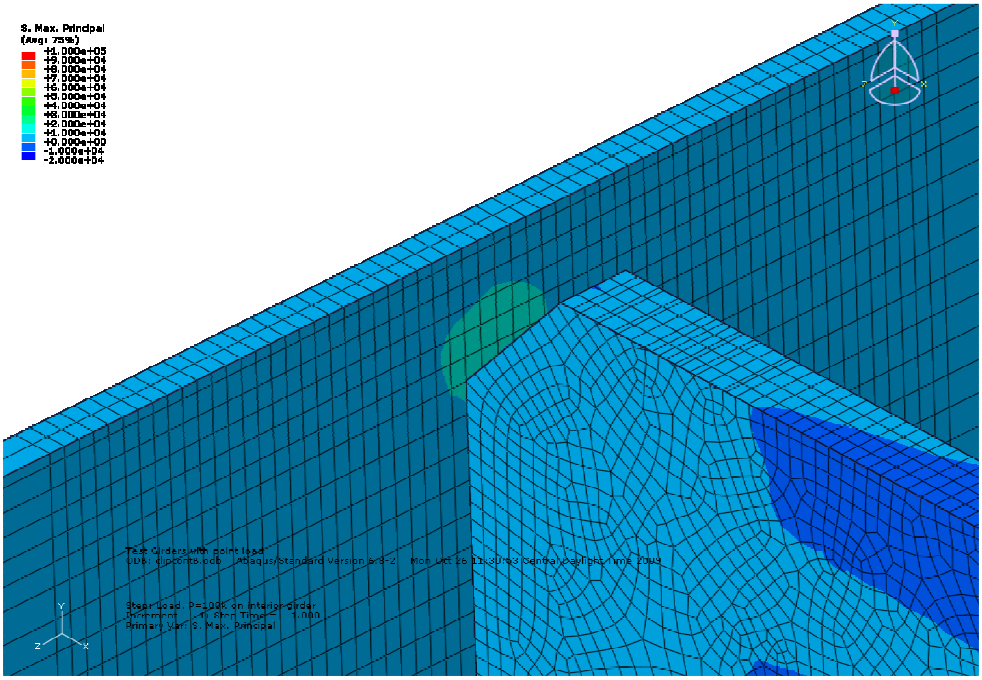

Figure 4-54 Continuous fiber B fringe plot (composite removed)

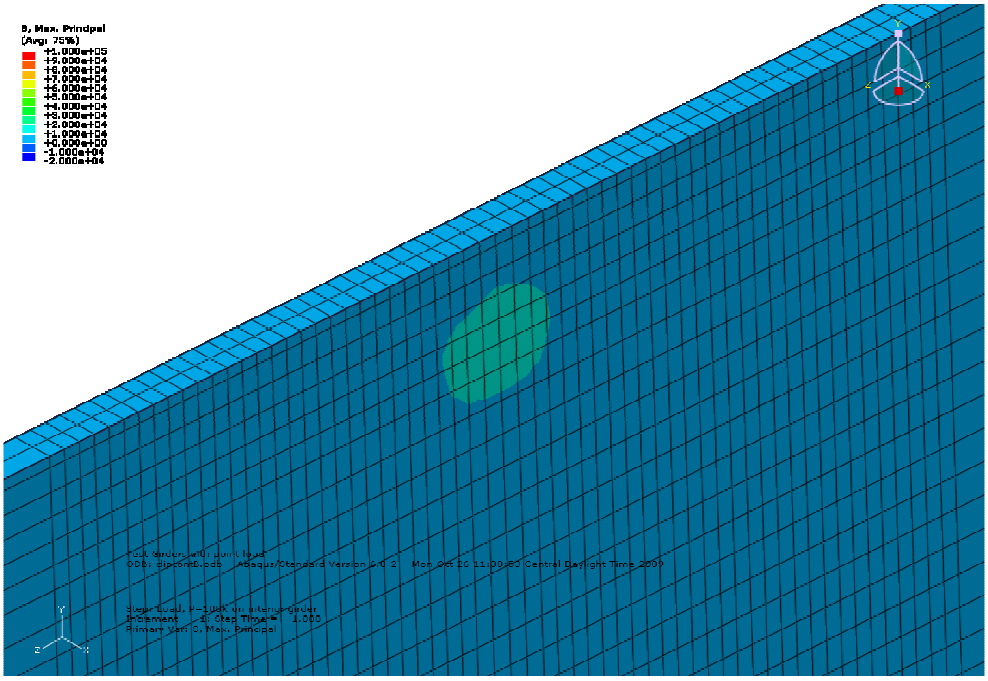

Figure 4-55 Continuous fiber B fringe plot (composite and connection plate removed)

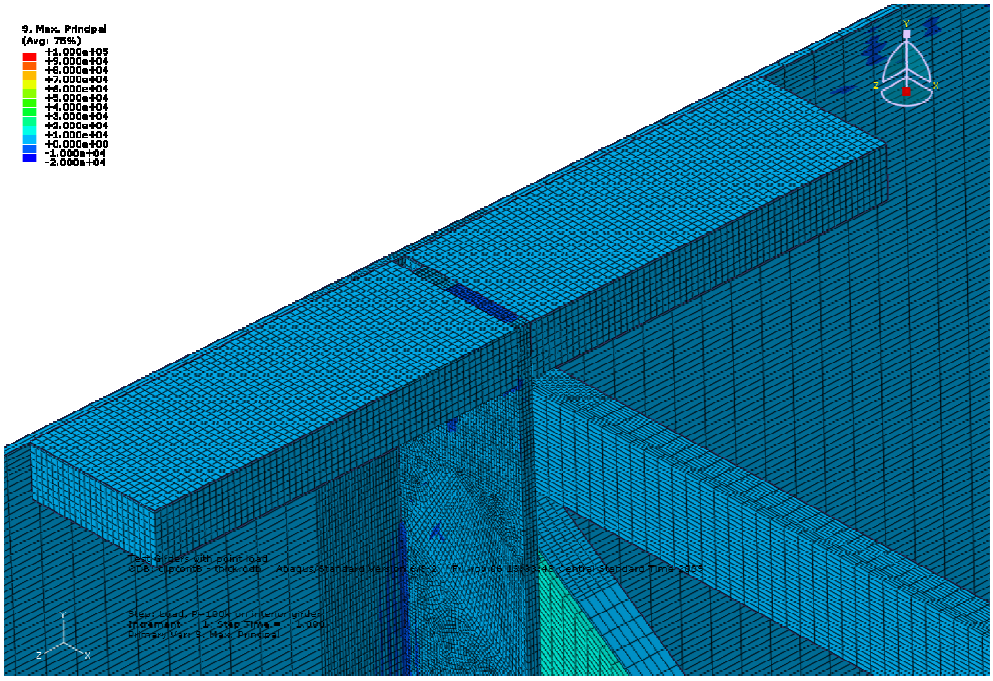

Figure 4-56 Continuous fiber B - thick fringe plot

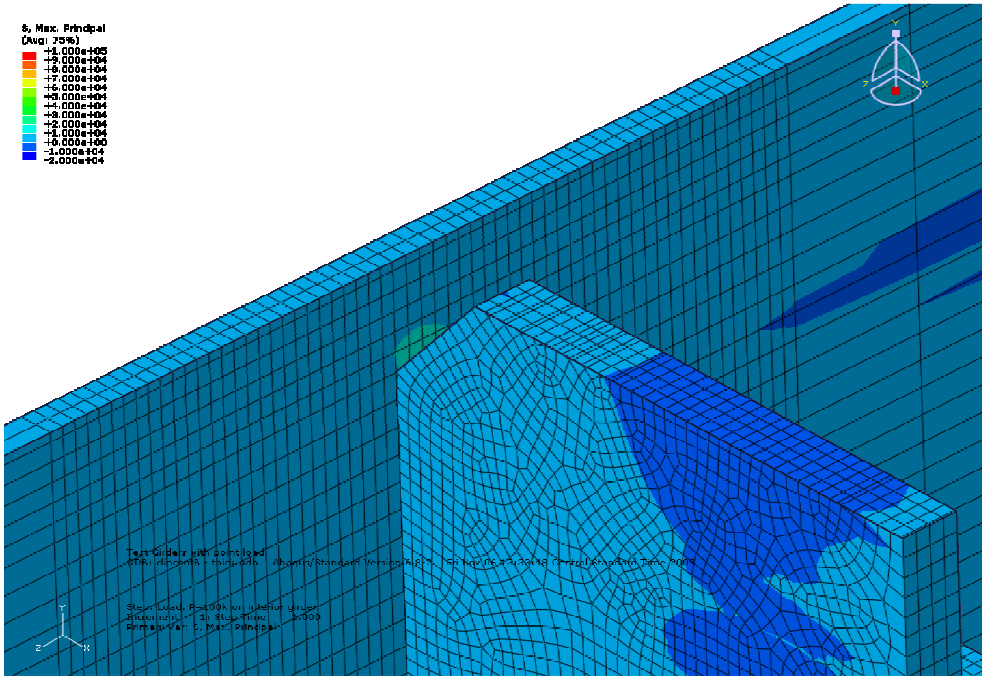

Figure 4-57 Continuous fiber B - thick fringe plot (composite removed)

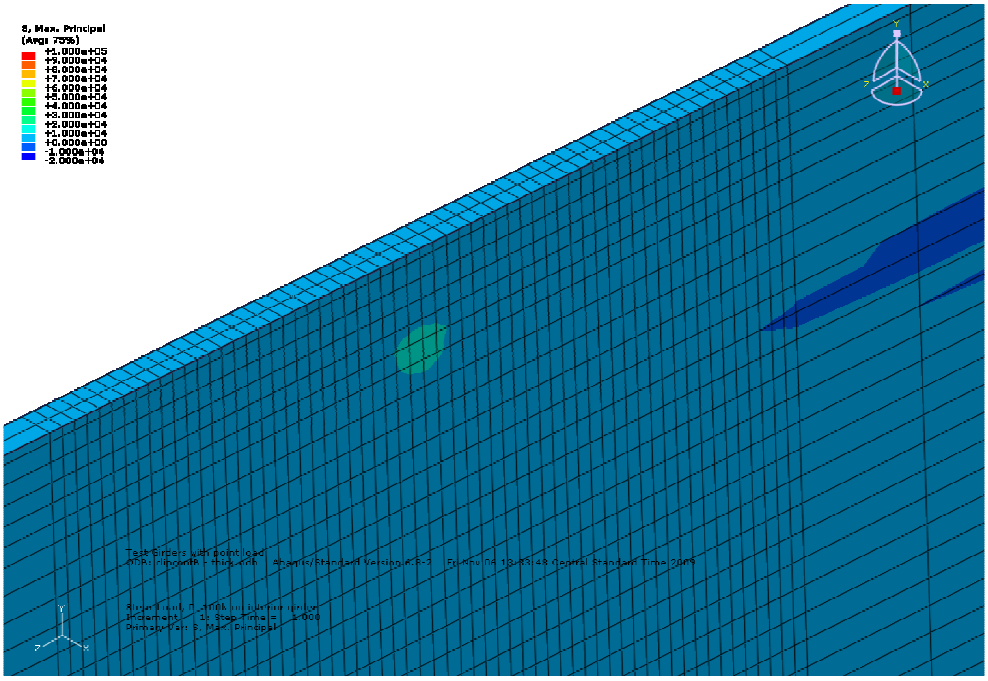

Figure 4-58 Continuous fiber B - thick fringe plot (composite and connection plate removed)

It is shown in the preceding figures that the stress demand in the retrofitted details was significantly reduced. The positive attachment (connection plate fixed to the top flange) and slot repair reduce the stress demand significantly enough to be considered an effective analytical retrofit. Retrofitting measures using CFRP overlays also reduce the stress demand enough to be considered an effective analytical retrofit.

4.3.7 DEFORMED SHAPES

Reducing the amount of deformation in the web-gap is an important factor in reducing the stress demand in the web-gap. Figure 4-59 shows the deformed shape of the three girder system described in Chapter 2. The center girder has the

most downward deflection, creating differential deflections between the center girder and exterior girders. Figure 4-60 through Figure 4-73 show the deformed shapes of non-retrofitted and retrofitted details on one of the exterior girders (the deformations are similar on both exterior girders for the same model). All of the deformed shapes in the following figures are scaled by a factor of 50. Because of this, some figures of the deformed shapes of web-gaps show the connection plate intersecting the top flange. The connection plates do not intersect the top flange if the deformations are not scaled by a factor of 50.

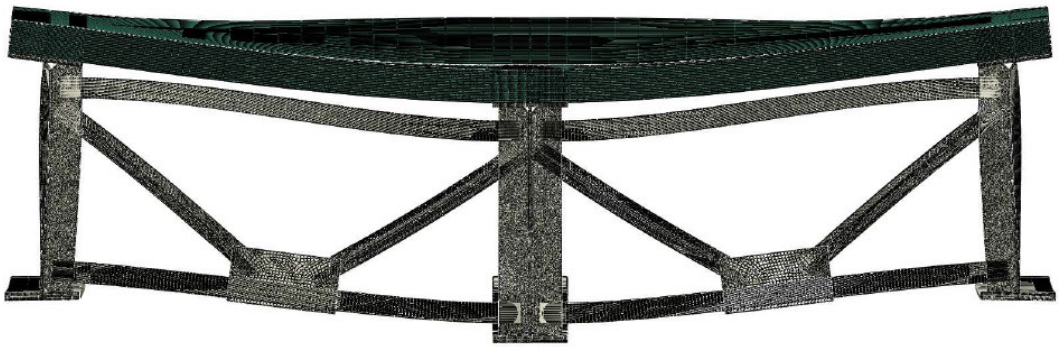

Figure 4-59 Deformed shape at midspan of non-retrofitted detail

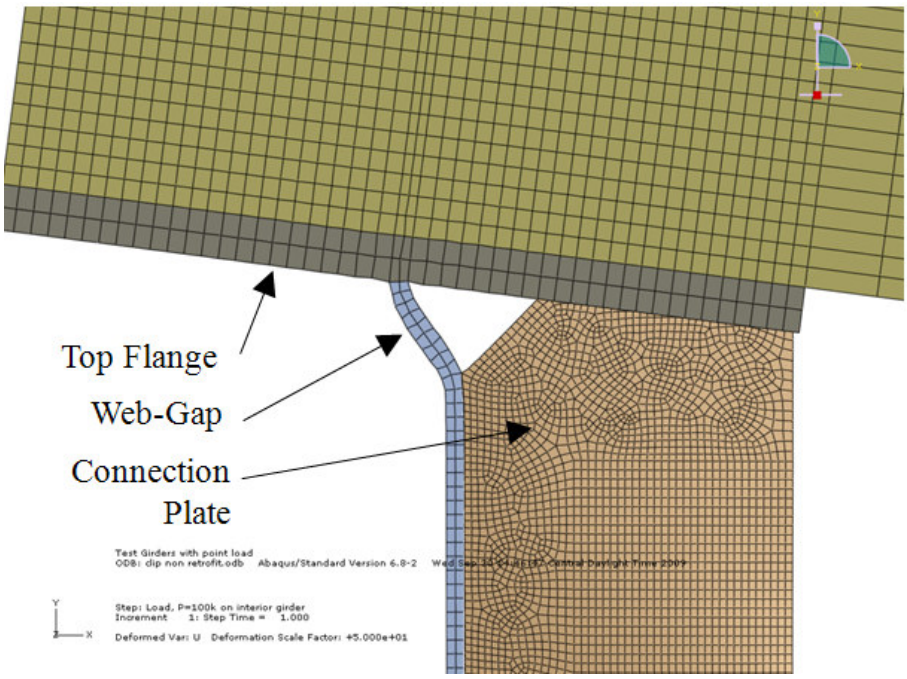

Figure 4-60 Deformed web-gap of non-retrofitted – clip

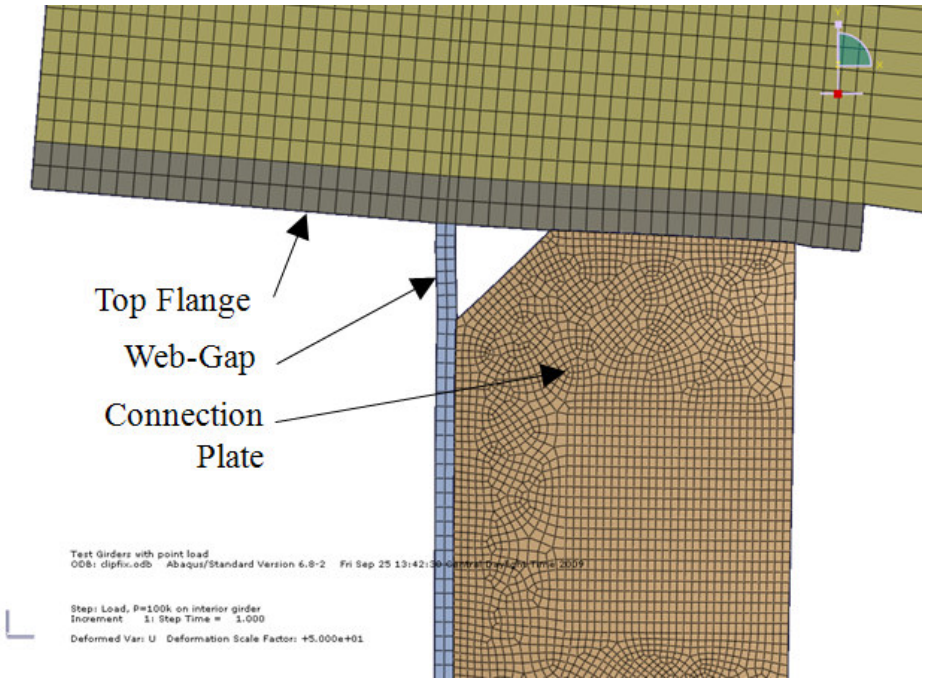

Figure 4-61 Deformed web-gap of fixed repair

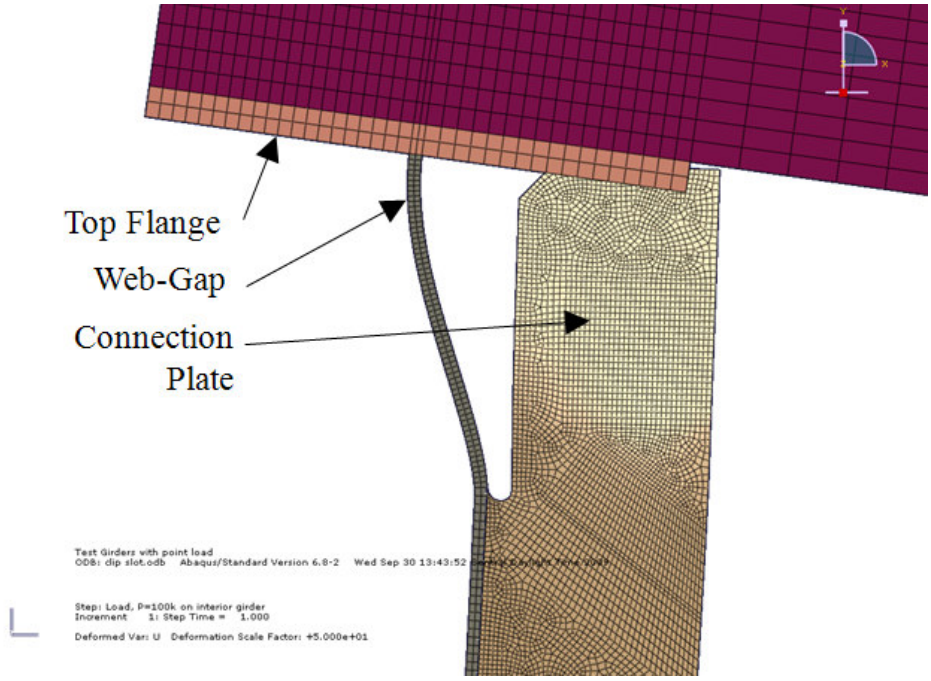

Figure 4-62 Deformed web-gap of slot repair

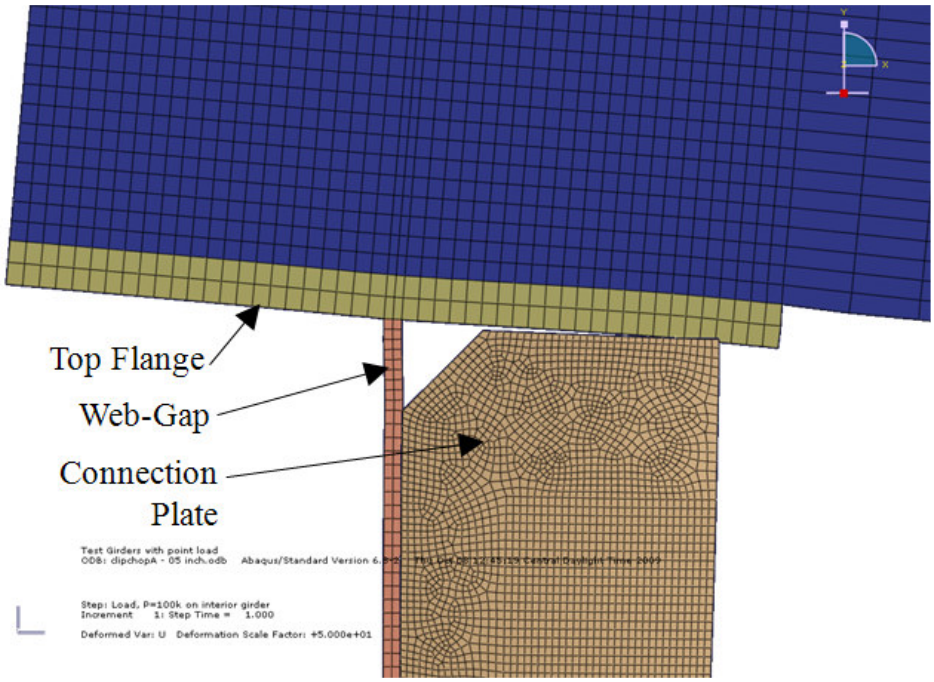

Figure 4-63 Deformed web-gap of chopped fiber A - 0.5 in. (composite not visible)

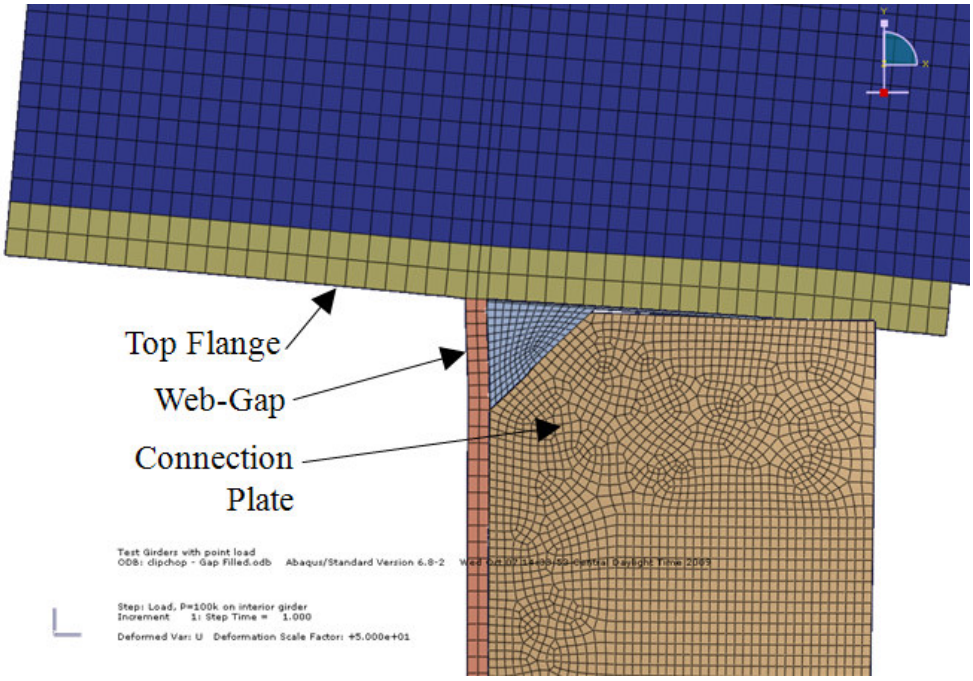

Figure 4-64 Deformed web-gap of chopped fiber A - 0.5 in gap filled

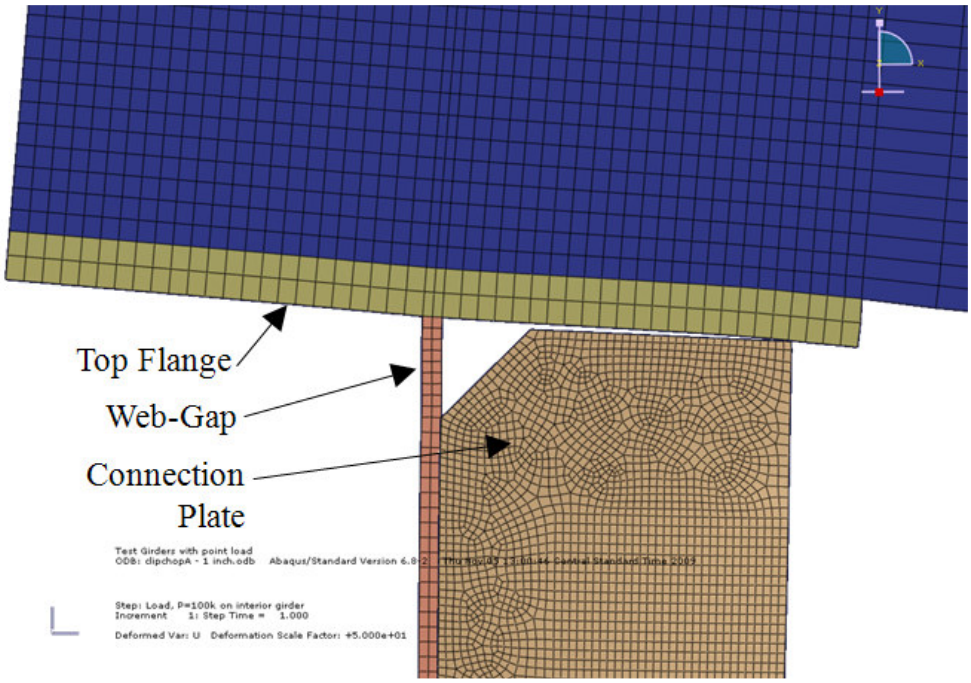

Figure 4-65 Deformed web-gap of chopped fiber A - 1.0 in. (composite not visible)

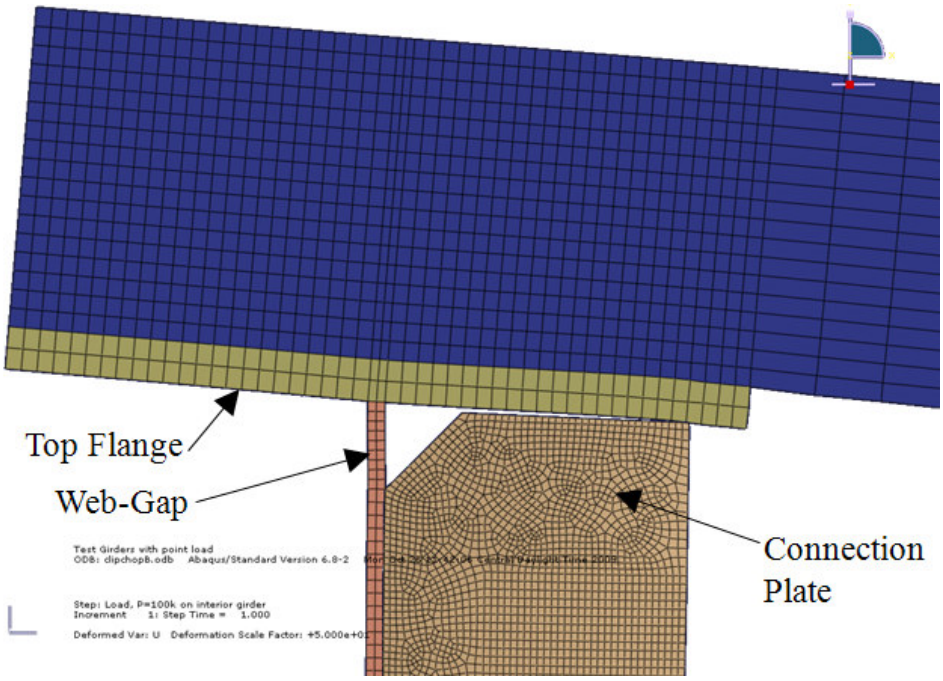

Figure 4-66 Deformed web-gap of chopped fiber B (composite not visible)

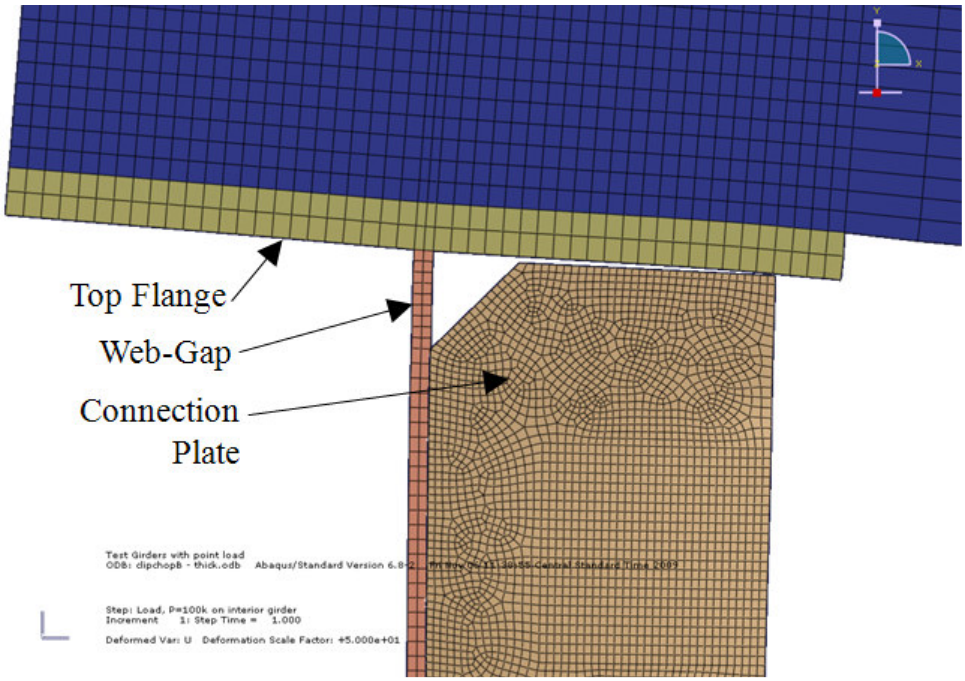

Figure 4-67 Deformed web-gap of chopped fiber B – thick (composite not visible)

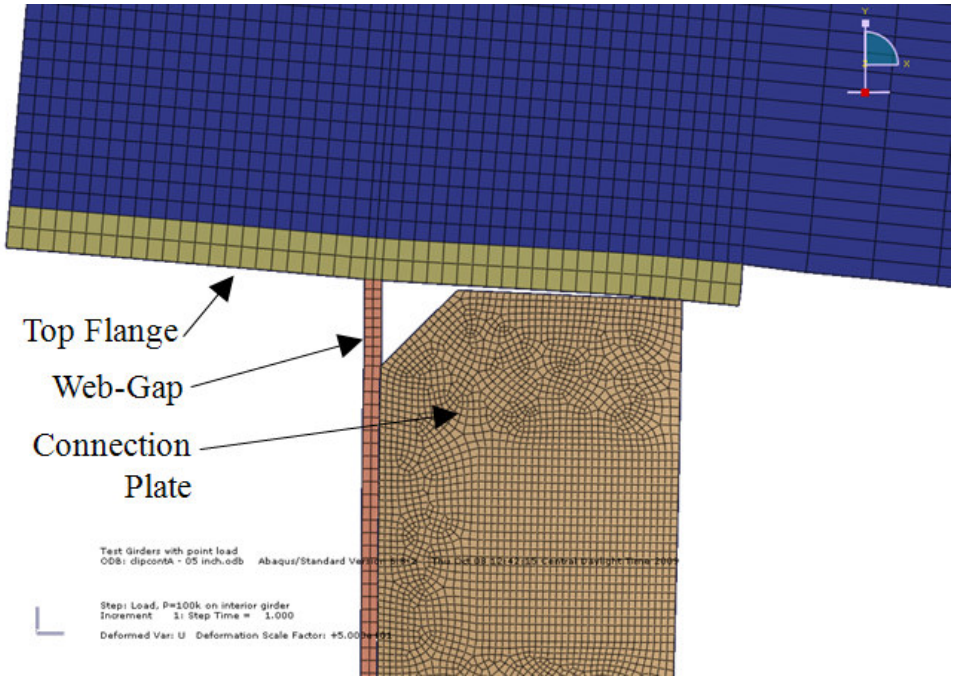

Figure 4-68 Deformed web-gap of continuous fiber A – 0.5 in. (composite not visible)

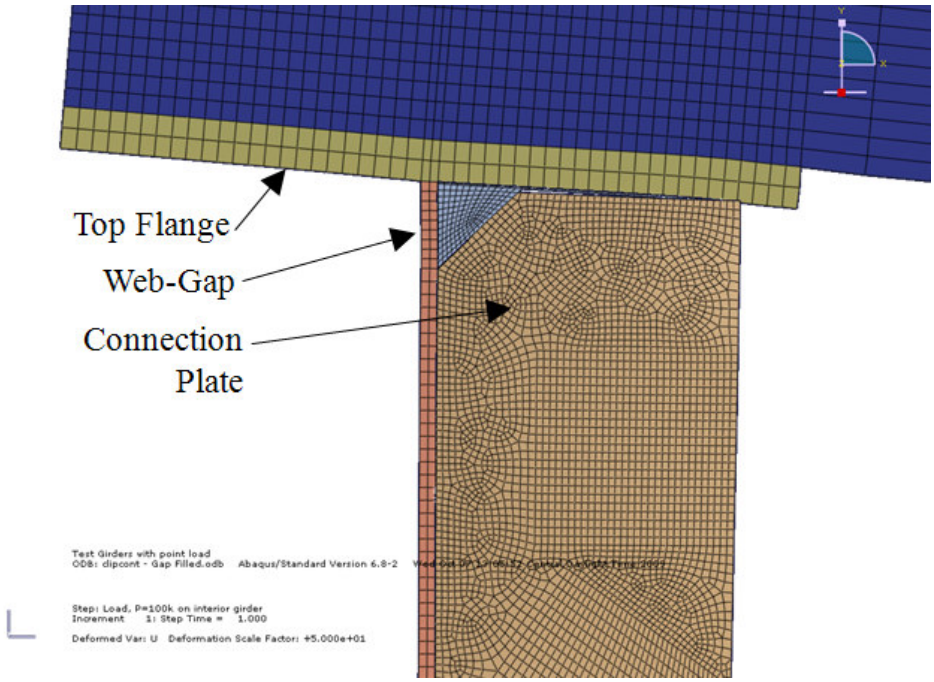

Figure 4-69 Deformed web-gap of continuous fiber A - 0.5 in. gap filled

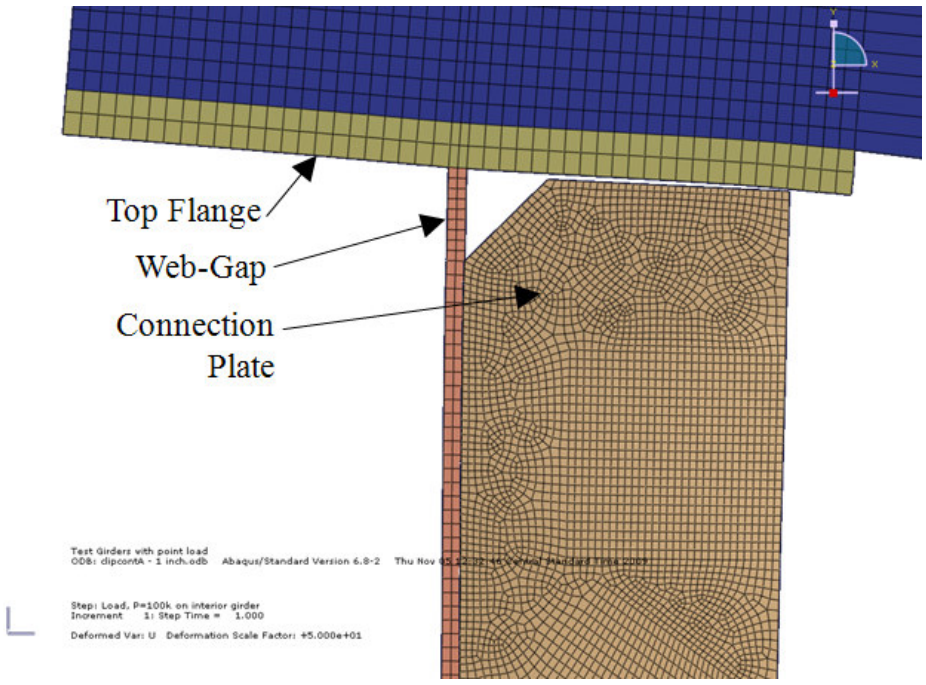

Figure 4-70 Deformed web-gap of continuous fiber A - 1.0 in. (composite not visible)

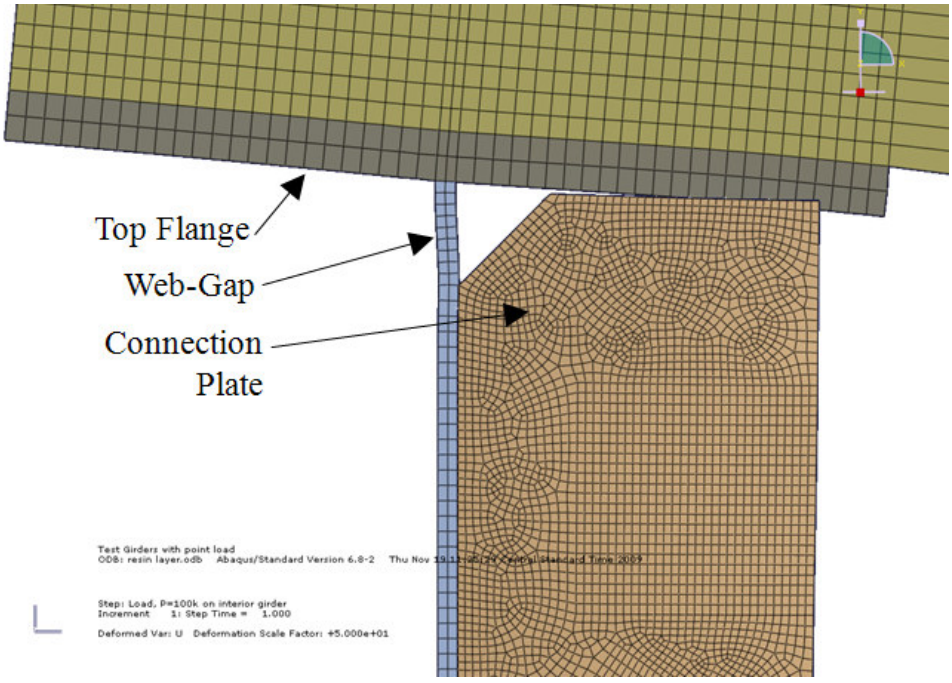

Figure 4-71 Deformed web-gap of continuous fiber A - 0.5 in with resin (composite not visible)

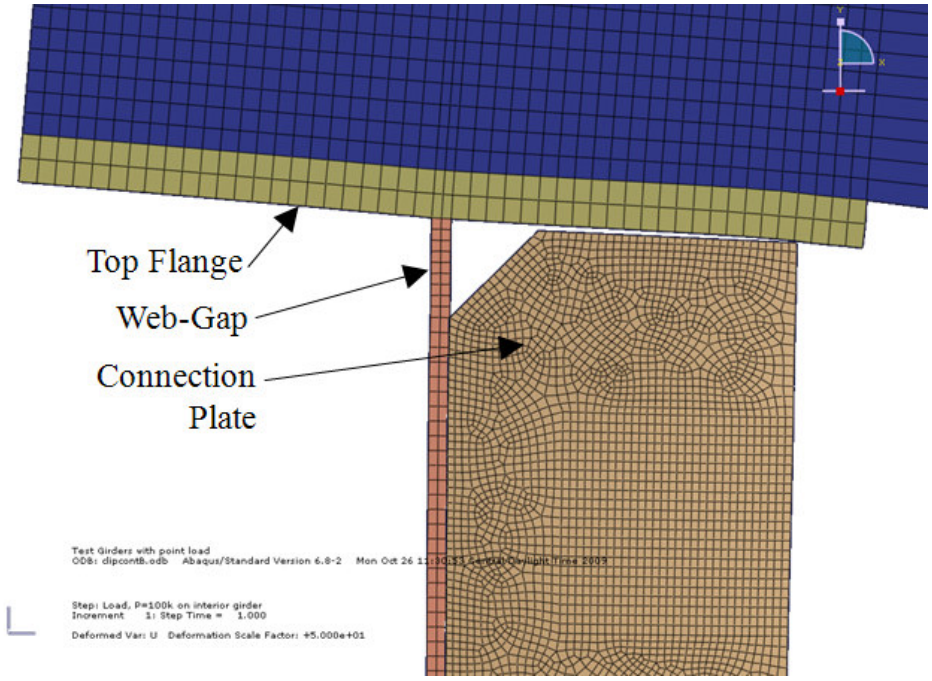

Figure 4-72 Deformed web-gap of continuous fiber B (composite not visible)

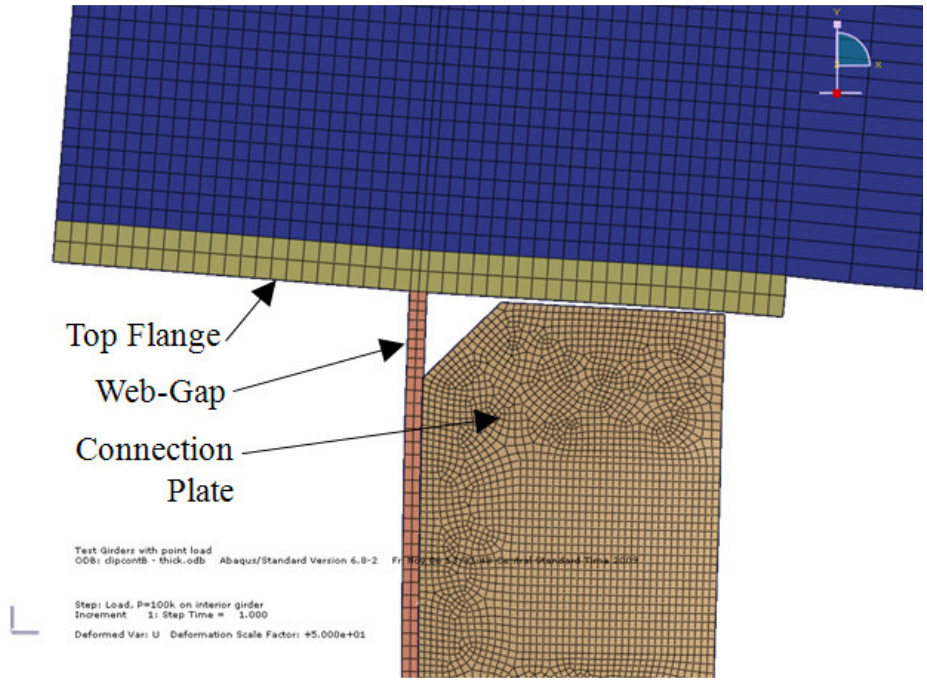

Figure 4-73 Deformed web-gap of continuous fiber B – thick (composite not visible)

The preceding deformed shapes of the web-gaps illustrate that the retrofitting measures significantly reduce the amount of deformation in the web-gap. The positive attachment (connection plate fixed to the top flange, as shown in Figure 4-61) and CFRP overlay retrofit measures show a significant reduction in web-gap deformation as compared to the non-retrofitted detail (Figure 4-60). This is because the positive attachment and CFRP overlay retrofit measures were aimed at stiffening the connection, which would decrease the amount of deformation. The slot repair (Figure 4-62) shows a significant amount of deformation in the web-gap; the slot repair was intended to increase the flexibility of the connection to reduce the stress demand, which increases the amount of deformation in the web-gap. Both the positive attachment and CFRP overlay retrofit measures were considered effective retrofits because the amount of web-gap deformation was reduced from the non-retrofitted web-gap deformation.

4.4 CFRP RETROFIT DISCUSSION

Section 4.3 presents the results from the finite element models of non-retrofitted and retrofitted web-gap details. Stress paths, hot spot stresses (HSS), fringe plots, and deformed web-gap shapes were presented to determine the effectiveness of retrofit measures. The stress paths, HSS, and fringe plots suggest that the positive attachment (connection plate fixed to top flange), slot repair, and all CFRP overlay retrofit measures were effective in reducing the stress demand

in the web-gap. The deformed shapes of the web-gaps demonstrated that the positive attachment and all CFRP overlay retrofit measures reduced the amount of deformation in the web-gap by stiffening the detail; the slot repair was much more flexible, which increased the amount of deformation in the web-gap.

Results from the HSS analysis demonstrated that the CFRP overlay retrofit measures performed better than the established retrofit measures. The configuration of the CFRP overlay did not have a significant impact on the performance. However, the practical application of increasing the thickness of the CFRP overlay relates to bond strength between the composite and steel surfaces; a thicker composite would have a better bond over a thinner composite. It is important that the CFRP overlay is bonded directly to at least both sides of the connection plate and to top flange to properly stiffen the connection.

CHAPTER 5 SUMMARY AND CONCLUSIONS

Transverse stiffener web-gap details are susceptible to fatigue cracks due to secondary stresses caused by differential deflection of adjacent girders. In girders subjected to positive bending moments, the stress demand is the highest near the top girder flange, where the connection plate is not positively connected to the top flange and the top flange is restrained against rotation by the concrete deck. Some retrofit measures have been developed in the past aimed at reducing the magnitude of web-gap stress demand. Common retrofits include a slot repair in which the web-gap length is increased to increase the flexibility of the connection, and a positive connection in which the connection plate is rigidly attached to the top flange to eliminate distortion. These established retrofit measures were studied to understand their effectiveness on reducing the secondary stress in the web-gap region of steel bridge girders. Also, new retrofitting schemes were developed using Carbon Fiber Reinforced Polymers (CFRP) to stiffen the web-gap detail and to provide an alternative load path for secondary stresses. Both the established and new retrofitting schemes were studied using finite element (FE) software.

Results of the FE models showed that both the established (slot and positive attachment) and new (CFRP) retrofits reduced the magnitude of web-gap stress significantly. The positive attachment and CFRP overlay retrofit measures were successful in reducing the amount of deformation in the web-gap as

compared to the non-retrofitted detail. The slot repair had a large amount of deformation because of the increased flexibility as compared to the non-retrofitted detail. Also, based on the results from the finite element models, the CFRP retrofit measures performed better than the established retrofit measures by reducing the maximum principal, S_{11}, S_{22}, and S_{33} stresses. It is also worth noting that the CFRP repair with the resin layer still performed better than the slot and positive attachment retrofits but not as well as the repairs without the resin layer. This was expected because the CFRP overlay was not as stiff when the flexibility of the resin layer is taken into account. The observed reductions in stress demand and web-gap deformation that result from attaching CFRP overlays indicated that this type of retrofit measure may be used successfully to reduce secondary stress demand due to differential deflections of adjacent girders. However, because of practical problems that may arise during fabrication, it is important to validate this retrofit technique with experiments.

REFERENCES

American Concrete Institute (ACI) (2008). *Building Code Requirements for Structural Concrete,* ACI 318-08, American Concrete Institute, Farmington Hills, MI.

American Institute of Steel Construction (AISC) (1986). *Manual of Steel Construction, Load and Resistance Factor Design.* First Ed., Chicago, Ill.

American Association of State Highway and Transportation Officials (AASHTO) (1984). *Standard Specifications for Highway Bridges*, Washington, D.C.

American Association of State Highway and Transportation Officials (AASHTO). (2002). *Standard Specifications for Highway Bridges,* 17th Ed., Washington, D.C.

American Association of State Highway and Transportation Officials (AASHTO). (2004). *Load and Resistance Factor Design Specification (LRFD) Bridge Design Specifications*, 3rd Ed., Washington, D.C.

ASTM D3039 (2000). "Standard Test Method for Tensile Properties of Polymer Matrix Composite Materials," *ASTM International,* West Conshohocken, PA.

Barth (Grider), Amy S. and Bowman, Mark D. (2001). "Fatigue Behavior of Welded Diaphragm-to-Beam Connections." *Journal of Structural Engineering*, v 127, n 10, p 1145-1152.

Barsom, John M. and Rolfe, Stanley T. (2006). *Fracture and Fatigue Control in Structures: Applications of Fracture Mechanics. Third Edition.* Bridgeport, NJ: ASTM.

Bassetti, Andrea; Nussbaumer, Alain; and Hirt Manfred A. (2000). "Crack Repair and Fatigue Life Extension of Riveted Bridge Members Using Composite Materials." *Proceedings of Bridge Engineering Conference: The Egyptian Society of Engineers*, v 1, p 227-238.

Breuer, David (2007). "Laser Peening – Advanced Residual Stress Technology." *Industrial Heating,* v 74, n 1, p 48-50.

Castiglioni, C.A.; Fisher, J.W.; and Yet, B.T. (1988). "Evaluation of Fatigue Cracking at Cross Diaphragms of a Multigirder Steel Bridge." *Journal of Constructional Steel Research*, v 9, n 2, p 95-110.

Cheng, J. J. and Yura, J.A. (1986). "Local web buckling of coped beams." *Journal of Structural Engineering,* ASCE, v 112, n 10, p 2314-2331.

Domazet, Zeljko (1996). "Comparison of Fatigue Crack Retardation Methods." *Engineering Failure Analysis,* v 3, n 2, p 137-147.

Dong, P. and Hong J.K. (2003). "Analysis of Hot Spot Stress and Alternative Structural Stress Methods." *Proceedings of the International Conference on Offshore Mechanics and Arctic Engineering – OMAE,* v 3, p 213-224.

Eaton, Roger A.; Grubb, Michael A.; and Hartmann, Joseph L. (1997). "Example 1: Simple-Span Composite I Girder. Load and Resistance Factor Design (Customary U.S. Units)." *American Iron and Steel Institute, p 1-1 – 1-53.*

Elliot, Arthur L. and LeBeau, Richard J. (1997). "Steel and Concrete Bridges: Load Factor Design." *Structural Engineering Handbook: Fourth Edition.* Ed. Gaylord Jr., Edwin H.; Gaylord, Charles N.; and Stallmeyer, James E. New York: McGraw-Hill, p 18-1 – 18-115.

Fisher, John W. (1984). *Fatigue and Fracture in Steel Bridges: Case Studies.* New York: John Wiley & Sons.

Fisher, John W. and Keating, Peter B. (1989). "Distortion-Induced Fatigue Cracking of Bridge Details with Web Gaps." *Journal of Constructuional Steel Research,* v 12, n 3-4, p 215-228.

Fisher, J.; Jian, J.; Wagner, D; and Yen, B. (1990). "Distortion-Induced Fatigue Cracking in Steel Bridges." *NCHRP Report #336, Transportation Research Board (TRB).*

Goldberg, F. (1973). "Influence of thermal cutting and its quality on the fatigue strength of steel." *Welding Journal*, London, United Kingdom, v 52, n 9, p 392s-404s.

Hacini, Lyes; Van Lê, Ngan; and Bocher, Philippe (2008). "Effect of impact energy on residual stresses induced by hammer peening of 304L plates." *Journal of Materials Processing Technology,* v 208, n 1-3, p 542-548.

Hassan, Ahmed F. and Bowman, Mark D. (1996). "Fatigue Crack Repair of Steel Beams with Tapered Cover Plate Details." *Journal of Structural Engineering*, v 122, n 11, p 1337-1346.

Hu, Yuying; Shield, Carol K.; and Dexter, Robert J. (2005). "Use of Adhesives to Retrofit Out-of-Plane Distortion at Connection Plates." *Transportation Research Board – 6th International Bridge Engineering Conference: Reliability, Security, and Sustainability in Bridge Engineering,* p 419-427.

Kaan, Ben (2008). "Fatigue Enhancements of Category E' Details in Steel Bridge Girders using CFRP Materials" thesis, presented to the University of Kansas at Lawrence, KS, in partial fulfillment of the requirements of the degree of Master of Science in Civil Engineering.

Kaan, B.; Barrett, R.; Bennett, C.; Matamoros, A.; and Rolfe, S. (2008). "Fatigue enhancement of welded coverplates using carbon-fiber composites," *Proceedings of the 2008 ASCE/SEI Structures Congress*, Vancouver, BC, April 24-26, 2008.

Khalil, Ayman; Wipf, Terry J.; Greimann, Lowell; Wood, Douglas L.; and Brakke, Bruce (1998). "Retrofit Solution for Out-of-Plane Distortion of X-Type Diaphragm Bridges." *Transportation Conference Proceedings, Iowa Department of Transportation*, p 99-102.

Kim, M-H and Kang, S-W (2008). "Testing and analysis of fatigue behaviour in edge details: a comparative study using hot spot structural stresses." *Proceedings of the Institution of Mechanical Engineers, Part C: Journal of Mechanical Engineering Science,* v 22, n 12, p 2351-2363.

Leon, A. (1998). "Benefits of Split Mandrel Coldworking." *International Journal of Fatigue,* v 20, n 1, p 1-8.

Lindberg, A.Y. and Schultz, A.E. (2007). *Incorporation of Fatigue Detail Classification of Steel Bridges into the Minnesota Department of Transportation Database: Final Report*. St. Paul: Minnesota Department of Transportation: Research Services Section.

Maddox, S.J. (1998). "Fatigue of steel fillet welds hammer peened under load." *Welding in the World,* v 41, n 4, p 343-349.

Maddox, S.J. (2002). "Hot-Spot Stress Design Curves for Fatigue Assessment of Welded Structures." *International Journal of Offshore and Polar Engineering,* v 12, n 2, p 134-141.

Marquis, Gary and Kahonen, Asko (1996). "Fatigue testing and analysis using the hot spot method." *VTT Publications,* n 239, p 3-35.

National Steel Bridge Alliance (NSBA), accessed 2009. *Steel Bridge Design Handbook. Chapter 8 – Stringer Bridges: Making the Right Choices.* <http://www.aisc.org/contentNSBA.aspx?id=20244>.

Niemi, E. (1993). "Recommendations concerning stress determination for fatigue analysis of welded components." *IIS/IIW 1221-93.* 69 pgs.

Nihei, Kanta; Inamura, Fumihide; and Koe, Shigeki (1997). "Study on Hot Spot Stress for Fatigue Strength Assessment of Fillet Welded Structure." *Proceedings of the International Offshore and Polar Engineering Conference,* v 4, p 557-564.

Okafor, A. Chukwujekwu; Singh, Navdeep; Enemuoh, U.E.; and Rao, S.V. (2005). "Design, analysis and performance of adhesively bonded composite patch repair of cracked aluminum aircraft panels." *Composite Structures,* v 71, n 2, p 258-270.

Ozelton, Malcom W. and Coyle, Timothy G. (1986). "Fatigue Life Improvement by Cold Working Fastener Holes in 7050 Aluminum." *Fatigue in Mechanically Fastened Composite and Metallic Joints, ASTM STP 927.* Ed. John M. Potter. Philadelphia: ASTM, p 53-71.

Poutiainen, Ilkka; Tanskanen, Pasi; and Marquis, Gary (2004). "Finite element methods for structural hot spot stress determination – a comparison of procedures." *International Journal of Fatigue,* v 26, n 11, p 1147-1157.

Roddis, W. M. Kim and Zhao, Yuan (2001). "Out-of-Plane Fatigue Cracking in Welded Steel Bridges. Why It Happened and How It Can Be Repaired." *Welding Innovation*, v 27, n 2, p 2-7.

Roddis, W. M. Kim and Zhao, Yuan (2003). "Finite-Element Analysis of Steel Bridge Distortion-Induced Fatigue." *Journal of Bridge Engineering*, v 8, n 5, p 259-266.

Stallings, J.M.; Cousins, T.E.; and Stafford, T.E. (1996). "Effects of Removing Diaphragms from Steel Girder Bridge." *Transportation Research Record,* n 1541, p 183-188.

Stefanescu, D.; Santisteban, J.R.; Edwards, L.; and Fitzpatrick, M.E. (2004). "Residual Stress Measurement and Fatigue Crack Growth Prediction after Cold Expansion of Cracked Fastener Holes." *Journal of Aerospace Engineering*, v 17, n 3, p 91-97.

Tedesco, J.W.; Stallings, J. M.; and Tow, D.R. (1995). "Finite Element Method Analysis of Bridge Girder-Diaphragm Interaction." *Computers and Structures*, v 56, n 2-3, p 461-473.

Vilhauer, Brian; Bennett, Caroline; Matamoros, Adolfo; Rolfe, Stan (2008). "Fatigue Behavior of Welded Connections Enhanced with UIT and Bolting." *The Kansas Department of Transportation K-TRAN Project No. KU-07-1*.

Wang, Liqun and Helwig, Todd A. (2008). "Stability Bracing Requirements for Steel Bridge Girders with Skewed Supports." *Journal of Bridge Engineering*, v 13, n 2, p 149-157.

Yam, Michael C.H. and Cheng, J.J. Roger (1990). "Fatigue Strength of Coped Steel Beams." *Journal of Structural Engineering*, v 116, n 9, p 2447-2463.

Ye, Xionglin; Zhu, Youli; and Wang, Kan (2006). "Effects of Ultrasonic Impact Treatment on the Residual Stress and Fatigue Performance of Ultrahigh Strength Steel Weld Joint." *IET Conference Publications,* n 524, p 150-154.

Zhao, Yuan and Roddis, W.M. Kim (2007). "Fatigue Behavior and Retrofit Investigation of Distortion-Induced Web Gap Cracking." *Journal of Bridge Engineering,* v 12, n 6, p 737-745.

Zwerneman, Farrel J.; West, Adam B.; and Lim, Kee S. (1993). "Fatigue Damage to Steel Bridge Diaphragms." *Journal of Performance of Constructed Facilities*, v 7, n 4, p 207-224.

APPENDIX A

First One-Plane Structural Stress Calculation

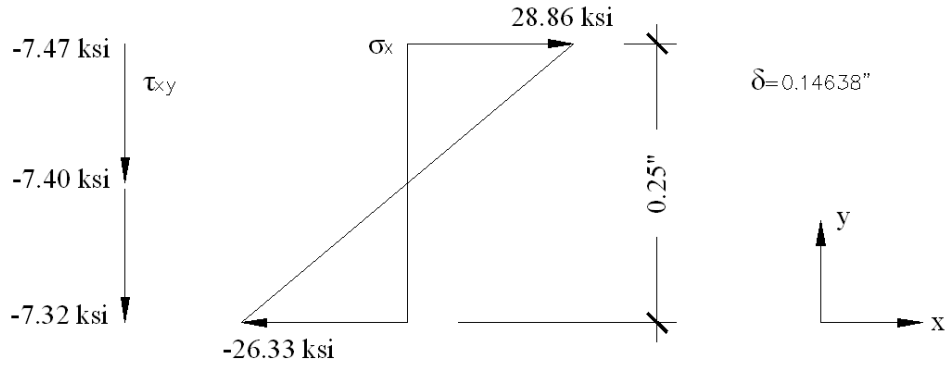

$$\sigma_x(y) = 220.76\,y - 26.33$$

$$\tau_{xy}(y) = -0.6\,y - 7.325$$

$$t = 0.25"$$

$$\sigma_m = \frac{1}{t}\int_0^t \sigma_x(y)$$

$$\sigma_m = 1.265\ ksi$$

$$\sigma_m \frac{t^2}{2} + \sigma_b \frac{t^2}{6} = \int_0^t \sigma_x(y)\ y\ dy + \delta\int_0^t \tau_{xy}(y)\ dy$$

$$\sigma_b = 1.60\ ksi$$

$$\sigma_s = \sigma_m + \sigma_b$$

$$\sigma_s = 2.86\ ksi$$

Second One-Plane Structural Stress Calculation

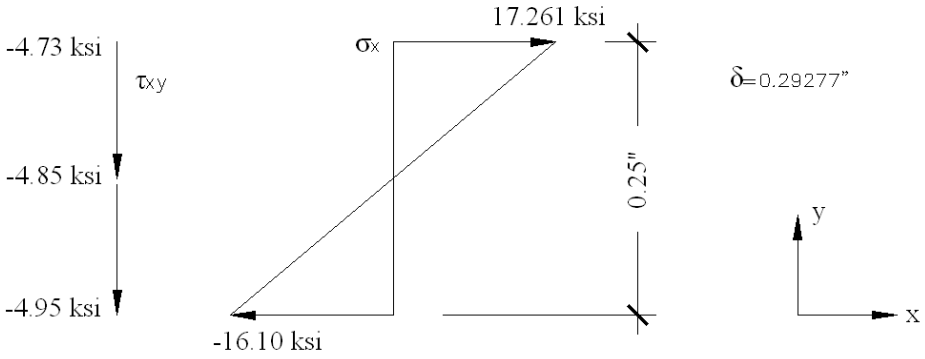

$$\sigma_x(y) = 133.43y - 16.097$$

$$\tau_{xy}(y) = 0.96y - 4.97$$

$$t = 0.25"$$

$$\sigma_m = \frac{1}{t}\int_0^t \sigma_x(y)$$

$$\sigma_m = 0.5818\ ksi$$

$$\sigma_m \frac{t^2}{2} + \sigma_b \frac{t^2}{6} = \int_0^t \sigma_x(y)\ y\ dy + \delta\int_0^t \tau_{xy}(y)\ dy$$

$$\sigma_b = -17.4\ ksi$$

$$\sigma_s = \sigma_m + \sigma_b$$

$$\sigma_s = -16.8\ ksi$$